# CHARACTERIZATION OF THE PROPERTIES OF PHOTOPATTERNED HYDROGELS FOR USE IN REGENERATIVE MEDICINE

by

CALLIE IRENE FIEDLER

B.A., University of San Diego, 2011

M.S., University of Colorado Boulder, 2014

A thesis submitted to the

Faculty of the Graduate School of the

University of Colorado in partial fulfillment

of the requirement for the degree of

Doctor of Philosophy

Department of Electrical, Computer, and Energy Engineering

This thesis entitled:

Characterization of the properties of photopatterned hydrogels for use in regenerative medicine

written by Callie Irene Fiedler

has been approved for the Department of

Electrical, Computer, and Energy Engineering

_____

Robert R. McLeod, Ph.D.

_____

Stephanie J. Bryant, Ph.D.

Date_____

The final copy of this thesis has been examined by the signatories, and we find that both the content and the form meet acceptable presentation standards of scholarly work in the above mentioned discipline.

ABSTRACT

Fiedler, Callie Irene (Ph.D., Electrical, Computer, and Energy Engineering)

**Characterization of the properties of photopatterned hydrogels for use in regenerative medicine**

Thesis directed by Professor Robert R. McLeod

The goal of this thesis was to locally photopattern cytocompatible hydrogels to exhibit a wide range of mechanical properties and to probe the fundamental parameters governing these materials printed via stereolithography (SLA). Fabricating cell-laden structures with locally defined mechanical properties is non-trivial because the use of multiple precursor materials is wasteful, slow, and can lead to cell-death. To investigate the range of mechanical properties a single precursor solution can produce, a single-network hydrogel was initially formed and cyclically in- swelled fresh precursor solution followed by photo-exposure of the swollen gel ("swelling + exposure" or SE cycle). Because transport (i.e., diffusion and swelling) can occur on the same time scale as photopolymerization reaction kinetics, the variable modulus hydrogels were first characterized in bulk to isolate the reaction kinetics. These experiments demonstrated the ability modify the mechanical and chemical (i.e., compressive modulus, toughness, crosslink density, swelling ratio) properties by up to 10-fold using only 2-4 SE cycles.

The understanding gained via these bulk experiments was then used to locally photopattern the elastic modulus of a cytocompatible hydrogel with pixel-limited resolution (~10s μm) employing a custom SLA system. The ability to fabricate hydrogels with a 500% elastic moduli increase with respect to the unpatterned hydrogel was then verified using using atomic force microscopy. Monomer attachment to the existing matrix was monitored as a function of SE cycle using confocal fluorescence microscopy to characterize the shape and size

of printed features. The dependence of these features on material and processing conditions was then demonstrated to be explained by a first-order reaction/diffusion model. SLA 3D printed, soft, cytocompatible hydrogels (~10s kPa) with ~250 μm channels were then fabricated in addition to fabricating 3D printed stiff, cytocompatible hydrogels (39 MPa) both with ~10 μm resolution. With this fundamental understanding and demonstration of 3D printed soft, low solids-content hydrogels, printed complex and cytocompatible 3D tissue engineering constructs are possible.

# Acknowledgements

I would like to acknowledge and thank all who assisted me in this work. This list includes, but is in no way limited to the following people: my advisor, Professor Robert McLeod for his constant enthusiasm, support, guidance, and endless flow of ideas; my committee, Professors Stephanie Bryant, Virginia Ferguson, Juliet Gopinath, and Sean Shaheen, for their continued support and guidance throughout this process; the members of the McLeod Lab, who have been a constant source of encouragement and entertainment; the members of the Bryant Lab for welcoming me and giving me a second home at east campus (both figuratively and literally); the members of the Ferguson Lab for their support and enthusiasm for our collaborative project; the ECEE Facilities Manager, Wayne Gardner, for being my go-to person to fix anything that is broken in our lab; my fiancé, for his ability to support me through every failure and champion me during my successes; my family for their unwavering support from afar; the Higgins family, for supporting me at every stage in this process and encouraging me when I needed it most; and my incredible friend group.

# Dedication

*I dedicate this dissertation to my incredible parents, Cassie and Bill Gilmore, my fiancé, my family, and my friends for affording me the opportunity to succeed through their unrelenting support and for always believing I could change the world, if by many small or large actions.*

# Table of Contents

# List of Figures

# List of Tables

# Chapter 1- Introduction

## 1.1 Regenerative medicine

The use of human-derived stem cells to treat diseases and injuries ranging from arthritis to paralysis has the potential to revolutionize the medical field. Personalized medical treatments are advantageous because they allow drugs to be pre-screened by the patient's system prior to treatment. Specifically, personalized regenerative medicine focuses on understanding how biological tissues are formed and maintained *in vivo*, to restore damaged or diseased tissues.[1,2] One method to understand tissue behavior is to duplicate the physical environment during tissue growth, which provides a framework for patient-specific tissue engineering.[3] Current research in this field concentrates on engineering and recapitulating the mechanical and chemical environments that allow cells to develop into useful tissue.

One such tissue of interest is the bone-cartilage or osteochondral interface. This interface covers the ends of bones within the joint and connects the load-bearing bone to the elastic articular cartilage that reduces joint friction.[4] Cartilage does not have any vasculature and therefore cannot fully heal when injured due to insufficient nutrients and regenerative stem-cells. Current research explores filling the wound defect with bone-derived, mesenchymal stem cell (MSC) laden soft (~10s-100s kPa) hydrogel, but the physical loads sustained by joints are too high for the encapsulated cells to differentiate into the ideal, articular cartilage and can reduce cell viability due to hydrogel failure.[5–8] Stiff hydrogels that can sustain the physiological loads similar to native cartilage have also been tested, but the increased crosslinking density is too high for MSCs to receive sufficient nutrients, which also leads to cell death.[9–11] A variety of techniques attempt to recapitulate this region using both soft, MSC-laden material (10s kPa) and stiff supporting material (~1MPa) including electro-spun collagen fibers and collagen-based microsphere scaffolds onto which cells are seeded.[12,13] While these techniques are promising, their inability to locally control the mechanical and chemical properties within a structure limits their utility.

3D printing is a promising technique to locally control material deposition of multiple materials. Fabricating structures with user-defined mechanical and chemical properties will enable patient-specific tissue engineering, which motivates the body of research devoted to

biomaterial printing. Next a range of 3D printing techniques are reviewed, focusing on the stereolithography system, which is used throughout this work.

## 1.2 Three-Dimensional Printing

3D printing is a promising technology for regenerative medicine because it allows customized structures to be fabricated ranging from acellular bone-tissue scaffolding to cell-laden vascularized hydrogels.[14–17] To fabricate structures, this technique uses a computer aided design (CAD) of the desired structure to digitally 'slice' it into two dimensional (2D) cross-sections of defined thickness, which are then delivered to the printer to iteratively build a 3D structure. A defining feature of 3D printing is the ability to fabricate structures with overhanging features, meaning structures like porous bone can be physically duplicated. A variety of printing techniques are currently in use for tissue engineering, the three most prominent being selective laser sintering (SLS), polymer extrusion or fusion deposition modeling (FDM), and stereolithography (SLA).[18]

### *1.2.1 Selective Laser Sintering (SLS)*

Selective Laser Sintering (SLS) solidifies a powder via heat from a scanning focused laser. A new layer is printed when the powder bed platform moves down and a recoater arm moves fresh material from a powder supply reservoir into the vacant printing region, as shown in **Figure 1.1**. SLS is a useful technique to print structures of stiff (~GPa) material that cannot be readily fabricated using traditional techniques (*e.g.,* injection molding is unable to fabricate a porous, metal scaffold for bone regeneration).[19] Overhanging features are naturally supported by the unexposed powder bed. Conversely, because this technique uses a powder material, surface-roughness is dependent on the powder particle size, which leads to part failure in high-friction environments (e.g., joint structures).[12,20,21] Additionally, many biomaterials cannot be sintered from powder form.

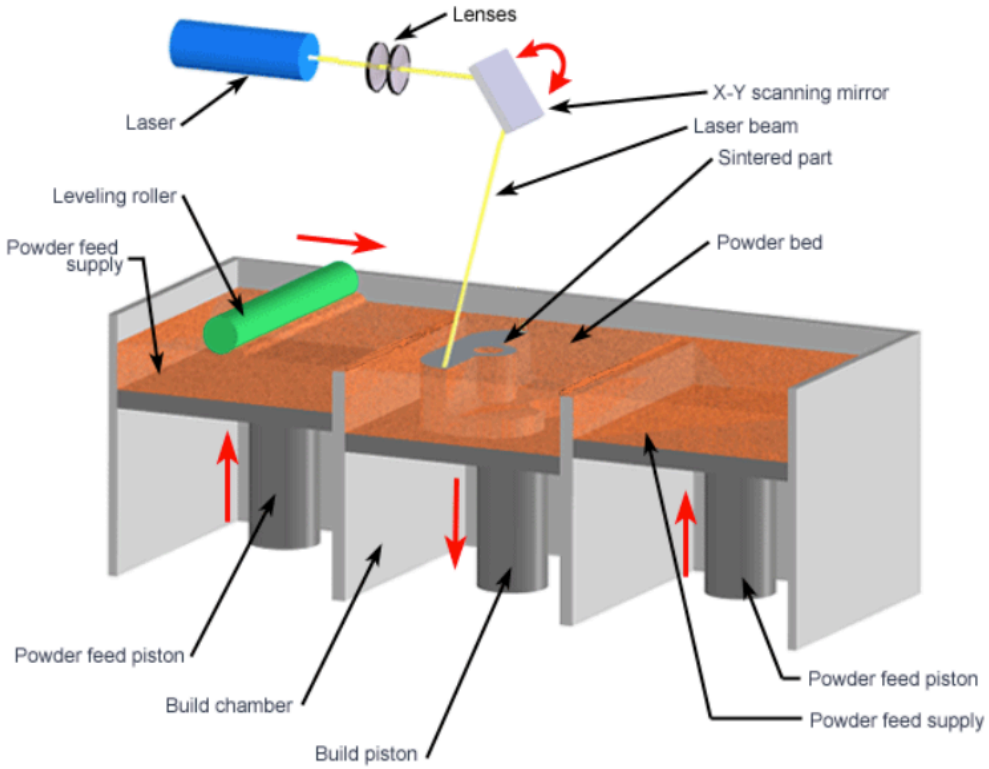


**Figure 1.1** Schematic of SLS where a cross-section of the desired 3D structure is sintered in the powder bed, the build chamber then moves down, the recoater arm or levelling roller pushes a new supply of powder into the chamber for the next cross-section to be sintered. (adapted from Verma et al.[20]).

*1.2.2 Fused Deposition Modeling (FDM)*

FDM is currently the most widely used 3D printing technique in regenerative medicine, so much so that the community uses the term 'inkjet' or 'bioprinting' exclusively for this printing process. FDM uses either a series of nozzles or filaments to deposit material onto a substrate from above where, again, a 2D section of the 3D structure is built up by scanning the print head (**Figure 1.2**). FDM, also referred to as polymer extrusion, is an appealing technique to fabricate synthetic biological tissues due to its ability to print multiple cytocompatible soft materials in a single structure.[3,22,23] However, to date there have been no structures fabricated with both stiff (~1-100s MPa) and soft regions (~10s-100s kPa) in a single print.[24] The barrier, which is a focus of this work, is that stiff, cytotoxic material diffuses into the soft, hydrated material.

Materials in FDM must be shear-thinning to be extruded[23]. Shear-thinning, thixotropic materials behave as a liquid when a force is applied (i.e., as the material is extruded) and then behave as a solid when the shearing force is removed.[25] This requirement constrains the range of useful materials to a subset of liquid polymers and is currently the subject of substantial academic and industrial research.[17,26,27] The pressure to deposit material can also reduce cell viability, therefore the printing speed is constrained by the amount of pressure a given cell line can sustain.[28] The extrusion nozzle is an additional constraint because it limits the minimum feature size and resolution of the printed structure to approximately two-times the tip diameter (>10μm).[29]

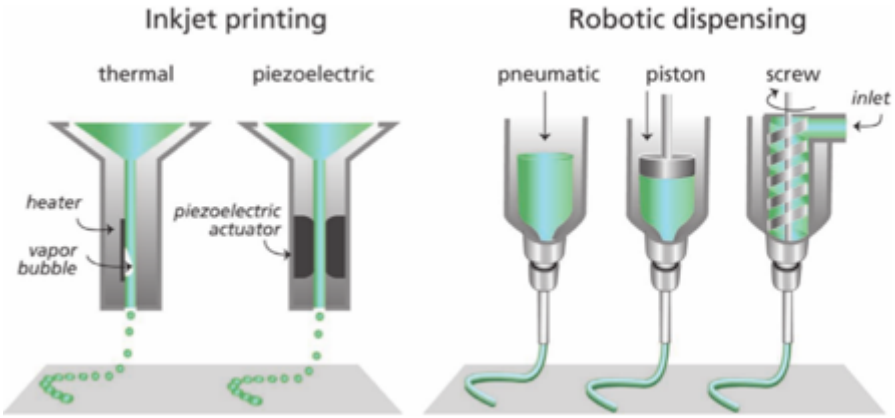


**Figure 1.2** Schematic of two types of FDM processes, where inkjet utilizes thermal or piezoelectric control of material deposition and robotic dispensing requires an external force to deposit material through a nozzle-based system (adapted from Malda et al., 2013[30]).

*1.2.3 Stereolithography (SLA)*

SLA was the first demonstration of 3D printing, invented by Chuck Hull in 1983. This method uses a photo-curable liquid resin and an exposure source (laser or programmable mask) to solidify 2D cross-sections of a desired structure. Translating the sample stage axially allows fresh material to flow into the vacated patterning region, where a new layer is exposed. There are currently two techniques to fabricate structures using this technology: laser-scanning SLA and projection SLA (**Figure 1.3** left and right, respectively).

Two-photon laser-scanning SLA employs a laser that scans across the surface of the photo-reactive material to produce a cross-section of the desired 3D structure (**Figure 1.3**). This technique can produce high-resolution (~100s nm), small minimum feature size (~100s nm) structures by using multi-photon polymerization, where the resin polymerization is constrained to the laser focus by two-photon absorption[31–34]. This technique is advantageous because it does not require a recoater arm to move new material into the patterning region due to localized polymerization within the resin volume.

While laser scanning systems can accommodate fabrications that require high spatial resolution, because the laser must be scanned across the surface of or within the volume photo-reactive material to produce a 3D structure printing speed substantially reduced (~10-100X) with respect to SLS, FDM, or projection SLA.[35] As with laser-scanning SLA, projection SLA employs a photo-reactive liquid material to polymerize a 3D structure. However, instead of scanning a laser across the surface to produce a cross-section of the 3D structure, projection-based systems photopattern an entire 2D section in a single step. Not only does this projection photopatterning technique reduce printing time by orders of magnitude from laser scanning techniques, it also eliminates the additional calibration step required to correlate scanning speed to feature width. This is because the radical initiation rate, which is the first step of the polymerization process, classically goes as the square-root of incident intensity and therefore the speed of printing increases by dividing light into many parallel channels at the same total power, e.g., a projector.[36]

Most projection-based SLA systems utilize a non-stick window against which the 2D projected image slice is polymerized.[37] The most commonly used non-stick window for this technique is polydimethylsiloxane (PDMS), which serves as an oxygen reservoir that inhibits the homo-polymerization process of vinyl species, the most common reactive species in SLA resins.[38,39] However, this window does not work for all resins because some photo-chemistries are not inhibited by oxygen (*e.g.*, thiol-ene click chemistry).[40,41] For this reason, alternate SLA windows are the topic of current research.[42] Other silane-based materials (*e.g.,* RainX) have been demonstrated as a nonstick window coatings for oxygen-inert resins, but because structures printed with greater than two layers are not reported, more research is required to validate this non-stick window use.[43] Additionally, some research demonstrates this technique without a window, but layer-thickness control is limited to limits $100 \pm 20\mu m$.[44]

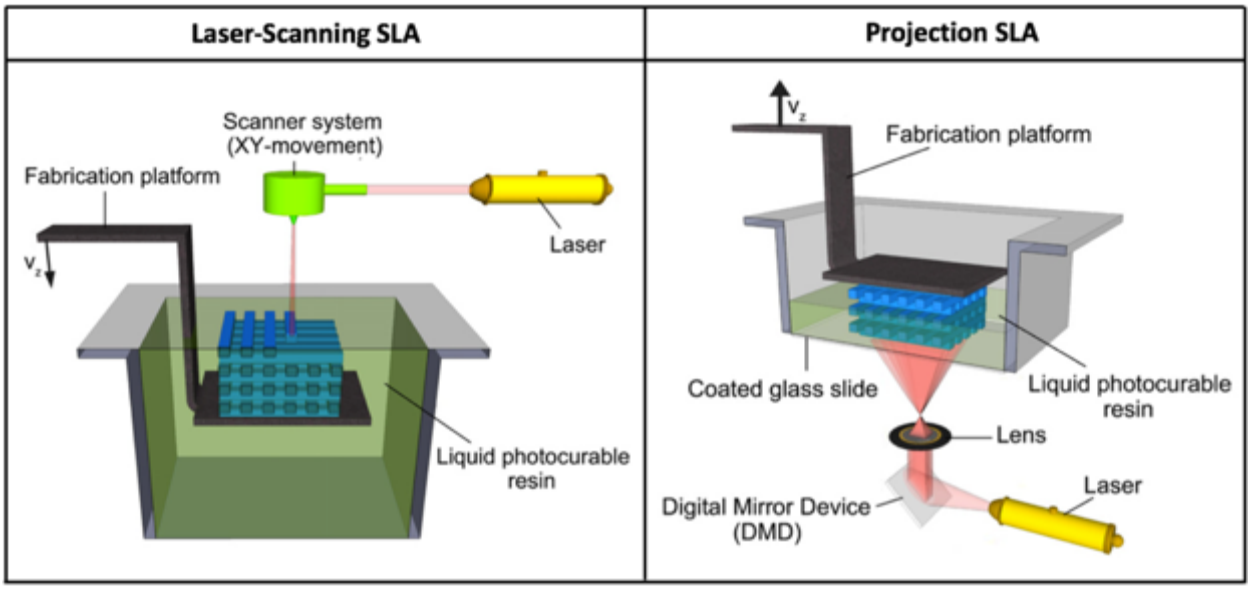


**Figure 1.3** Illustration of SLA laser-scanning and projection systems, where the material is fabricated upon a platform and iteratively built by selectively polymerizing regions exposed to the desired photopattern (adapted from Billiet et al., 2012[31]).

Commercial laser-scanning and projection SLA systems shown in Figure 1.3 use a large volume of resin that can be prohibitive for expensive materials. Fortunately, this is not a design requirement and can be modified to confine the material between the window and sample substrate via capillary forces, which requires very little material to fabricate a structure (~100s to 1000s μL, part-size dependent).[45] This modification allows expensive and environment-sensitive (*e.g.,* temperature, humidity, etc.) materials to be printed (*e.g.*, cell-laden materials).

Unlike FDM, printing structures with multiple materials using SLA is difficult because all unreacted material must be removed from the part to print a second material. When printing hydrogels with high water concentrations (50-95%), this become particularly difficult because the second resin will readily diffuse into the first hydrogel structure, reducing the fidelity of the printed part. Like FDM, SLA is thus similarly unable to print both stiff and soft, cell-laden materials because diffusion of stiff precursor solution into the hydrogel network will lead to cell-death.[46] Overcoming this limitation in SLA is the subject of Chapter 2.

As is derived in chapter M, printing resolution in SLA is limited by the diffusion rate of radical initiating species that is particularly high in low viscosity hydrogel precursors consisting primarily of water. This has been addressed by adding an inert compound to the formulation that

increases the viscosity, enabling ~1 mm feature size as shown in **Figure 1.4**. Unfortunately, there has been limited work to demonstrate true 3D structures with overhangs and internal channels with size less than ~2 mm. [48] Chapter X demonstrates 3D printing of complex hydrogel structure including internal 250 micron channels via the use of a very high reactivity thiol-ene polymer that reduces the transport-limited resolution to as little as Y microns.

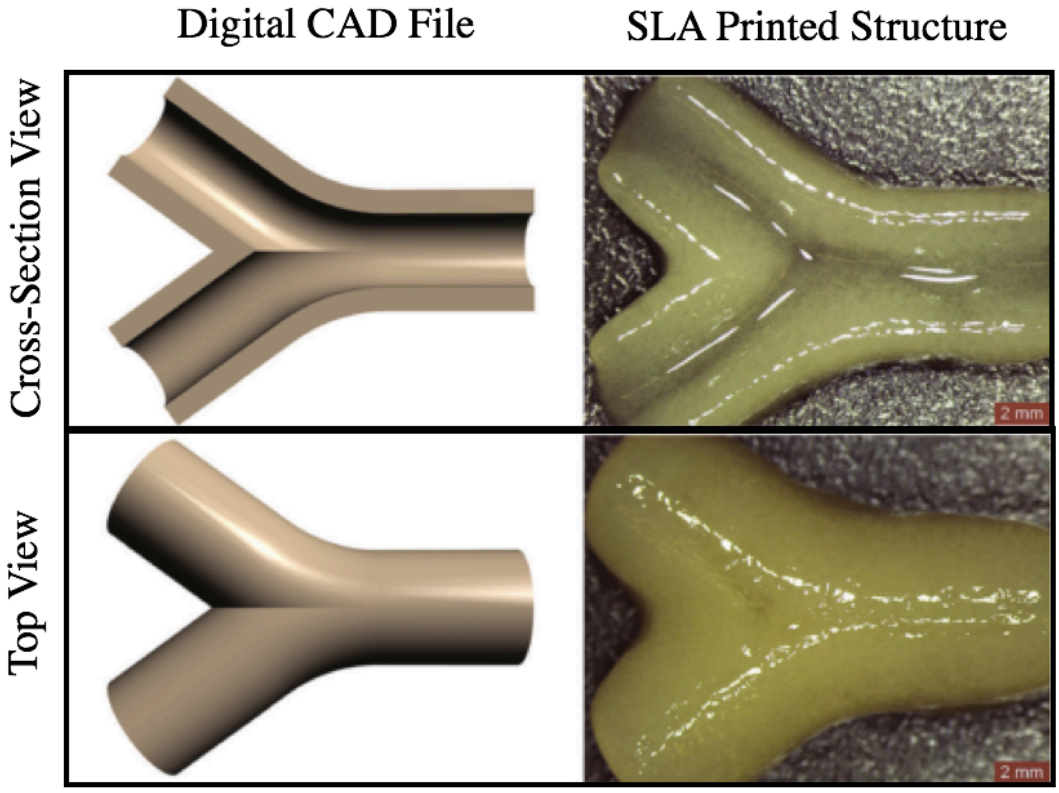


**Figure 1.4** Work demonstrating SLA 3D printed hydrogel constructs with a channel, where the minimum feature size is ~1 mm, adapted from Elomaa *et al.*[48]

### 1.3 Thesis Approach

This work demonstrates a projection SLA system able to print high-fidelity hydrogel structures with a wide range of mechanical properties using a single material.[44,47–51] Chapter 2 presents the fundamental concepts and design tradeoffs of SLA including the relevant reaction/diffusion kinetics. Chapter 3 introduces the multiple patterning concept and uses bulk materials testing to demonstrate order of magnitude increase in mechanical properties using a single precursor solution. In chapter 4, the multiple patterning method is applied to SLA to create variable modulus hydrogel structures. Limits to the fidelity of this photopatterning method are

characterized in Chapter 5 and compared to a first order reaction/diffusion model. Finally, Chapter 6 presents novel 3D printed hydrogel structures including interior 250 micron diameter channels in a low (15 wt%) solids content hydrogel with no thickening agents as well as printed stiff biomaterials.

### 1.4 References


1. Bajaj, P., Schweller, R. M., Khademhosseini, A., West, J. L. & Bashir, R. 3D Biofabrication Strategies for Tissue Engineering and Regenerative Medicine. *Annu. Rev. Biomed. Eng.* **16,** 247–76 (2014).
2. Huh, D., Hamilton, G. a. & Ingber, D. E. From 3D cell culture to organs-on-chips. *Trends Cell Biol.* **21,** 745–754 (2011).
3. Jang, J., Yi, H.-G., Cho ACS Biomater Sci Eng, D.-W. & Cho, D.-W. 3D Printed Tissue Models: Present and Future. (2016). doi:10.1021/acsbiomaterials.6b00129
4. Mansour, J. M. *Biomechanics of Cartilage in: Kinesiol. Mech. pathomechanics Hum. Mov.* (Lippincott Williams & Wilkins, 2003). at <http://web.mit.edu/cortiz/www/3.052/3.052CourseReader/27_BiomechanicsofCartilage.pdf>
5. Allan, K. S., Pilliar, R. M., Wang, J., Grynpas, M. D. & Kandel, R. A. Formation of biphasic constructs containing cartilage with a calcified zone interface. *Tissue Eng.* **13,** 167–77 (2007).
6. Burdick, J. A. & Anseth, K. S. Photoencapsulation of osteoblasts in injectable RGD-modified PEG hydrogels for bone tissue engineering. *Biomaterials* **23,** 4315–4323 (2002).
7. Steinmetz, N. J., Aisenbrey, E. A., Westbrook, K. K., Qi, H. J. & Bryant, S. J. Mechanical loading regulates human MSC differentiation in a multi-layer hydrogel for osteochondral tissue engineering. *Acta Biomater.* **21,** 142–153 (2015).
8. Aisenbrey, E. A. & Bryant, S. J. Mechanical loading inhibits hypertrophy in chondrogenically differentiating hMSCs within a biomimetic hydrogel. *J. Mater. Chem. B* **4,** 3562–3574 (2016).
9. Bryant, S. J., Nuttelman, C. R. & Anseth, K. S. The effects of crosslinking density on cartilage formation in photocrosslinkable hydrogels. *Biomed. Sci. Instrum.* **35,** 309–14 (1999).

10. Weber, L. M., Lopez, C. G. & Anseth, K. S. Effects of PEG hydrogel crosslinking density on protein diffusion and encapsulated islet survival and function. *J. Biomed. Mater. Res. Part A* **90A,** 720–729 (2009).
11. Reinhart, C. T. & Peppas, N. A. Solute diffusion in swollen membranes. Part II. Influence of crosslinking on diffusive properties. *J. Memb. Sci.* **18,** 227–239 (1984).
12. Mikos, A. G. *et al.* Engineering complex tissues. *Tissue Eng.* **12,** 3307–3339 (2006).
13. Walters, B. D. & Stegemann, J. P. Strategies for directing the structure and function of three-dimensional collagen biomaterials across length scales. *Acta Biomater.* **10,** 1488–1501 (2014).
14. Chim, H. *et al.* A comparative analysis of scaffold material modifications for load-bearing applications in bone tissue engineering. *Int. J. Oral Maxillofac. Surg.* **35,** 928–934 (2006).
15. Zhou, X. *et al.* 3D bioprinted graphene oxide-incorporated matrix for promoting chondrogenic differentiation of human bone marrow mesenchymal stem cells. *Carbon N. Y.* (2017). doi:10.1016/j.carbon.2017.02.049
16. Kolesky, D. B. *et al.* 3D Bioprinting of Vascularized, Heterogeneous Cell-Laden Tissue Constructs. *Adv. Mater.* **26,** 3124–3130 (2014).
17. Norotte, C., Marga, F. S., Niklason, L. E. & Forgacs, G. Scaffold-free vascular tissue engineering using bioprinting. *Biomaterials* **30,** 5910–5917 (2009).
18. Pellegrino, J., Makila, T., Mcqueen, S. & Taylor, E. Measurement Science Roadmap for Polymer-Based Additive Manufacturing Measurement Science Roadmap for Polymer-Based Additive Manufacturing Measurement Science Roadmap for Polymer-Based Additive Manufacturing i. *NIST Adv. Manuf. Ser.* **100,** (2016).
19. Tele Nko, C. & Seepersad, C. C. A Comparative Evaluation of Energy Consumption of Selective Laser Sintering and Injection Molding of Nylon Parts. at <https://sffsymposium.engr.utexas.edu/Manuscripts/2011/2011-04-Telenko.pdf>
20. Verma, A. & Rai, R. Energy Efficient Modeling and Optimization of Additive Manufacturing Processes. at <https://www.researchgate.net/profile/Anoop_Verma5/publication/251231305_Energy_Efficient_Modeling_and_Optimization_of_Additive_Manufacturing_Processes/links/02e7e51eeec020ef49000000.pdf>
21. Bergmann, G. *et al.* Hip contact forces and gait patterns from routine activities. *J.*

*Biomech.* **34,** 859–871 (2001).

22. Park, J. Y., Gao, G., Jang, J. & Cho, D.-W. 3D Printed Structures for Delivery of Biomolecules and Cells: Tissue Repair and Regeneration. *J. Mater. Chem. B* (2016). doi:10.1039/C6TB01662F
23. Hospodiuk, M., Dey, M., Sosnoski, D. & Ozbolat, I. T. The bioink: A comprehensive review on bioprintable materials. *Biotechnol. Adv.* (2017). doi:10.1016/j.biotechadv.2016.12.006
24. Gu, B. K. *et al.* 3-dimensional bioprinting for tissue engineering applications. *Biomater. Res.* **20,** 12 (2016).
25. Mezger, T. G. The rheology handbook : for users of rotational and oscillatory rheometers. (2006). at <http://www.bcin.ca/Interface/openbcin.cgi?submit=submit&Chinkey=240303>
26. Hospodiuk, M., Dey, M., Sosnoski, D. & Ozbolat, I. T. The bioink: A comprehensive review on bioprintable materials. *Biotechnol. Adv.* **35,** 217–239 (2017).
27. Suntornnond, R., An, J. & Chua, C. K. Roles of support materials in 3D bioprinting. *Int. J. Bioprinting* **3,** (2017).
28. Wang, X., Jiang, M., Zhou, Z., Gou, J. & Hui, D. 3D printing of polymer matrix composites: A review and prospective. *Compos. Part B Eng.* (2016). doi:10.1016/j.compositesb.2016.11.034
29. Cui, H., Nowicki, M., Fisher, J. P. & Zhang, L. G. 3D Bioprinting for Organ Regeneration. *Adv. Healthc. Mater.* 1601118 (2016). doi:10.1002/adhm.201601118
30. Malda, J. *et al.* 25th Anniversary Article: Engineering Hydrogels for Biofabrication. *Adv. Mater.* **25,** 5011–5028 (2013).
31. Billiet, T., Vandenhaute, M., Schelfhout, J., Van Vlierberghe, S. & Dubruel, P. A review of trends and limitations in hydrogel-rapid prototyping for tissue engineering. *Biomaterials* **33,** 6020–6041 (2012).
32. Serbin, J. *et al.* Femtosecond laser-induced two-photon polymerization of inorganic-organic hybrid materials for applications in photonics. *Opt. Lett.* **28,** 301–303 (2003).
33. Tormen, M. *et al.* 3D patterning by means of nanoimprinting, X-ray and two-photon lithography. *Microelectron. Eng.* **73–74,** 535–541 (2004).
34. Park, S.-H., Yang, D.-Y. & Lee, K.-S. Two-photon stereolithography for realizing

ultraprecise three-dimensional nano/microdevices. *Laser Photonics Rev.* **3,** 1–11 (2009).

35. Zhou, G. *et al.* Digital light procession three-dimensional printing acrylate/collagen composite airway stent for tracheomalacia. *J. Bioact. Compat. Polym.* 88391151668609 (2017). doi:10.1177/0883911516686090
36. Odian, G. *Principles of Polymerization*. (A JOHN WILEY & SONS, INC., 2004).
37. Zheng, X. *et al.* Design and optimization of a light-emitting diode projection micro-stereolithography three-dimensional manufacturing system. *Rev. Sci. Instrum.* **83,** (2012).
38. Tumbleston, J. R. *et al.* Continuous liquid interface production of 3D objects. *Science (80-. ).* **347,** (2015).
39. Janusziewicz, R., Tumbleston, J. R., Quintanilla, A. L., Mecham, S. J. & DeSimone, J. M. Layerless fabrication with continuous liquid interface production. *Proc. Natl. Acad. Sci. U. S. A.* 201605271 (2016). doi:10.1073/pnas.1605271113
40. Ashley, J. F., Cramer, N. B., Davis, R. H. & Bowman, C. N. Soft-lithography fabrication of microfluidic features using thiol-ene formulations. *Lab Chip* **11,** 2772–2778 (2011).
41. Lowe, A. B. Thiol-ene 'click' reactions and recent applications in polymer and materials synthesis. *Polym. Chem.* **1,** 17–36 (2010).
42. Guo, N. & Leu, M. C. Additive manufacturing: Technology, applications and research needs. *Front. Mech. Eng.* **8,** 215–243 (2013).
43. Linnenberger, A. Live cell lithography and non-invasive mapping of neural networks. (University of Colorado Boulder, 2014).
44. Chan, V., Zorlutuna, P., Jeong, J. H., Kong, H. & Bashir, R. Three-dimensional photopatterning of hydrogels using stereolithography for long-term cell encapsulation. *Lab Chip* **10,** 2062–2070 (2010).
45. Linnenberger, A. *et al.* Three dimensional live cell lithography. *Optics express* **21,** 10269–77 (2013).
46. Chen, C. S., Mrksich, M., Huang, S., Whitesides, G. M. & Ingber, D. E. Geometric control of cell life and death. *Science* **276,** 1425–1428 (1997).
47. Sun, A. X., Lin, H., Beck, A. M., Kilroy, E. J. & Tuan, R. S. Projection Stereolithographic Fabrication of Human Adipose Stem Cell-Incorporated Biodegradable Scaffolds for Cartilage Tissue Engineering. *Front. Bioeng. Biotechnol.* **3,** 115 (2015).
48. Elomaa, L. *et al.* Three-dimensional fabrication of cell-laden biodegradable poly(ethylene

glycol-co-depsipeptide) hydrogels by visible light stereolithography. *J. Mater. Chem. B* **3,** 8348–8358 (2015).

49. Polizzotti, B. D., Fairbanks, B. D. & Anseth, K. S. Three-Dimensional Biochemical Patterning of Click-Based Composite Hydrogels via Thiolene Photopolymerization. *Biomacromolecules* **9,** 1084–1087 (2008).
50. Gandavarapu, N. R., Alge, D. L. & Anseth, K. S. Osteogenic differentiation of human mesenchymal stem cells on α5 integrin binding peptide hydrogels is dependent on substrate elasticity. *Biomater. Sci.* **2,** 352–361 (2014).
51. Weng, Z., Zhou, Y., Lin, W., Senthil, T. & Wu, L. Structure-Property Relationship of Nano Enhanced Stereolithography Resin for Desktop SLA 3D Printer. *Compos. Part A Appl. Sci. Manuf.* (2016). doi:10.1016/j.compositesa.2016.05.035

# Chapter 2 - Three-dimensional (3D) Stereolithography Additive Manufacturing (SLA-AM)

## 2.1 Executive Summary

This chapter presents the design and characterization of a custom three-dimensional projection stereolithography (SLA) system to print small volumes of cytocompatible, low-viscosity (1cps) precursor solutions. Photopolymerization, diffusion, and Beer-Lambert Absorption are discussed because they are the fundamental properties of SLA 3D printing and constrain system design specifications, which are further constrained by requiring the system to print cytocompatible materials. A commercial photopattern generator consisting of a DMD spatial light modulator, three switchable LED sources, and objective optics is characterized for uniformity and the gray-scale capability of the DMD is used to create a uniform illumination region over the center 30% of the field. The optical capabilities of the SLA-AM system are characterized using a commercial photoresist, demonstrating pixel-limited photopattern resolution (~10 μm) with a maximum illumination intensity of 20 mW/cm$^2$.

## 2.2 Stereolithography (SLA) Fundamentals

SLA 3D printing remains a prominent tool to fabricate complex structures for rapid prototyping and manufacturing, decades past its invention in 1983. However, extension to cytocompatible hydrogel biomaterials for regenerative medicine requires a greater understanding of how transport phenomenon such as diffusion and swelling limit fabrication fidelity.[1] For example Chuck Hull introduced the use of a strong photo-absorber to control the penetration depth of the laser and thus the layer thickness.[2] Less well documented is that the transverse feature size depends both on the optical spot size and the reaction and diffusion kinetics of the exposed resin. A significant portion of this thesis is dedicated to understanding and harnessing these kinetics, specifically in low solids content, high diffusivity resins. Similarly, hydrogels introduce post-gelation swelling that can significantly distort printed structures during or after printing.

This chapter introduces the fundamental principles and components of SLA systems including photopolymerization, diffusion, and Beer-Lambert absorption. The trade-offs between different system design components are considered, including resolution and minimum feature size, illumination and wavelength, depth of focus, and choice of programmable mask. With these principles, a custom SLA system is designed and characterized.

### *2.2.1 Photopolymerization and Diffusion*

The transport and reaction kinetics during photopolymerization affect photopattern fidelity, total printing time, and the ability to photopattern mechanical property variations. Polymerization is the mechanism by which small molecules, monomers, are linked together to form larger molecules, oligomers, that eventually become a solid polymer. The most common initiation mechanism for SLA is free-radical polymerization. The reaction proceeds by first **initiation**, in which radicals are generated by photolysis of a photoinitiator, then **propagation**, in which these monomer radicals react with additional monomers to create propagating polymer radicals and finally **termination**, in which propagating polymer radicals terminate.

The process of **initiation** begins when an initiator ($I$), absorbs a photon ($hv = E_{photon}$, where $h$ is Plank's constant and $v$ is the radiation frequency) and cleaves to form reactive species ($R\bullet$) that can then diffuse and react with monomer ($M$) to produce a reactive monomer species, as described by the following equations,

$$I + hv \rightarrow 2R\bullet$$

$$R\bullet + M \rightarrow (R-M)\bullet \rightarrow (\mathrm{M_n}\bullet) \ . \tag{2-1}$$

These combined processes govern the rate of primary and propagating radical generation[3].

Unreacted monomers species ($M$) can readily diffuse and react with the propagating polymer radicals ($\mathrm{M_n}\bullet$) to produce a new, larger radical species ($\mathrm{M_{n+1}}\bullet$),

$$(M_n\bullet) + M \xrightarrow{k_p} (M_{n+1}\bullet), \tag{2-2}$$

which is generally called **propagation**. As this process continues, the oligomers produced continue to grow in molecular weight, increasing the material viscosity. In the multifunctional monomers that will be used here, sufficient crosslinks eventually form such that the network spans the printed volume and the molecular weight becomes effectively infinite. At this phase

transition, the high viscosity oligomers become a low modulus solid swollen with the remaining monomer, unattached oligomers and water; in other words, a gel. Controlling this gelation is the central goal of SLA. Further conversion of stiff monomers at high solids content can lead to a second phase transition from a rubbery solid to a vitrified glass reducing chemical transport and suppressing continued reactions.[3,4]

Finally, **termination** is the mechanism that consumes radicals, reducing radical concentrations, and can occur via three different avenues: recombination, disproportionation, and/or occlusion, as depicted below,

$$\begin{aligned}(M_m\bullet) + (M_n\bullet) &\rightarrow M_{m+n} && \textit{(recombination)}\\ &\rightarrow M_m + M_n && \textit{(disproportionation)}\\ &\rightarrow \{M_m\}\bullet + \{M_n\}\bullet && \textit{(occlusion)}\end{aligned} \tag{2-3}$$

*Recombination* occurs when two radical oligomers and/or polymers combine to a single molecule and the radicals terminate one another. *Disproportionation* occurs when one radical oligomer abstracts the radical from a second oligomer, terminating both oligomers without forming a covalent bond between them. Finally in some cases, the radical species are unable to interact with another species because they are physically confined, as indicated by the curly brackets, and result in trapped radical species, which is called *occlusion*.[3]

Rate equations such as these are sufficient when the intensity is spatially uniform. In patterned exposure of a liquid or gel material, however, concentration and chemical potential gradients lead to diffusion of liquid components. [5,6] This in turn causes swelling of the solid network. Diffusion-driven concentration change as a function of time can be understood using Fick's second law, written in one dimension as,

$$\frac{\partial c}{\partial t} = \frac{\partial}{\partial x}\left(D\frac{\partial c}{\partial x}\right), \tag{2-4}$$

where $D$ is the diffusion coefficient.[7] $D$ may vary in space, $x$, and time, $t$, particularly due to local monomer, $c$, conversion. However, in the case of low solids content hydrogels (~5-20 wt%), $D$ is approximately a constant because the distance between crosslinks in the polymer, or mesh size, is much greater than the hydrodynamic radius of the diffusing species (~10-100X).[8–10]

Expanding this work to incorporate reaction kinetics contributing to the changing species concentration gives,

$$\frac{\partial c}{\partial t} = \frac{\partial}{\partial x}\left(D\frac{\partial c}{\partial x}\right) - R\,, \tag{2-5}$$

where $R$ is rate at which a species is consumed, where, in the case of photopolymerization it represents the rate of polymerization, $R_\mathrm{p}$.[11–13] At steady state, the rate of radical species generation is equivalent to the rate of termination and the concentration of radical species is therefore constant given, again, that $c$ is monomer concentration. Combining this assumption with constant diffusion, the species consumption becomes

$$0 = D\frac{\partial^2 c}{\partial x^2} - R_\mathrm{p}. \tag{2-6}$$

This relationship governs the spatial distribution of polymer in an SLA system, the goal of which is to create a layer of polymer that is a close approximation of the photopattern design, producing high-fidelity features. However, photopolymerization and subsequent diffusion of species do not naturally result in a polymer distribution that is a close copy of the optical dose. To understand the relationship between reaction-diffusion kinetics and feature fidelity, consider two limiting cases: (1) polymerization occurs much more rapidly than diffusion and (2) the polymerization rate is much lower than the diffusion rate.

When the rate of reaction is much faster than diffusion, radical species react before they can diffuse outside of the illuminated region. This is the ideal printing environment for SLA because it ensures high-fidelity. This is the reason why most SLA printing materials have much higher viscosity and lower diffusivity than the hydrogel precursors considered here. Since high viscosity is not possible in the high solvent conditions used here, instead this work shows that a highly reactive monomer can overcome the high diffusion transport rate. Additionally, high illumination intensity can increase reaction rate, however this is often limited by light source availability and cytocompatibility.

Conversely, when the diffusion rate is comparable to or much faster than the reaction rate, species can move into and out of the photo pattern during the reaction. This transport blurs the edges of the patterned material in at least two ways: diffusion of monomer into the pattern and diffusion of radical species out. These processes, not optical diffraction, typically limit the resolution (the minimum distance between features) and critical dimension (the minimum isolated feature size) of the SLA process.

This work is particularly concerned with patterning hydrated gels for cellular biology applications, and therefore the viscosity of the precursor solution is similar to water with

diffusion rates for small molecules that are correspondingly quite fast in comparison to traditional SLA resins (~100 $\mu m^2/s$ vs. 0.01 $\mu m^2/s$, respectively).[14] Therefore, high-fidelity hydrogel features are only attainable if the reaction rate can be is increased with respect to the rapid diffusion rate. Unfortunately, the reaction rate in hydrogels is reduced relative to traditional SLA resins because of high water content and thus low monomer concentration dictated by cytocompatibility. Initiator concentrations in cytocompatible gels are similarly limited in order to constrain the radical concentration.[15] Thus, the only means to increase the reaction rate are by choosing high-reactivity species and/or by increasing the illumination within a range of cytocompatible intensities.

*2.2.2 Beer-Lambert Absorption*

SLA 3D printing confines polymerization to a 2D layer by adding a strong absorber. It is generally preferred that this absorber not photo-bleach because minimum layer thickness is constrained by maximum achievable absorbance and also because bleaching would needlessly complicate the printing process. Without bleaching, this absorption causes exponential decay of intensity with depth according to the Beer-Lambert law as

$$\mathrm{I}(z) = \mathrm{I}_0 e^{-\alpha[A]z}, \tag{2-7}$$

where $\mathrm{I}_0$ (mW $cm^{-2}$) is the incident intensity, $[A]$ is the molar concentration of a light-absorbing species, and $\alpha$ (L $mol^{-1}$ $cm^{-1}$) is the molar absorptivity of species $A$.[3] Assuming that the steady state propagation rate scales as $I^m$ and that conversion increases linearly with exposure time at the low conversion levels typical prior to gelation, the "effective dose" to reach gelation can be written[3]

$$\mathrm{E}_C = I^m\, t. \tag{2-8}$$

The thickness of a layer defined by the material conversion reaching the gel point at a depth $z = C_d$ can be determined by combining these two equations as

$$C_d = \frac{D_p}{m} \ln\left[\frac{E_{max}}{E_C}\right], \tag{2-9}$$

where $E_{max} \equiv I_0^m\, t$ is the effective dose at the illuminated surface of the material. In the SLA literature, the sublinear dependence of conversion on intensity is typically ignored and the material response is assumed to be reciprocal, or $m \equiv 1$. This derivation shows that the "working curve[2]" derived by experimentally determining the parameters of Equation (1-9) can be applied even in the case of sublinear material response with appropriate definition of an effective depth of penetration $D_p/m$ and effective dose $E \equiv I^m\, t$. The primary point of this discussion is that the available printer intensity ($I_0$), desired print time per layer ($t$), desired layer depth ($C_d$), the gel conversion fraction and the linearity of the intensity response ($m$) are coupled by Equation 1-9 and must be jointly optimized. [2,16–18]

## 2.3 Projection Stereolithography System Design

### *2.3.1 Design Specifications*

Projection SLA printers are simple optical systems that require a controlled exposure source, programmable mask or spatial light modulator, and relaying optics to image a mask pattern onto the sample plane (**Figure 2.1**). This system is intended to print materials for regenerative medicine, which therefore influences the choice of each component and design consideration of the SLA system. Design trade-offs are discussed in the following sections, with the final SLA system diagram show in **Figure 2.1.**

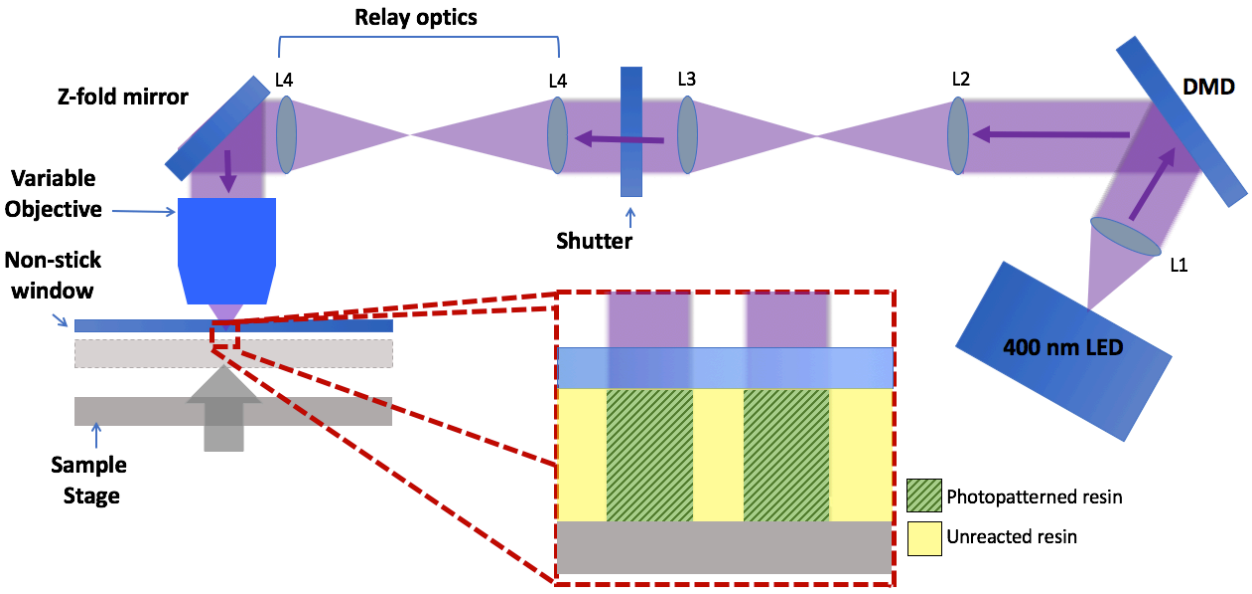

**Figure 2.1** Projection SLA-AM system diagram, where the programmable digital micromirror device (DMD) projects a 2D cross-section using a cytocompatible light source through a series of relaying-optics, through an interchangeable objective, and into a photopatternable material.

2.3.1.1 Resolution and Minimum Feature Size

Resolution and critical dimension are two specifications often used interchangeably in the literature, but they are not equivalent. Resolution defines how closely two features can be patterned while remaining resolvable to an external detector (*e.g.*, photodetector, atomic force microscope, etc.). Critical dimension is the smallest, independent feature that a printer can produce. The lower limit to both quantities, for an ideal perfect fidelity material, is set by optical diffraction of the image on the sample plane.

Considering the case where two pixels are projected by an optical system with a rectangular optical transfer function, the Sparrow criterion states they are just resolved when the sum of the two diffraction maxima produce a flat intensity profile, resulting in

$$r = \frac{0.47\,\lambda}{n \sin\theta} = \frac{0.47\,\lambda}{NA} \tag{2-10}$$

as the diffraction-limited optical resolution. The system elements that define this equation are $\lambda$, illumination wavelength, and $n \sin\theta$, numerical aperture $(NA)$, of the projection system given its angular extent $(\sin\theta)$ and index of refraction of the medium (air)$(n)$.[19]

Because cells are on the order of ~10 μm in diameter, printing hydrogel structures below this length-scale is not required, while the ability to print small structures (<5 μm) is ideal for structural, acellular constructs. Given an illumination wavelength of 405 nm, the NA of the system would need to be only 0.04, and therefore the system is never limited by optical diffraction.

To enable of NAs and different DMD pixel magnifications, the system built for this work incorporated a microscope objective turret. This allows for both large structure with large critical dimensions and small structures with small critical dimensions to be printed. The objectives were chosen for approximately equal parfocal distances to ensure minimal variations in the system focal plane when changing objectives. These system requirements, in addition (2-9), guide the choice of exposure source to optimize resolution, while maintaining a cytocompatible environment.

2.3.1.2 Intensity and wavelength

A cytocompatible exposure wavelength and intensity are required because the system is intended to print biomaterials. Near ultraviolet (e.g. i-line or 365 nm) sources are traditionally used for SLA printing due to fast initiation into UV absorbers using argon ion lasers that, in the past, had higher power than laser diodes available in the blue. However, energetic UV photons are known to damage cells and reduce their viability at intensities greater than 20 mW/cm$^2$.[15,20] 405 nm light has been shown to not significantly affect cell viability for $I_0 = 20$ mW/cm$^2$ and was hence chosen for the photopatterning source.[21,15,22]

2.3.1.3 Depth of Focus

Aside from the absorptive properties of the printing material, the layer thickness depends on the system depth of focus ($DOF$), which is the axial range of projected image focus. In a pixel-limited projection system, the $DOF$ is defined as

$$DOF = 2\mathrm{p}\, f/\# = \frac{2\mathrm{p}\, f}{\mathrm{D}} \approx \frac{\mathrm{p}\, n}{\mathrm{NA}}, \tag{2-11}$$

where p is the pixel size, f-number, $f/\# = \frac{f}{\mathrm{D}}$, $f$ is the effective focal length, D is the aperture diameter, and $f/\# \approx \frac{n}{2\ \mathrm{NA}}$ if the system NA is small. [23]

Because numerical aperture ($NA$) and $DOF$ are inversely proportional, variations in the $NA$ linearly change the $DOF$, affecting the maximum layer thickness by the same factor. Because layer thickness is approximately inversely proportional to printing speed, maximizing layer thickness also maximizes the printing speed. Using Equation (2-9), the $DOF$ can also be related to minimum features size,

$$r = \frac{0.47\ \lambda\ DOF}{\mathrm{p}n}, \tag{2-12}$$

which indicates a trade-off between minimum feature size and maximum printing speed. Assuming a pixel size on the sample, p, of 5 μm, $n = 1$ in air, and $\lambda = 405$nm, increased layer thickness reduces printing speed in an inversely linear relationship (**Figure 2.2**). By designing the system to support a variety of objectives with different numerical apertures, the $DOF$ can be varied to accommodate either fast, low resolution prints or slow, high resolution prints.

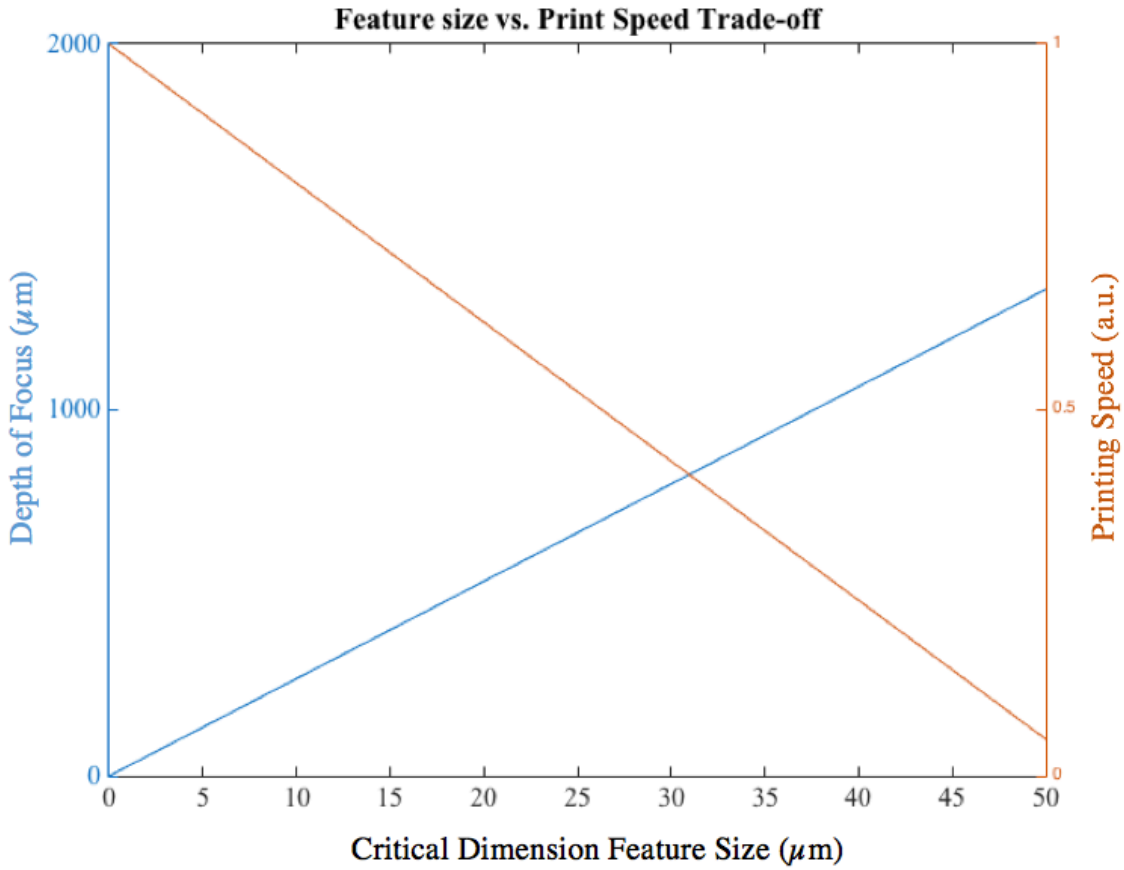


**Figure 2.2** Plot depicting the tradeoff between desired critical dimension feature size and printing speed.

2.3.1.4 Spatial Light Modulator (SLM)

The dimensions and pixel size on the sample (PSS) of the final printed structure are defined by programmable mask or spatial light modulator (SLM), which contains a finite number of pixels of finite size. The PSS proportionally increases with total area projection size and increases the critical dimension of the printed structure if large fabrications are required. This tradeoff translates directly into printing throughput because large SLMs support large printing areas and thus large final structures in addition to multiple, small structures in a single print cycle, which decreases total printing time. Therefore, to increase printing speed, the total number of pixels on the SLM must be maximized assuming the total power output is held constant (i.e., the illumination source power can be increased for an increased SLM size).

The two most common SLM technologies are liquid crystal displays (LCD), that are found in most commercial projection systems, and micro electro-mechanical systems such as the

digital micromirror device (DMD). Because LCDs use the polarization-dependent properties of liquid crystals, they require the incident light to be polarized, which reduce the pattern exposure intensity by a factor of two if using common, unpolarized light sources such as LEDs.[24] DMDs are not polarization-dependent and consist of an array of square, electronically bi-stable micromirrors. To projection a pattern, the array of electro-mechanical micromirrors will switch to an 'on' state that sends light to the desired sample plane or to an 'off' state that send light to an absorber, which represent white and black regions of the photopattern, respectively. The pixels switch across their diagonal axis and require incident light be oriented along this axis in a non-planar system geometry. Recent DMD designs have overcome this issue by rotating the pixels 45 degrees, which allow incident light to be oriented in the plane of the projection system. For these reasons, this work uses a pixel-rotated DMD projection source (Texas Instruments, DLP 0.3 WVGA Series 220 DMD) to maximize the total intensity at the sample plane for the 405 nm exposure source and minimize the SLA printer size.

## 2.4 System Characterization and Calibration

### *2.4.1 Illumination Characterization*

Due to the large cone-angle illumination of LEDs, the intensity across the photopatterned exposure field is non-uniform. A DataRay beam profiler was used to measure the intensity pattern with the DMD pixels set to a uniform level. The grayscale feature of the DMD was used to produce a uniform intensity across the field (**Figure 2.3**). Due to the significant intensity roll-off at the photopattern edges (70%), the total intensity of the image must be reduced by as much to produce a flat intensity field. The photopattern is confined to the ~25% of the total projection area to maximize intensity output and to limit intensity roll-off at the edges to <15%.

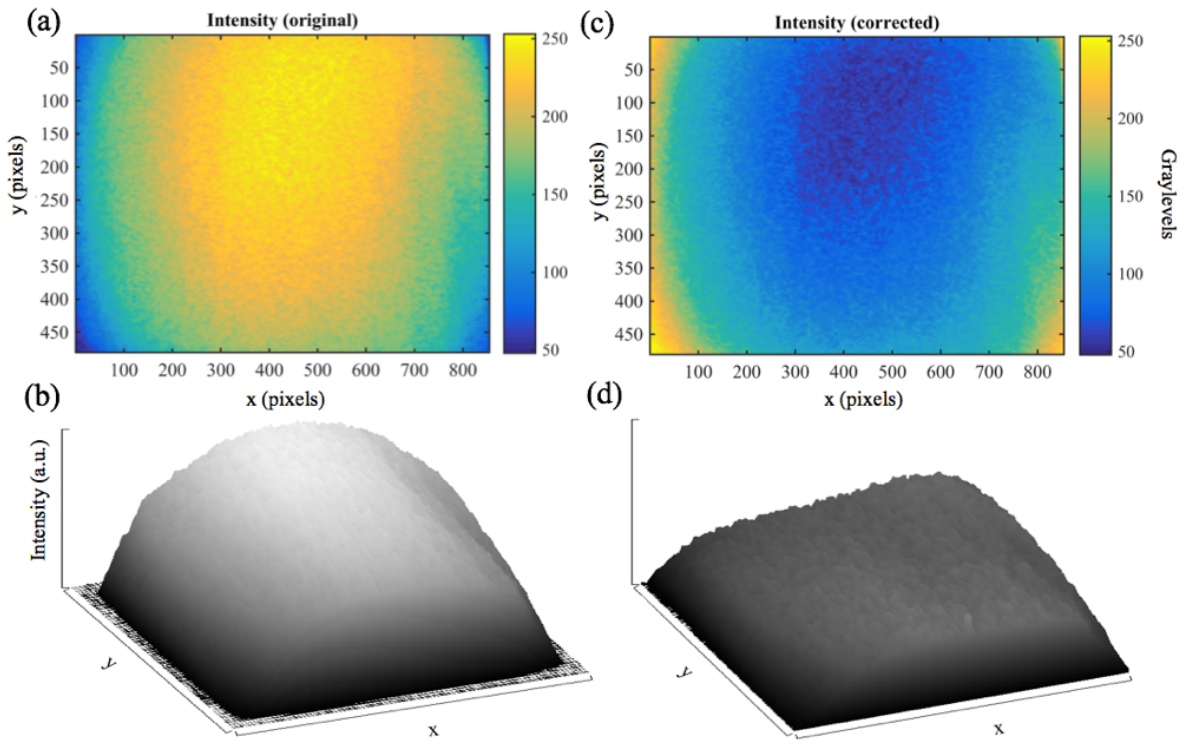


**Figure 2.3** (a) Depicts intensity variations across the full exposure field at the sample plane as a function of graylevel (0-256) that are input to the correction algorithm with (b) a 3D depiction of the original intensity variation. (c) Depicts the generated corrected intensity photomask with the subsequent (d) flattened intensity variation at the sample plane.

### *2.4.2 Focus Characterization*

The focus is characterized using a commercial negative photoresist (AZ4210) sensitive to 400 nm. The photoresist is deposited onto a glass substrate and spun at 6000 rpm for 30s to create a layer thickness of ~2 µm followed by a soft-bake at 100 degrees C for 90s. The samples are then exposed to a resolution photopattern at 20 mW/cm$^2$ for 30s (600 mJ/cm$^2$). To verify the best focus of the system, a series of resolution pattern exposures is done across the sample at different defocus steps (**Figure 2.4**). Two objectives with different magnifications, 5X and 1X, were tested to determine the ability to modify the photopattern total projection area in exchange for increased pixel size on the sample (**Figure 2.4**b-c). Due to the diagonal, rotated orientation of the DMD pixels, straight lines in the bitmap photopattern appear as a saw-tooth edge, which allows observation of pixel-limited resolution. As pixel size on the sample plane increases, the pixel features become visible because the photoresist response is sensitive at these length-scales.

**Figure 2.4c** displays said features, where the distance between pixels and the mirror etching holes at their center are visible.

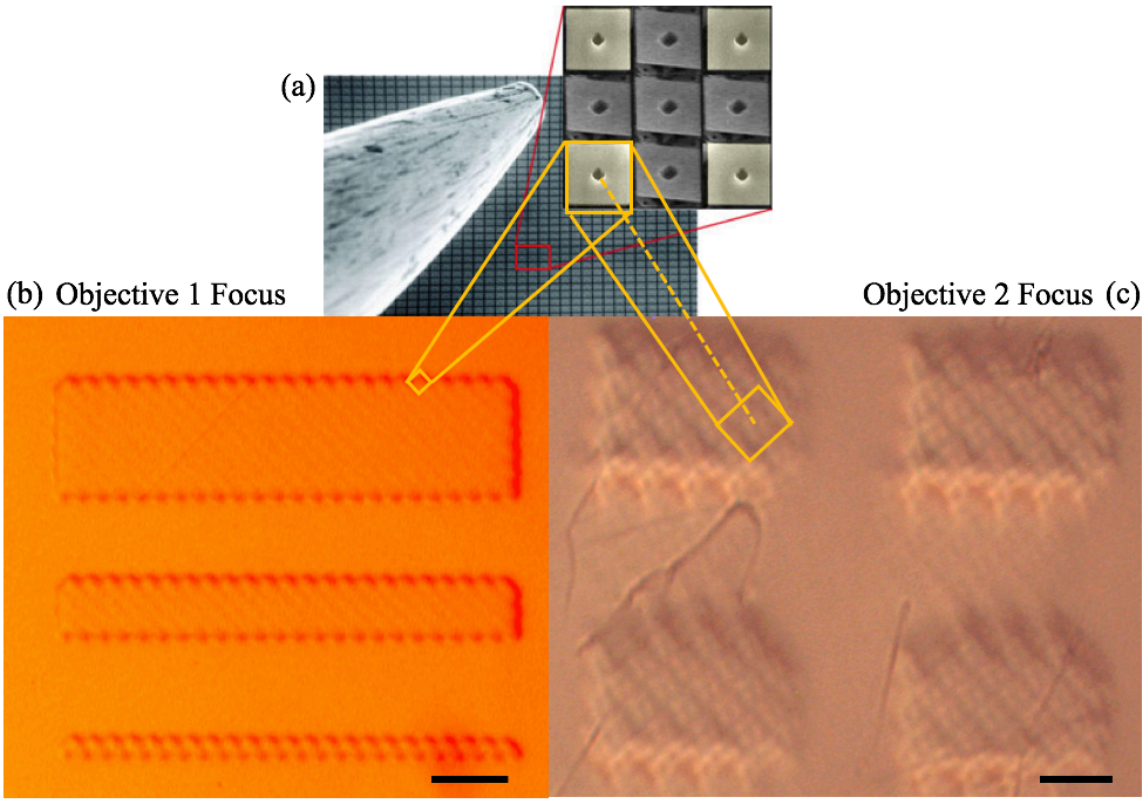


**Figure 2.4** (a) Depicts image and scaling of DMD pixels in their 'on' 'off' states. (b) and (c) are DIC images of focus test using a commercial photoresist (AZ4210), where the samples were iteratively exposed a series of times to determine the best focus of the system demonstrating the ability to pattern using two different objectives (scale bar corresponds to 20 μm).

## 2.5 Conclusion

SLA 3D printing is a simple platform to design and build both prototypes and functional devices. It is an ideal system to print structures for regenerative medicine because it supports printing both soft (10s kPa), cytocompatible hydrogels and stiff (100 MPa), structural biomaterials. With a deeper fundamental understanding of the transport kinetics during photopolymerization, this tool will enable the fabrication of tissues and tissue scaffolds that are unable to be built using other manufacturing systems.

## 2.6 References


1. Melchels, F. P. W., Feijen, J. & Grijpma, D. W. A review on stereolithography and its applications in biomedical engineering. *Biomaterials* **31,** 6121–6130 (2010).

2. Jacobs, P. Stereolithography 1993 : Epoxy Resins , Improved Accuracy & Investment Casting. (1993).

3. Odian, G. *Principles of Polymerization*. (A JOHN WILEY & SONS, INC., 2004).

4. Corbel, S., Dufaud, O. & Roques-Carmes, T. *Materials for stereolithography*. *Stereolithography* (2011). doi:10.1007/978-0-387-92904-0

5. Zhao, G. & Mouroulis, P. Diffusion Model of Hologram Formation in Dry Photopolymer Materials. *J. Mod. Opt.* **41,** 1929–1939 (1994).

6. Anseth, K. S. *et al.* Kinetic evidence of reaction diffusion during the polymerization of multi(meth)acrylate monomers. *Macromolecules* **27,** 650–655 (1994).

7. Balluffi, Robert, W., Samuel, M., Allen & Craig Carter, W. Solutions to the Diffusion Equation - Solutions to Fick ' s Laws. *Kinet. Mater.* 1–18 (2006).

8. Peppas, N. A. & Reinhart, C. T. Solute diffusion in swollen membranes. Part I. A new theory. *J. Memb. Sci.* **15,** 275–287 (1983).

9. Zhou, Y. *et al.* Establishment of a Physical Model for Solute Diffusion in Hydrogel: Understanding the Diffusion of Proteins in Poly (Sulfobetaine Methacrylate) Hydrogel. *J. Phys. Chem. B* acs.jpcb.6b10355 (2017). doi:10.1021/acs.jpcb.6b10355

10. Skaalure, S. C. & Engineering, B. Tuning Hydrogel Degradation for Cartilage Tissue Engineering by. (2014).

11. Wilemski, G. On the derivation of Smoluchowski equations with corrections in the classical theory of Brownian motion. *J. Stat. Phys.* **14,** 153–169 (1976).

12. Achilias, D. S. A Review of Modeling of Diffusion Controlled Polymerization Reactions. *Macromol. Theory Simulations* **16,** 319–347 (2007).

13. Zubtsov, D. A. *et al.* Effect of mixing on reaction-diffusion kinetics for protein hydrogel-based microchips. *J. Biotechnol.* **122,** 16–27 (2006).

14. Tang, Y. Stereolithography cure process modeling. (2005). at <http://smartech.gatech.edu/handle/1853/7235>

15. Bryant, S. J., Nuttelman, C. R. & Anseth, K. S. Cytocompatibility of UV and visible light photoinitiating systems on cultured NIH/3T3 fibroblasts in vitro. *J. Biomater. Sci. Polym. Ed.* **11,** 439–457 (2000).

16. Liska, R. *et al.* Photopolymers for rapid prototyping. *J. Coatings Technol. Res.* **4,** 505–510 (2007).

17. Stampfl, J. *et al.* Photopolymers with tunable mechanical properties processed by laser-based high-resolution stereolithography. *J. Micromechanics Microengineering* **18,** 125014 (2008).

18. Zabti, M. M. Effects of Light Absorber on Micro Stereolithography Parts A Thesis Submitted to The University of Birmingham for the Degree of Doctor of Philosophy By Mohamed Mohamed Zabti. (2012).

19. Sparrow, C. M. On spectroscopic resolving power. *Astrophys. J.* **44,** 76–86 (1916).

20. Editors, S., Bhatia, S., Chen, C., Liu, V. A. & Bhatia, S. N. Hybrid Bio/Arti®cial Microdevices: Three-Dimensional Photopatterning of Hydrogels Containing Living Cells. *Biomed. Microdevices* **4,** 257–266 (2002).

21. Linnenberger, A. Live cell lithography and non-invasive mapping of neural networks. (University of Colorado Boulder, 2014).

22. Fairbanks, B. D., Schwartz, M. P., Bowman, C. N. & Anseth, K. S. Photoinitiated polymerization of PEG-diacrylate with lithium phenyl-2,4,6-trimethylbenzoylphosphinate: polymerization rate and cytocompatibility. *Biomaterials* **30,** 6702–6707 (2009).

23. Depth of Field and Depth of Focus | Edmund Optics. at <https://www.edmundoptics.com/resources/application-notes/imaging/depth-of-field-and-depth-of-focus/>

24. Nikolenko, V., Peterka, D. S. & Yuste, R. A portable laser photostimulation and imaging microscope. *J. Neural Eng.* **7,** 45001 (2010).

# Chapter 3 - Photopatterned Hydrogel: Transport Kinetics Model

## 3.1 Executive Summary

Unlike traditional stereolithography (SLA) 3d printing of high viscosity acrylates that converts to glassy solids when polymerized, the goal of this thesis is to pattern low viscosity hydrated precursors (i.e., high solvent concentration) into low modulus gels that, initially, may be far from equilibrium swelling. This leads to three challenges in the recording of high fidelity structures: 1) the diffusion of photo-generated radical species out of the illuminated region, 2) the diffusion of species consumed by photo-initiated reactions into the illuminated region, and 3) the differential swelling of crosslinked polymer regions. To characterize these coupled effects, the work in this chapter shows that the reaction-diffusion equation set can be simplified to first-order steady-state reaction diffusion models for the first two effects. This work also shows that the impact of swelling on recorded micro-patterns can be understood from equilibrium swelling measurements of bulk samples. A characteristic distance is predicted for each of the three effects and these are compared in Chapter 5 to experimental results.

## 3.2 Introduction

There is a growing need in the regenerative medicine and personalized medicine community to locally control the mechanical and chemical properties of the extracellular matrix surrounding cells.[1–3] While this need has been addressed in part by fused deposition modelling (FDM) or 'bio-plotting' printers, the material constraints surrounding this technique severely inhibit its ability to recapitulate the microenvironment of cells.[4,5] Stereolithography does not have the same material constraints and is the subject of current research involving tools for tissue engineering.[6]

Traditional SLA resins have nearly 100% monomer concentration and are highly viscous (~1000 cPs) in order to minimize diffusion of species during photopatterning to produce high-fidelity printed features. However, printing cytocompatible precursor materials is inherently different because cells require an environment with >70% water to live.[7] High concentrations of water and low concentrations of monomer in the printing solution subsequently decreases the resin viscosity (~1cPs), increases diffusivity, and decreases polymerization rates. These factors

combine to effectively reduce the ability to fabricate high-fidelity photopatterned features in cytocompatible materials due to the swelling and diffusion that occur during polymerization.

This chapter presents a model to predict how printing fidelity is affected by precursor solution reactivity, diffusivity, and swelling during polymerization. The photopolymerization reaction kinetics developed by Reddy et al. for a known, cytocompatible photo-clickable chemistry, thiol-norbornene, are first discussed to obtain the relationship between reaction rate and species concentration. Diffusion during polymerization is then shown to simplify to first-order steady state reaction diffusion kinetics, modelling diffusion of species into and out of the photopattern shown in **Figure 3.1**(1). Differential swelling after polymerization is also modeled assuming bulk equilibrium swelling properties for the photopatterned material are known (**Figure 3.1**(2)). In Chapter 5, these models are then compared to experimental data.

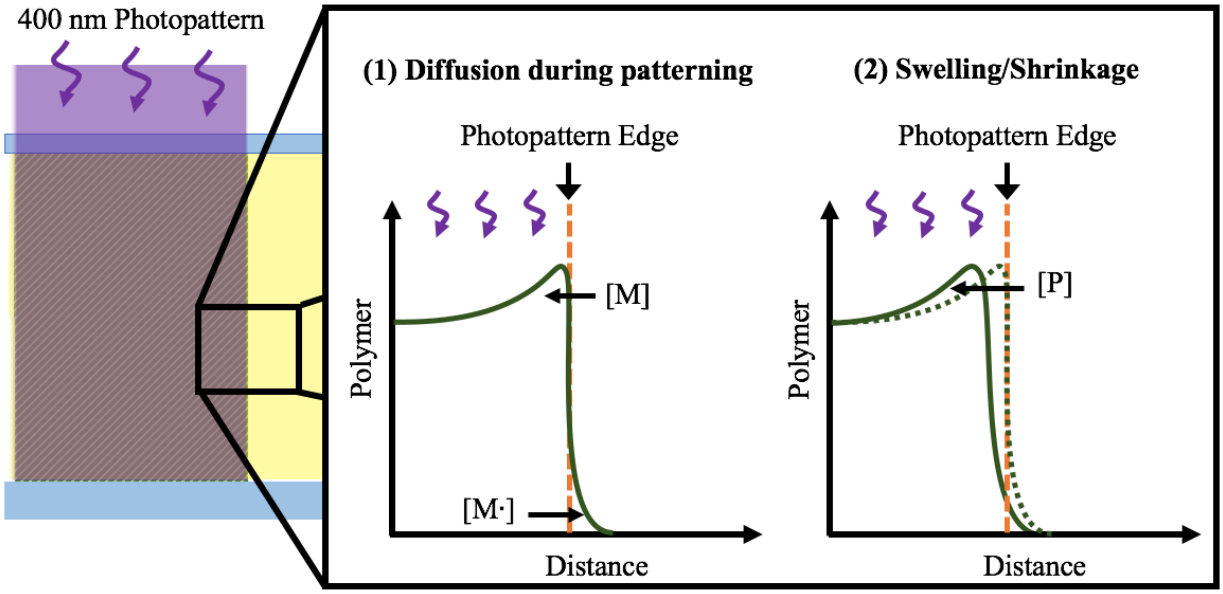


**Figure 3.1** Illustration depicting (1) diffusion of species [M] into and [M·] out of the photopattern and (2) differential swelling occurring due to enhanced crosslinking inside of the photopattern resulting in the movement of the polymer network [P] away from the pattern edge.

## 3.3 Modelling Kinetics

### *3.3.1 Materials*

Hydrogel precursor solutions are inherently difficult to print using SLA due to their low solids content and high diffusivity, since these reduce reaction rate and increase transport rates

respectively. Linnenberger showed that SLA of poly(ethylene)-glycol methacrylate (PEDMA) hydrogel to ~10 micron feature size requires a uniform pre-exposure to just below gelation in order to increase oligomer molecular weight and solution viscosity.[8] However, out-diffusion of oligomer from an initial photo-pattern significantly changes the gelation threshold and resolution of subsequent exposures, severely complicating the multiple patterning steps needed for three-dimensional (3D) SLA. Thus, in this work, poly(ethylene)-glycol (PEG) thiol-norbornene photo-clickable polymerization is chosen for three reasons. (1) Photo-clickable step-growth polymerizations offer enhanced control of property variations with respect to chain-grown reactions because precise off-stoichiometry can be engineered and an excess number of functional groups can be accurately predicted. (2) Photopolymerized PEG-thiol-norbornene hydrogels are cytocompatible, which is required for printing encapsulated cells.[9–11] (3) The thiol-norbornene reaction has the highest reactivity of all thiol-ene reaction ($k_p \cong 10^6$ $M^{-1}$ $s^{-1}$), significantly greater than meth-acrylates ($k_p \cong 10^2$ $M^{-1}$ $s^{-1}$) and acrylates ($k_p \cong 10^3$ $M^{-1}$ $s^{-1}$).[12] Additionally, the lithium acylphosphinate (LAP) photoinitiator was also chosen for its cytocompatibility and because it initiates at visible wavelengths (400 nm), which are known to be more cytocompatible than UV wavelengths (~ 365 nm).[13]

*3.3.2 Photopolymerization kinetics*

Cramer et al. and Reddy et al. elegantly modeled and experimentally verified the complex polymerization kinetics of thiol-ene step growth polymerizations.[12,14] This photo-clickable polymerization employs the addition of a thiyl radical to a vinyl functional group via propagation ($k_p$) (step 1), followed by radical chain transfer ($k_{CT}$) from the radical carbon produced in step 1 to a thiol functional group (step 2)[12]:

(propagation)

$$RS\bullet + R'CH = CH_2 \xrightarrow{k_p} R'C\bullet H - CH_2SR \qquad \text{(step 1)}$$

(chain transfer)

$$R'C\bullet H - CH_2SR + R''SH \xrightarrow{k_{CT}} R'CH_2 - CH_2SR + R''S\bullet, \qquad \text{(step 2)}$$

where $R''$, R′ and R non-reactive groups of the molecules, $\mathrm{C}=\mathrm{C}$ and SH are the radical-sensitive functional groups vinyl and thiol, respectively, with C• and S• indicating the radical carbon and thiyl species, respectively.

As discussed in Chapter 2, initiation, propagation (steps 1 and 2), and termination govern photopolymerization reaction kinetics. Thiol-ene step-growth photopolymerization employs radical photoinitiation, whose rate is defined as

$$\mathrm{R}_i = -\frac{d[\mathrm{I}]}{dt} = \frac{2.303 f \epsilon [I] \mathrm{I}_0 \lambda}{N_{\mathrm{AV}} h c}, \tag{3-1}$$

where $[I]$ is the concentration of photoinitiator ([LAP]) in the solution, $f$, efficiency, and $\epsilon$, molar absorptivity, are 0.8 and 470 L mol$^{-1}$ cm$^{-1}$, based on standard values for LAP.[19,20] Also in Equation (5-1), $\mathrm{I}_0$ is the incident illumination intensity (mW cm$^{-1}$) and $N_{\mathrm{AV}}$, $h$, and $c$ are Avogadro's number, Planck's constant and the speed of light, respectively.

The concentration of the four species, [SH], [CC], [S•], and [C•], is governed by the following equations[14]:

$$\frac{d[\mathrm{SH}]}{dt} = -k_{\mathrm{ct}}[\mathrm{C}\bullet][\mathrm{SH}]\ , \tag{3-2}$$

$$\frac{d[\mathrm{CC}]}{dt} = -k_{\mathrm{p}}[\mathrm{S}\bullet][\mathrm{CC}], \tag{3-3}$$

$$\frac{d[S\bullet]}{dt} = \mathrm{R}_i - \mathrm{R}_{\mathrm{t}}(\mathrm{S}\bullet) + k_{\mathrm{ct}}[\mathrm{C}\bullet][\mathrm{SH}] - k_{\mathrm{p}}[\mathrm{S}\bullet][\mathrm{CC}], \tag{3-4}$$

and

$$\frac{d[\mathrm{C}\bullet]}{dt} = \mathrm{R}_i - \mathrm{R}_{\mathrm{t}}(\mathrm{C}\bullet) - k_{\mathrm{ct}}[\mathrm{C}\bullet][\mathrm{SH}] + k_{\mathrm{p}}[\mathrm{S}\bullet][\mathrm{CC}]. \tag{3-5}$$

Where the termination rate of thiyl and carbon-centered radicals, $\mathrm{R}_t(\mathrm{S}\bullet)$ and $\mathrm{R}_t(\mathrm{C}\bullet)$, are defined as

$$\mathrm{R}_{\mathrm{t}}(\mathrm{S}\bullet) = 2k_{\mathrm{t1}}[\mathrm{S}\bullet]^2 + k_{\mathrm{t2}}[\mathrm{S}\bullet][\mathrm{C}\bullet] \tag{3-6}$$

and

$$\mathrm{R}_{\mathrm{t}}(\mathrm{C}\bullet) = k_{\mathrm{t2}}[\mathrm{S}\bullet][\mathrm{C}\bullet] + 2k_{\mathrm{t3}}[\mathrm{C}\bullet]^2, \tag{3-7}$$

where $k_{\mathrm{t1}}$, $k_{\mathrm{t2}}$, and $k_{\mathrm{t3}}$ are the bimolecular termination rate parameters for thiyl-thiyl, thiyl-carbon, and carbon-carbon radical recombination, respectively.[15] The rate at which all radicals terminate, independent of species, is thus the sum of (5-6) and (5-7),

$$\mathrm{R}_{\mathrm{t}} = \mathrm{R}_{\mathrm{t}}(\mathrm{S}\bullet) + \mathrm{R}_{\mathrm{t}}(\mathrm{C}\bullet) = 2k_{\mathrm{t1}}[\mathrm{S}\bullet]^2 + 2k_{\mathrm{t2}}[\mathrm{S}\bullet][\mathrm{C}\bullet] + 2k_{\mathrm{t3}}[\mathrm{C}\bullet]^2. \tag{3-8}$$

The polymerization rate ($R_p$) of this reaction related to individual radical concentrations is

$$R_p = k_{ct}[C\bullet][SH] = k_p[S\bullet][CC], \tag{3-9}$$

given the rates of thiol and vinyl group consumption are equivalent.[14] In steady state, the rate at which radicals are generated is equal to the rate at which radicals are terminated ($R_i = R_t$), or equations (5-4) and (5-5) = 0. Solving for $[S\bullet]$, $[C\bullet]$, and combining (5-1) through (5-9), the stead state polymerization rate, $R_{p,s}$, is found to be

$$R_{p,s} = \sqrt{\frac{R_i}{2}}\left(\sqrt{\frac{\boldsymbol{k_{t1}}}{(\boldsymbol{k_p}[\mathbf{CC}])^2} + \frac{\boldsymbol{k_{t2}}}{\boldsymbol{k_p k_{ct}}[\mathbf{CC}][\mathbf{SH}]} + \frac{\boldsymbol{k_{t3}}}{(\boldsymbol{k_{ct}}[\mathbf{SH}])^2}}\right)^{-1}. \tag{3-10}$$

Reddy et al. identified that each termination mechanisms must be equivalent in thiol-norbornene chemistries ($k_{t1} = k_{t2} = k_{t3}$) and that both propagation and chain transfer polymerizations are equally likely ($k_p = k_{ct}$) thus, $R_p$ simplifies to [13,15]

$$R_{p,s} = \sqrt{\frac{R_i}{2k_t}}k_P\left(\sqrt{\frac{1}{[CC]^2} + \frac{1}{[CC][SH]} + \frac{1}{[SH]^2}}\right)^{-1}. \tag{3-11}$$

With the steady state polymerization rate of the thiol-norbornene reaction, the steady state concentrations of the carbon-centered $[C\bullet]$ and the thiyl radicals $[S\bullet]$, is determined by substituting (5-11) into using (5-9) and solving for each radical species,

$$[C\bullet]_s = \frac{R_{p,s}}{k_{ct}[SH]} = \frac{R_{p,s}}{k_P[SH]}, \tag{3-12}$$

where $[S\bullet]_s$ is equivalently related to [CC].

For a given formulation and illumination intensity, the steady-state concentrations of the thiol-norbornene reaction are thus fully determined by the initiation rate (5-1), the polymerization rate (5-11) and the two radical concentrations $[S\bullet]_s$ and $[C\bullet]_s$ (5-12). The initiation rate constants for LAP are given above and Cramer et al. and Reddy et al. gives the termination constant ($k_t$ = 3.5 X $10^8$ L $mol^{-1}$ $cm^{-1}$) and polymerization rate constant ($k_t$ = 0.5-3.1 X$10^6$ L $mol^{-1}$ $cm^{-1}$).[12,14] A fourth advantage of the thiol-norbornene reaction is thus the complete, quantitative understanding of the reaction which I use next to predict patterning fidelity in gels formed from this chemistry.

*3.3.3 Diffusion kinetics*

The goal of this section is to quantitatively describe processes that will blur the polymer pattern resulting from a given intensity pattern, which reduce photopattern fidelity. The hydrogel initial conditions assumed are that monomer solution has swollen into an existing crosslinked, off-stoichiometry thiol-norbornene network expressing a known concentration of tethered thiol or norbornene functional groups (see Chapter 5). The new polymer pattern of interest is thus the concentration of thiol- and norbornene-attached monomers that react with the existing network due to the intensity pattern applied after the gel is swollen. Chosen here is a discrete intensity step as would occur at the edge of some more complex pattern.

This problem is qualitatively different than that encountered in traditional SLA. In typical SLA, exposure of liquid monomer solution creates a distribution of radical and terminated oligomers of various molecular weights, all of which then diffuse out of the photo-pattern as replacement monomer diffuses in. The solution viscosity increases depending on the local molecular weight distribution, locally changing the diffusivity of all species. Eventually the material undergoes the phase transition to a gel, dramatically changing reactivities and diffusivities. The goal of a model would be to predict the physical boundaries and polymer properties of the gel.

Here the problem is considerably simpler because the gel is already formed. The goal of the model is to predict the distribution of polymer attached to an existing network by the propagation reaction. While small amounts of mobile low molecular weight polymer are generated, the concentration of network-bound and mobile reactive groups are comparable in the systems explored, resulting in most chains becoming immobile after a small number of reactions. We can thus approximate the complex reaction sequence as the first-order reaction of mobile monomers to tethered functional groups. Finally, there is no phase transition in this patterning environment nor the associated change of properties. Note that the gel phase of both traditional SLA and the hydrogels considered here can swell, resulting in a second category pattern blurring. For this portion of the model, the polymer 3D network is taken to be fixed.

The thiol-norbornene precursor solution is designed with an off-stoichiometric ratio of 0.5:1, [SH]:[CC] respectively, to ensure that 50% of the initial concentration of norbornene groups remain unreacted after initial polymerization. After initial polymerization, the hydrogel is

then swollen with fresh precursor solution of the same formulation. Once the hydrogel is swollen to equilibrium, the assumed maximum effective concentration of thiol to norbornenes present is changed from 0.5:1 to 1/3:1 due to the presence of excess [CC] attached to the original hydrogel network. During polymerization, these concentrations change as functions of time dictated by the rate equations discussed previously.

The fluorescence detection method described in Chapter 5 quantifies the tethered thiol speices concentration after any untethered species have been removed by washing. At an intensity step, there are two cases of interest, then. First, thiyl radicals can diffuse out of the illuminated region and react with tethered ene functionality on the network in the dark. The thiyl concentration is $10^6$ times smaller than the tethered norbornene concentration, so this reaction may safely be considered first order in mobile thiyl concentration. Second, thiol monomer can diffuse from the dark and react with the tethered thiyl radicals in the light. The thiyl concentration is maintained at steady state by the illumination, so this reaction may be considered first order in mobile thiol concentration. The mathematical description of both processes is identical, so here I derive the behavior of the latter.

The diffusion and first-order reaction of the mobile thiol with the immobile network of carbon-centered radicals can be described as,

$$0 = \frac{1}{r^{n-1}}\frac{d}{dr}r^{n-1}D_{\mathrm{SH}}\frac{d}{dr}[\mathrm{SH}] - k_{\mathrm{P}}[\mathrm{SH}][\mathrm{C}\bullet]_s, \tag{3-13}$$

where r is distance from the illumination edge, $n$ = (1,2,3) is the spatial dimension, $D_{\mathrm{SH}}$ is the diffusion coefficient for thiol monomer and $k_p$ is the reaction rate constant between diffusing thiol and tethered carbon-centered radicals. This equation can be solved in closed form for species [SH] in 1, 2, and 3 dimensions from a source of radius $R$ using Bessel Functions of the first ($J_a$) and second kind ($Y_a$),

$$[\mathrm{SH}](r) = C[1]\, r^{\frac{2-n}{2}}\left[J_{\frac{1}{2}(n-2)}\left(-\mathbb{i}r\sqrt{\frac{k_{\mathrm{P}}[\mathrm{C}\bullet]_s}{D_{\mathrm{SH}}}}\right) - \mathbb{i}\, Y_{\frac{1}{2}(n-2)}\left(-\mathbb{i}r\sqrt{\frac{k_{\mathrm{P}}[\mathrm{C}\bullet]_s}{D_{\mathrm{SH}}}}\right)\right], \tag{3-14}$$

where $C[1]$ is a system- and dimensionality-defined constant relating to $\mathrm{J_{SH}}$( *i.e.*, $D_{\mathrm{SH}}$) and $\mathbb{i} = \sqrt{-1}$. Assuming a boundary of fixed flux through a radius R, the solution for $n$ = 1, 2, and 3 are

$$[\mathrm{SH}] = e^{\frac{R-r}{\sqrt{D_{\mathrm{SH}}/k_{\mathrm{P}}[\mathrm{C}\bullet]_s}}} \qquad n = 1, \tag{3-15}$$

$$[\mathrm{SH}] = \frac{K_0 \frac{r}{\sqrt{D_{\mathrm{SH}}/k_{\mathrm{P}}[\mathrm{C}\bullet]_s}}}{K_0 \frac{R}{\sqrt{D_{\mathrm{SH}}/k_{\mathrm{P}}[\mathrm{C}\bullet]_s}}} \qquad n = 2, \tag{3-16}$$

and

$$[\mathrm{SH}] = \frac{R}{r} e^{\frac{R-r}{\sqrt{D_{\mathrm{SH}}/k_{\mathrm{P}}[\mathrm{C}\bullet]_s}}} \qquad n = 3, \tag{3-17}$$

where $K_0$ is the Modified Bessel Function of the second kind, were the solutions are simplified to include the spatial dimension. We see that in all cases, the characteristic distance ($d_c$) thiol monomers can diffuse before reacting and immobilizing is

$$d_c = \sqrt{D_{\mathrm{SH}}/k_{\mathrm{P}}\,[\mathrm{C}\bullet]_s}, \tag{3-18}$$

which is shown as the radial diffusion distance scaling factor. The specific distribution of reacted thiols depends both on dimensionality and on the size of the source region relative to this characteristic distance (10:1, 1:1, and 0.1:1) as shown in **Figure 3.2**. **Figure 3.2**a show that when the source radius R is large in comparison to $d_c$, the distribution is independent of dimensionality because the boundary looks flat (n=1) on the scale of the transport. Conversely, when the source radius R is small relative to the transport distance $d_c$ as shown in **Figure 3.2**c, the thiols travel significantly less from the source as dimensionality increases because there is simply more volume to fill. This behavior is demonstrated experimentally in Chapter 5.

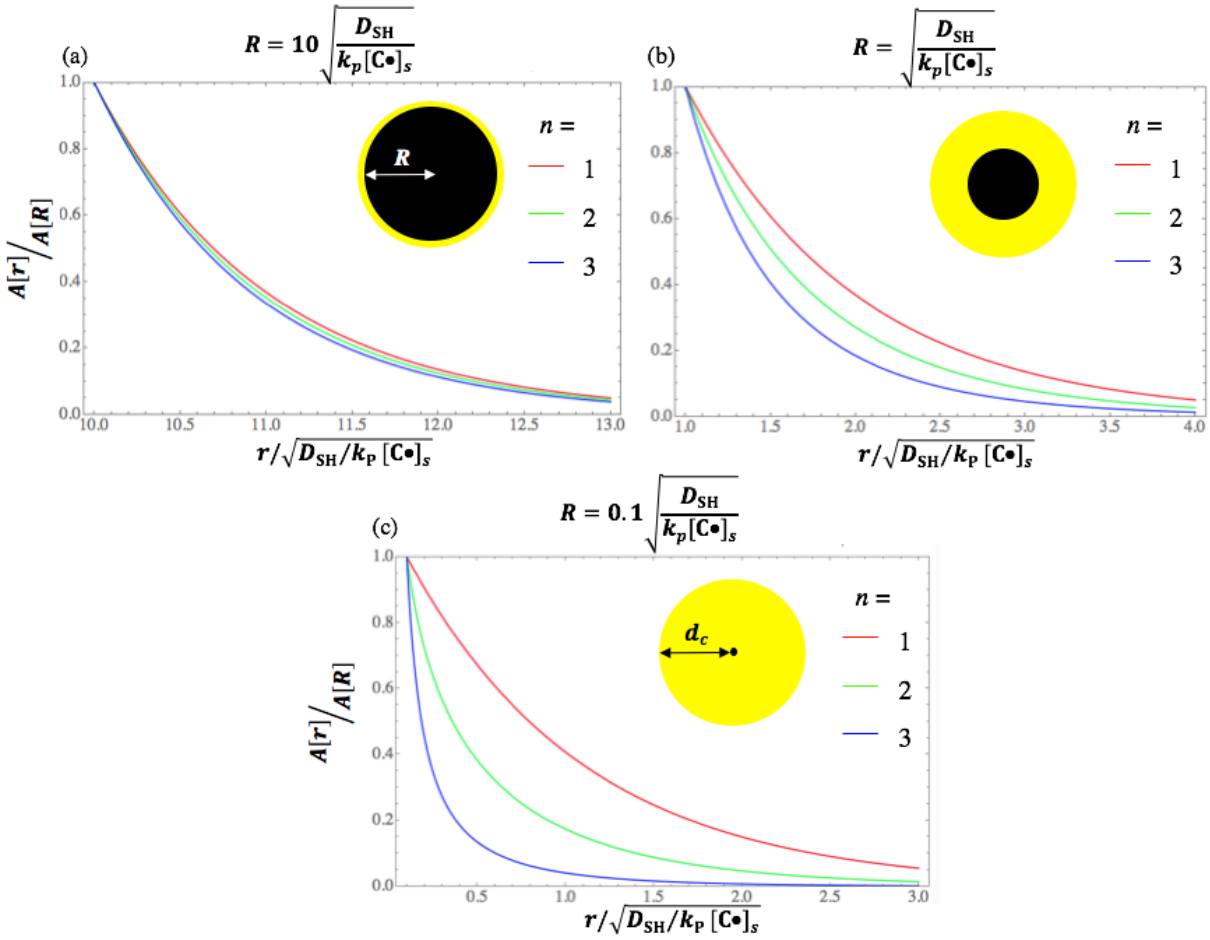


**Figure 3.2** Steady state concentrations of a diffusing species A as a function of distance r away from a constant flux surface of size R = 10, 1 and 0.1 times the characteristic distance in n = 1, 2, and 3 dimensions. Inset black circle indicates the current source and the yellow demonstrates $d_c$ extending beyond this source.

These results can be used to make quantitative predictions about the distance mobile thiols propagate into the illuminated photopattern and mobile thiyl radicals propagate into the dark before reacting. The distance by which the concentration of thiol monomer and thiyl radicals falls off to 1/e from a one-dimensional edge is equal to

$$d_{cSH} = \sqrt{\frac{D_{SH}}{k_P[C\cdot]_s}} \tag{3-19}$$

and

$$d_{cS\cdot} = \sqrt{\frac{D_{S\cdot}}{k_P[CC]}}, \tag{3-20}$$

respectively.

The two most important conclusions from this model are the distinctly different characteristic diffusion-reaction distances for radicalized species, S · and C ·, versus unreacted species, SH and CC (**Figure 3.3**). These distances vary because the steady-state thiyl radical concentration within the pattern is low with respect to the total concentration unreacted species outside of the photopattern, whereas monomer species diffusing into the pattern are at a comparable concentration to the attached radical species within the pattern due to off-stoichiometry. Therefore, diffraction-limited photopatterning should be possible given the short diffusion-reaction distance of thiyl radicals, which is on the order of nanometers.

Further, because $R_{p,s}$ and thus $[C\bullet]_s$ are proportional to $\sqrt{I_0}$, $d_c$ is predicted to increase by a fourth-root as incident exposure intensity increases ($d_c \propto \sqrt[4]{I_0}$). Equations 1-19 and 1-20 can be similarly derived for [CC] and $[C\cdot]_s$ as $d_{cCC}$ and $d_{cC\cdot}$, respectively. **Figure 3.3** is a plot these calculated distances tor typical intensities of $I_0 = 5, 10, \text{and } 20$ mW cm$^{-1}$ and typical concentrations of norbornene and thiol functional groups in high water content hydrogels (0.035 M and 0.07 M, respectively). The respective distances [CC] and [SH] propagate out of the photopattern before reacting are $10^3$ time greater than the distances $[C\cdot]_s$ and $[S\cdot]_s$ propagate out of the photopattern before terminating, shown in **Figure 3.3**. As expected, due to the low ratio of thiyl radical species diffusing out of the pattern to the total unreacted species concentration, the characteristic distance radicals can diffuse before terminating is negligibly affected by incident intensity variations (**Figure 3.3**).

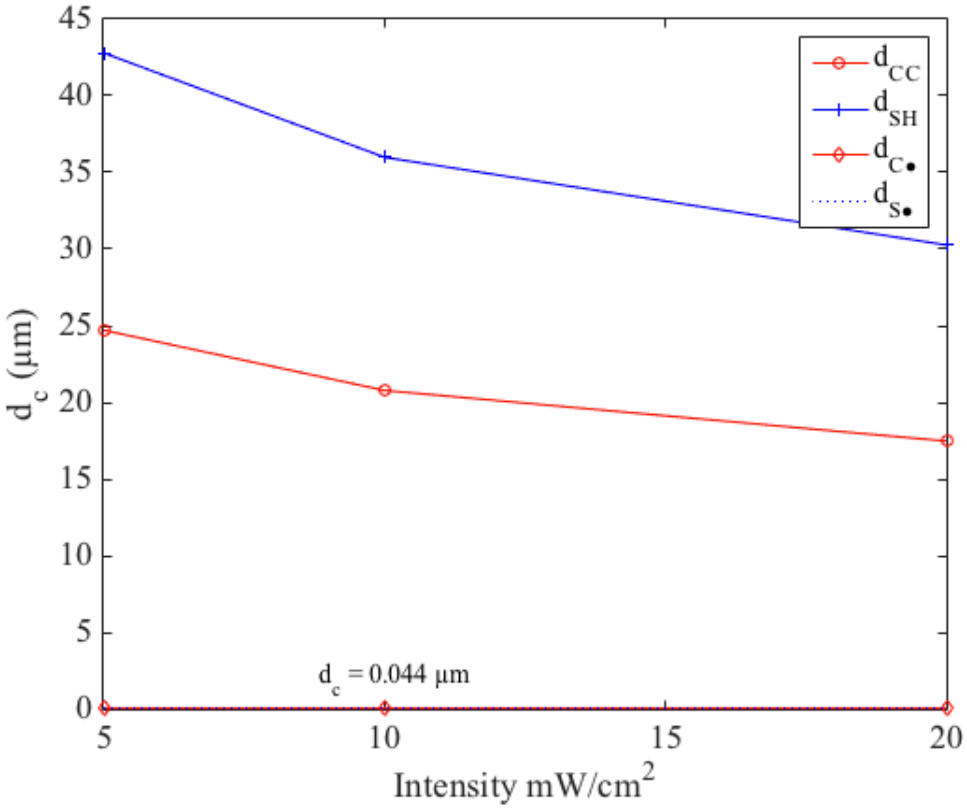


**Figure 3.3** Characteristic distance molecules can diffuse before reacting plotted as a function of incident intensity for species diffusing into the photopattern, [CC] and [SH], and out of the photopattern, $[C\cdot]_s$ and $[S\cdot]_s$. Because the characteristic distances for the radical species, $[C\cdot]_s$ and $[S\cdot]_s$, are significantly shorter than that of unreacted species, [CC] and [SH], the characteristic distance is labeled.

*3.3.4 Reaction-induced differential swelling*

An additional feature of hydrogels that affects photopattern fidelity is reaction-induced differential swelling. This differential swelling is related to the crosslinking density and therefore thiol concentration, which reduce the swelling ratio of the patterned region with respect to the initial hydrogel network. Illuminated regions thus expel water and de-swell, which contracts the hydrogel matrix and stretches the bonds at the edges of the pattern. If this process occurs during illumination, the edges of the pattern inside the illuminated region will experience less total conversion as gel is pulled into the light via elastic deformation. Using the technique introduced in Chapter 3 to determine the volumetric swelling ratio (Q), the swelling ratios between the initial precursor-swollen hydrogel network ($Q_0$) (w.r.t. the un-swollen initial network) versus the

photopatterned network ($Q_P$) (w.r.t. the swollen initial network) are found and used to determine the linear deformation ratio.

Taking the cube-root of each swelling ratio yields the linear deformation ($\lambda$) within the precursor solution, where $\lambda_0$ and $\lambda_P$ for the initial swollen hydrogel and the photopatterned network, respectively. The ratio of these two linear deformations yield the percent shrinkage that should be expected at the edges of the photopattern where, $\lambda_P/\lambda_0 =$ predicted linear deformation. This model assumes that the photopatterned feature in question is sufficiently isolated from any other photopatterns that could affect this shrinkage. The linear deformation ratio quantifies how much the pattern should deform at the edges with respect to the total photopattern dimensions assuming uniform crosslinking within the photopattern (*e.g.*, the edge of a photopattern width of 1 mm would move by ½ the expected total deformation because only ½ the photopattern width contributes to the shrinkage away from the pattern edge).

### 3.4 Conclusion

The ability to print high-fidelity cytocompatible hydrogel materials using SLA will enable tissue engineers to fabricate structures with 3D user-defined mechanical and chemical properties, which is required to fully recapitulate complex biological tissues and organs. Developed here is a model to predict the fidelity of photopatterned hydrogel structures given the high diffusivity, reduced reactivity of high-solvent precursor solutions and is represented by the characteristic distances of diffusing species into and out of the photopatterning region. Furthermore, a model to predict differential swelling as a function of bulk hydrogel properties and photopattern dimensions, which could, in theory, be compensated for by modifying the equilibrium swelling conditions of the hydrogel precursor solution of interest. Chapter 5 compares the predictive models presented here to experimental data obtained from hydrogels photopatterned using the custom SLA printer discussed in Chapter 2.

### 3.5 References


1. Kloxin, A. M., Kasko, A. M., Salinas, C. N. & Anseth, K. S. Photodegradable hydrogels for dynamic tuning of physical and chemical properties. *Science* **324,** 59–63 (2009).
2. Fairbanks, B. D. *et al.* A versatile synthetic extracellular matrix mimic via thiol-norbornene photopolymerization. *Adv. Mater.* **21,** 5005–5010 (2009).

3. wei Lv, H. *et al.* Biomaterial stiffness determines stem cell fate. *Life Sci.* (2017). doi:10.1016/j.lfs.2017.04.014
4. Park, J. H., Jang, J., Lee, J. S. & Cho, D. W. Three-Dimensional Printing of Tissue/Organ Analogues Containing Living Cells. *Ann. Biomed. Eng.* 1–15 (2016). doi:10.1007/s10439-016-1611-9
5. Hospodiuk, M., Dey, M., Sosnoski, D. & Ozbolat, I. T. The bioink: A comprehensive review on bioprintable materials. *Biotechnol. Adv.* **35,** 217–239 (2017).
6. Elomaa, L. *et al.* Three-dimensional fabrication of cell-laden biodegradable poly(ethylene glycol-co-depsipeptide) hydrogels by visible light stereolithography. *J. Mater. Chem. B* **3,** 8348–8358 (2015).
7. Chan, V., Zorlutuna, P., Jeong, J. H., Kong, H. & Bashir, R. Three-dimensional photopatterning of hydrogels using stereolithography for long-term cell encapsulation. *Lab Chip* **10,** 2062–2070 (2010).
8. Linnenberger, A. Live cell lithography and non-invasive mapping of neural networks. (University of Colorado Boulder, 2014).
9. Roberts, J. J. & Bryant, S. J. Comparison of photopolymerizable thiol-ene PEG and acrylate-based PEG hydrogels for cartilage development. *Biomaterials* **34,** 9969–9979 (2013).
10. Cramer, N. B., Reddy, S. K., O'Brien, A. K. & Bowman, C. N. Thiol - Ene Photopolymerization Mechanism and Rate Limiting Step Changes for Various Vinyl Functional Group Chemistries. *Macromolecules* **36,** 7964–7969 (2003).
11. Wade, R. J., Bassin, E. J., Gramlich, W. M. & Burdick, J. A. Nanofibrous hydrogels with spatially patterned biochemical signals to control cell behavior. *Adv. Mater.* **27,** 1356–1362 (2015).
12. Reddy, S. K., Cramer, N. B. & Bowman, C. N. Thiol−Vinyl Mechanisms. 1. Termination and Propagation Kinetics in Thiol−Ene Photopolymerizations. *Macromolecules* **39,** 3673–3680 (2006).
13. Kang, W., Bi, B., Zhuo, R. & Jiang, X. Photocrosslinked methacrylated carboxymethyl chitin hydrogels with tunable degradation and mechanical behavior. *Carbohydr. Polym.* **160,** 18–25 (2017).
14. Cramer, N. B., Reddy, S. K., O'Brien, A. K. & Bowman, C. N. Thiol−Ene

Photopolymerization Mechanism and Rate Limiting Step Changes for Various Vinyl Functional Group Chemistries. *Macromolecules* **36,** 7964–7969 (2003).

# Chapter 4- Control of Hydrogel Properties via Swelling and Photopolymerization

## 4.1 Executive Summary

This study investigates the range of mechanical properties a single precursor solution can produce by cyclically in-swelling fresh precursor solution followed by photo-exposing the swollen gel ("swelling + exposure" or SE cycle). By characterizing the range of mechanical properties in bulk hydrogel, this work can be extended and implemented into a 3D printing system to spatially photopattern mechanical properties using a single material, as shown in Chapter 5. I employ a cytocompatible photo-clickable poly(ethylene glycol) macromer solution to demonstrate this technique, which consists of PEG-dithiol and 8-arm PEG-norbornene. I chose three cytocompatible precursor solution formulations of 5, 10, and 20 wt% macromer concentration in phosphate buffered saline (PBS) to investigate, each of which underwent 10 SE cycles. The process was terminated at 10 cycles based on the observation that properties changed rapidly in the first several cycles and much more slowly by cycle 10. Comparing the gels that underwent zero SE cycles (single network gels) to those that underwent multiple SE cycles, I demonstrate that hydrogel mechanical properties can be increased by more than an order of magnitude using this technique, e.g., compressive moduli increase from 10s kPa to 100s kPa.

## 4.2 Introduction

Hydrogels are the subject of extensive research as tissue scaffolds due to their tunable properties including water content (50-97%), swellability (~5-15X), diffusivity (up to ~100 $\mu m^2/s$) and stiffness (1s to 1000s of kPa).[1–7] These materials mimic the extracellular matrix of a variety of human tissues, ranging from fat to cartilage.[8] Hydrogels can also be highly cytocompatible, with cell viability on the order of 95% after weeks of culture.[1] Cartilage repair and regeneration is particularly difficult as the native tissue possesses limited ability to heal. However, a cartilage replacement must bear the physiological loads on the order of ~1000s of N, while simultaneously providing a soft scaffold that is suitable for cells.[9–12] This dual requirement for spatially

controlled tough, high-modulus global behavior that is locally soft and resorbable is challenging to meet with a homogeneous material. A patterned, heterogeneous structure can address this requirement.[13]

Stereolithography offers a route to spatially pattern such structures. In all variants of stereolithography, an optical pattern representing a two-dimensional slice of a 3D design hardens a thin layer of resin.[14,15] As the fabrication is moved away from the light source by a motorized platform, a fresh layer of liquid resin is supplied by the bath surrounding the part. To incorporate a second printing material, the incomplete part must be removed from the bath, washed in a solvent, and placed into a bath of the second macromer resin. This process is slow and wasteful of material.[16] When printing with cell-laden precursor solutions, the solvent wash can lead to cell death.[16–18] Finally, the high diffusivity of hydrogels causes the subsequent macromer solutions to rapidly penetrate the existing solidified gel, making it difficult to pattern distinct features.

Previous research by DeForest et al.[19] and Marklein et al.[20] exploited this rapid diffusion of molecules into a previously polymerized hydrogel to spatially pattern different chemical cues that control stem cell differentiation, by in-diffusing functionalized macromer solutions and locally photopolymerizing. Similarly, Ducrot et al.[21] and Gong et al.[22,23] demonstrated modification of an existing polymer network by swelling the original matrix with a second precursor solution, which was then polymerized, forming a double network (DN) hydrogel. While these techniques demonstrated that macromer transport followed by photopolymerization can selectively modify properties of biologically relevant hydrogels, the use of multiple macromer formulations is inherently difficult for stereolithography, as described.

To overcome these challenges, transport of the original macromer solution into the printed gel can be exploited to obtain large variations in mechanical properties using only a single macromer solution, avoiding removal from the bath and solvent wash. Specifically, precursor solution of the same formulation is allowed to swell into an existing polymerized matrix and is selectively polymerized, locally modifying the hydrogel properties.[23] Exploiting the rapid transport inherent to hydrogels and using a single precursor solution to produce a mechanically diverse 3D structure enables the large range of mechanical properties required for cartilage replacement to be efficiently fabricated in a stereolithographic 3D printer.

This study investigates the range of mechanical properties a single precursor solution can produce by cyclically in-swelling fresh precursor solution followed by photo-exposing the swollen gel ("swelling + exposure" or SE cycle), as illustrated in **Figure 4.1**.[20–22] We employ a cytocompatible photo-clickable poly(ethylene glycol) macromer solution to demonstrate this technique, which consists of PEG-dithiol and 8-arm PEG-norbornene.[24–26] We chose three cytocompatible precursor solution formulations of 5, 10, and 20 wt% macromer concentration in phosphate buffered saline (PBS ) to investigate, each of which underwent 10 SE cycles.[12,24] The process was terminated at 10 cycles based on the observation that properties changed rapidly in the first several cycles and much more slowly by cycle 10. Comparing the gels that underwent zero SE cycles (single network gels) to those that underwent multiple SE cycles, we demonstrate that hydrogel mechanical properties can be increased by more than an order of magnitude using this technique, e.g., compressive moduli increase from 10s kPa to 100s kPa. By characterizing the range of mechanical properties in bulk hydrogel, this work can be extended and implemented into a 3D printing system to spatially photopattern mechanical properties using a single material, as shown herein.

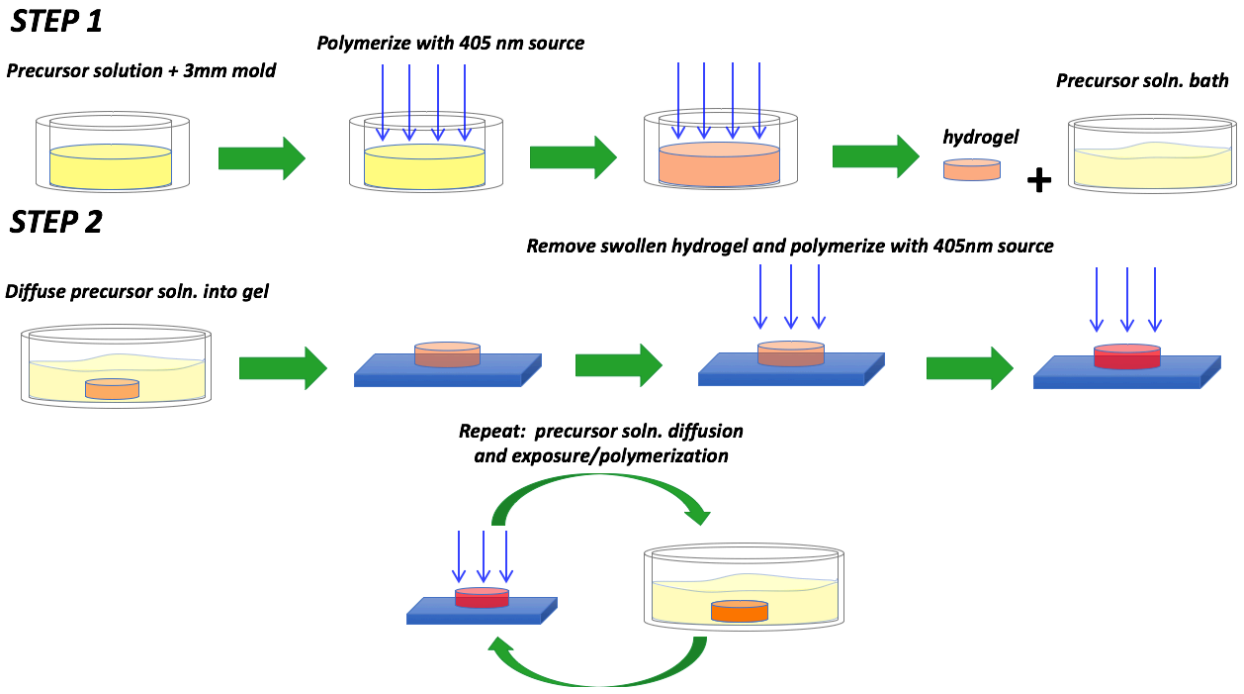


**Figure 4.1** (1) The initial precursor solution is placed into a cylindrical mold and photopolymerized into a hydrogel. (2) The hydrogel is then placed into a bath containing the same macromer and photoinitiator concentrations as were used to form the initial gel and swollen to equilibrium. (3) The swollen gel is removed and immediately polymerized using the same

exposure conditions as step 1. Steps 2-3 encompass a single DE cycle, which is repeated up to 10 times.

## 4.3 Experimental Procedure

### *4.3.1 Materials*

Poly(ethylene glycol) dithiol (PEG-dithiol (Sigma Aldrich, MW 1,000 Da), poly(ethylene glycol) thiol (tripentaerythritol) (JenKem USA, 8ARM-PEG-SH, MW 10,000 Da), and lithium phenyl-2,4,6-trimethylbenzoylphosphinate (LAP) (Colorado Photopolymer Solutions) were used as received. 5-norbornene-2-carboxylic acid (NB) (Sigma Aldrich) was conjugated to poly(ethylene glycol) amine (PEG-$NH_2$) (JenKem USA, 8arm PEG amine, HCl salt, MW 10,000 Da) at room temperature (RT) under an argon purge to produce poly(ethylene glycol) norbornene (PEG-NB). [12] This was done by dissolving PEG-$NH_2$ (10 g) in dimethylformamide (DMF) (15mL) and dichloromethane at 1:1 ratio to which the solution containing 4-molar excess NB (4.42g), 2 molar excess 2-(1H-7-Azabenzotriazol-1-yl)-1,1,3,3-tetramethyl uronium hexafluorophosphate methanaminium (HATU, AKSci) (9.12g), and 2 molar excess N,N-diisopropylethylamine (DIEA, Sigma) (6.2 g) was reacted with for 48 hours. The solution was precipitated in diethyl ether, dialyzed four times with di$H_2O$ over two days, and lyophilized. The resulting 8-arm PEG-NB product conjugation of 99% (percentage of NB conjugated PEG arms), referred to herein as PEG-NB. The degree of norbornene conjugation was determined by $^1$HNMR (Bruker AV-III 400) by comparing the area under the peak for the allylic hydrogen closest to the norbornene bridged cyclic hydrocarbon group (resonance from ~3.1 to 3.2 ppm) to the area under the peak for the methyl groups in the PEG backbone (resonance from ~3.4 to 3.85 ppm), see **Figure 4.2** for $^1$HNMR spectrum. Macromers were dissolved in phosphate-buffered saline (PBS) (OmniPur, Calbiochem).

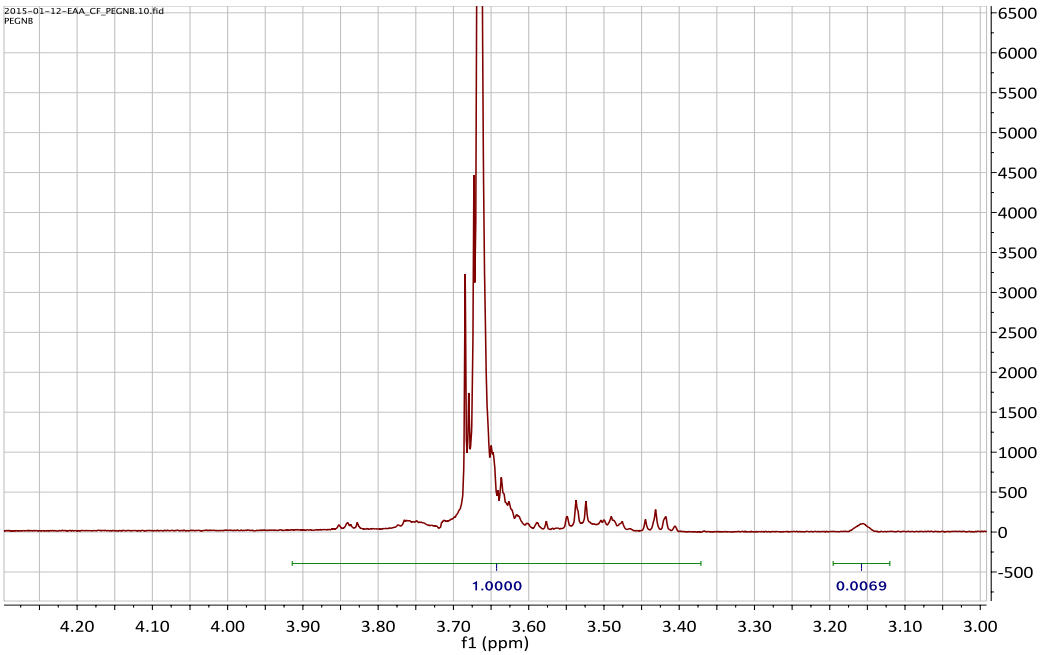


**Figure 4.2** Nuclear magnetic resonance spectrum of the conjugation product of norbornene (NB) to poly(ethylene glycol) amine (PEG), where (a) indicates the spectrum of the PEG backbone with resonance between ~3.4-3.85 ppm and (b) indicates the spectrum for the allylic proton closest to the NB R group with resonance between ~3.1-3.2 ppm. A 99% conjugation percentage was found using the ratio of the two peak areas combined with the molecular weight of the PEG and NB molecules.

### *4.3.2 Sample Preparation*

PEG-NB and PEG-dithiol (at 0.25:1, 0.5:1, 0.75:1, and 1:1 thiol:ene ratios) were combined with cytocompatible UV photoinitiator LAP[24] at 0.05 wt% in PBS at three precursor solution concentrations of 5, 10, and 20 wt% of total macromer. First PEG-NB was dissolved into PBS for 10 hrs., PEG-dithiol and LAP were then added immediately before use to minimize the formation of disulfide bridges within the solution. A volume of 20 µL precursor solution was then added to 3 mm diameter by 5 mm cylindrical molds and photopolymerized with a uniform intensity 405 nm illumination (OmniCure S1000) at RT for 6 minutes (13 mW/cm$^2$) to form a cylindrical hydrogel, with the diameter ~3 mm and height ~ 2 mm. Because the hydrogels are formed at a high solvent concentration and off stoichiometry, unreacted 'enes' and any unreacted thiols are free to react with new precursor solution, as shown in **Figure 4.3**.

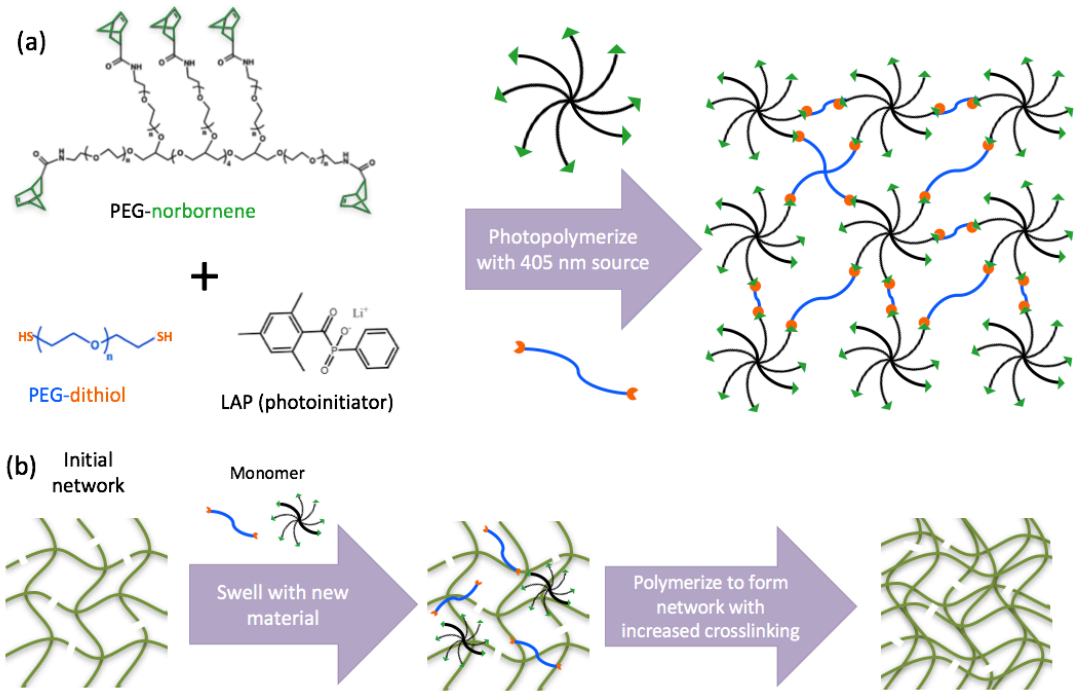


**Figure 4.3** (a) The chemical structure of the precursor solution components, where the green and orange regions indicate the functional groups norbornene and thiol, respectively. (b) An illustration of initial network formation showing remaining functional groups after polymerization. (c) A cartoon depicting the network transformation after a single SE cycle.

To modify the characteristics of the existing polymer network, the gel was then placed into a fresh bath of precursor solution containing the same concentrations of macromer and photoinitiator as used to form the original gel. The precursor solution bath volume was maintained at 15 times greater than the gel volume to prevent significant concentration dilution of the bath during swelling. Each hydrogel was swollen to approximate equilibrium at RT by leaving it in the bath for a time determined by a series of swelling experiments, as described below and in **Table 4.2**.

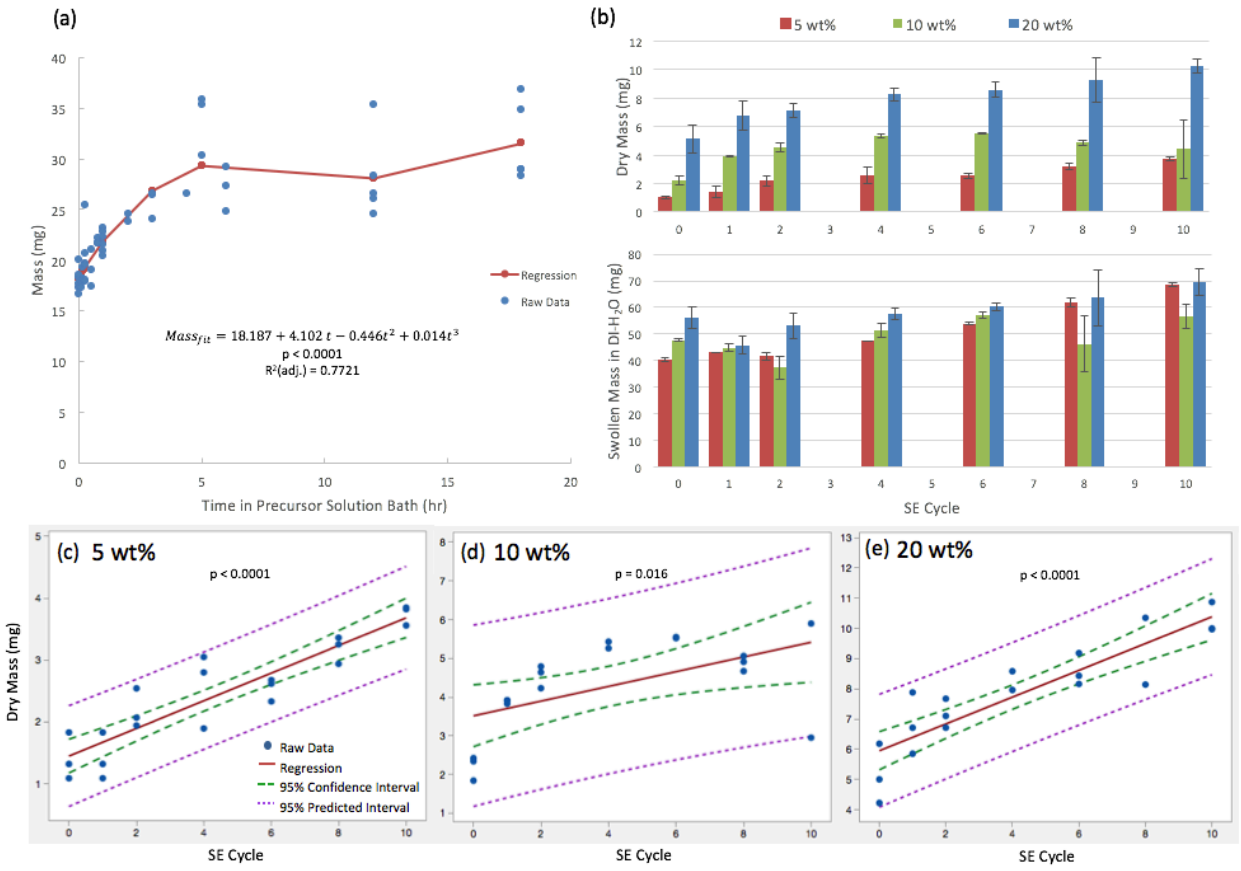


**Figure 4.4** (a) Swollen mass as a function of time in precursor solution bath and the polynomial regression analysis, shown as solid line in red ($p<0.0001$) (b) Bar graphs illustrating increased dry and swollen masses as a function of DE cycle with standard deviation indicated. (c-d) Regression fits with 95% confidence interval, demonstrating statistically significant increase in dry polymer mass as a function of DE cycle.

To ensure homogeneous concentration of the precursor solution bath throughout swelling, it was placed onto an orbital shaker at an oscillation speed of 90 rpm. The gel was then removed, gently dried (removing only liquid remnants on surface of gel), and immediately polymerized with a 405 nm exposure source. The above process was repeated 10 times, n=3-4 trials per cycle. Each gel was then placed into a bath of deionized (DI) water and swollen to equilibrium for 24 hours. DI water replaced the previously used PBS to remove the salts from the dried gel mass, and all swelling measurements were taken at this time.

### *4.3.3 Characterization*

#### 4.3.3.1 Mechanical Properties

Unconfined compression tests were performed using a Material Testing System (MTS) Insight 2 (MTS Systems Corporation. Two different capacity (5 N and 250 N) load cells were used to encompass the varying maximum loads produced by compressing each of the equilibrium swollen, 3 mm x 2 mm cylindrical gel samples (i.e., the 250 N load cell was required to test 10 wt% gels from SE cycles 4-10 and all 20 wt% samples). Stress-strain tests were all run to failure. The duration of each compression test was under 5 minutes, a sufficiently short time to neglect the effects of evaporation.

The compressive modulus (hereafter termed 'modulus') was found using engineering stress-strain curves taken for equilibrium-swollen hydrogels in DI water **(Figure 4.5**). Hydrogel toughness was determined by compressing each gel at a rate of 0.5 mm/min until failure (*i.e.,* the point at which the gel experienced fracture as indicated by a severe drop in stress) and then integrating the region under the stress-strain curve to obtain toughness prior to failure. The ultimate strength is the highest stress attained before failure. It should be noted that all stress and strain values presented herein are based on preloaded sample dimensions using infinitesimal strain assumptions.[27]

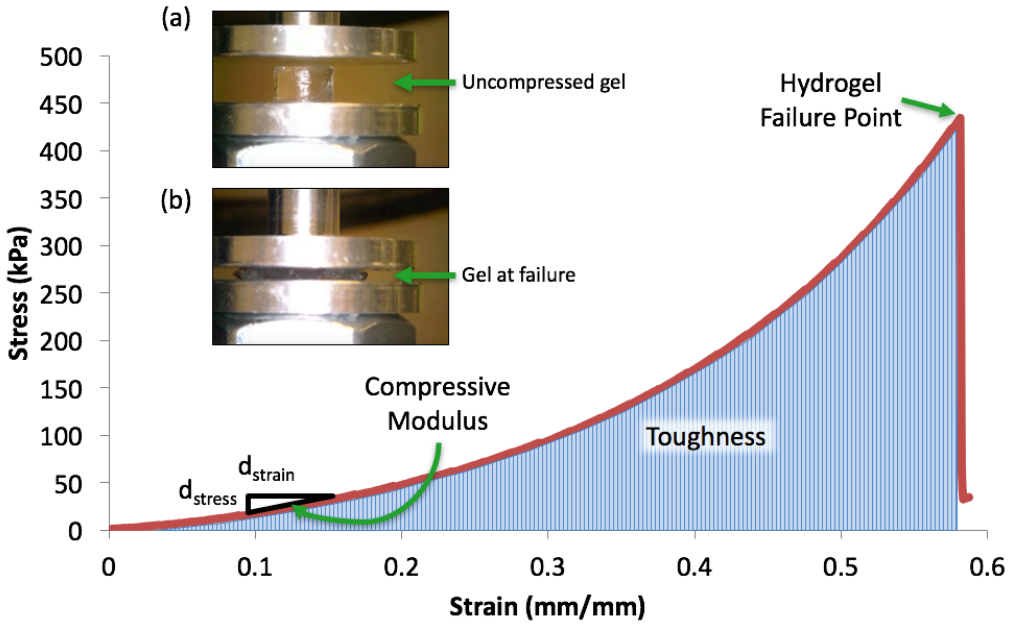


**Figure 4.5** Stress-strain curve illustrating the hydrogel behavior under compressive loading and subsequent failure where the slope of the curve at 15% strain was used to determine the engineering compressive modulus, and the shaded region indicates the toughness. (Inset) (a) and (b) show images of a single hydrogel sample before compression and at compressive failure known as ultimate compressive stress, respectively.

The hydrogel equilibrium volumetric swelling ratio, $Q$, was determined by

$$Q = 1 + {}^{\rho_p}/_{\rho_s}\left({}^{M_s}/_{M_d} - 1\right), \tag{4-1}$$

where $M_s$ is the equilibrium DI swollen mass of each gel, $M_d$ is the polymer mass after lyophilization, $\rho_p$ is the polymer density assumed to be 1.08 mg/mL, and $\rho_s$ is the density of water (1 g/mL).[25,27] From equilibrium volumetric swelling ratio, the polymer volume fraction is defined by[28]

$$\phi = Q^{-1}, \tag{4-2}$$

we estimated crosslink density, $\rho_x$ and the polymer-solvent interaction parameter, $\chi_{12}$ using a self-learning model described by Akalp et al.[29] This model uses the experimentally determined parameters of polymer volume fraction (*i.e.*, $\phi$) and the modulus of the fully swollen as inputs and solves for $\rho_x$ and $\chi_{12}$ by combining Flory-Rehner theory with theories of mixture and poroelasticity.[30–33] The model assumes isotropic swelling and uses a modified version of Flory-Rehner theory that neglects the contribution of chain ends. These assumptions are reasonable for unconstrained swelling conditions and have been shown to predict swelling and modulus of similar PEG hydrogels.[29]

The linear deformation of a hydrogel network, assuming isotropic swelling, is described by $Q^{1/3}$.[34] To understand the impact of in-swelling on the level of polymer chain stretching at each SE cycle, the ratio of linear deformation of the hydrogel at equilibrium ($Q_{n,f}^{1/3}$) to the linear deformation of hydrogel immediately after the gel is formed but before swelling ($Q_{n,i}^{1/3}$) was evaluated for cycle $n$. This ratio is defined in terms of $\phi$ by[28]

$$\lambda_n = \left(\frac{\phi_{n,i}}{\phi_{n,f}}\right)^{1/3}. \tag{4-3}$$

*4.3.4 Statistical Analysis*

Polynomial regression, a special case of multiple linear regression, was performed for each mechanical property response (modulus, toughness, swelling ratio) in models including SE cycle, $SE^2$, and $SE^3$. For each dependent variable, the models were constructed and compared for each combination of linear, quadratic, and cubic orders of SE. Model selection favored overall model significance ($p < 0.05$), and high $R^2$(adjusted) (**Table 4.1**). For several responses, log

transformation of the dependent variable was necessary to satisfy model assumptions of normally distributed residuals and unstructured residuals versus model fits. Simple linear regression was used to evaluate the relationship between toughness and modulus where model assumptions were satisfied. Two-factor ANOVA considered the effect of hydrogel composition (5, 10, 20 wt%) and bath composition (with or without photoinitiator) on mechanical properties. For all analyses, alpha was set *a priori* at 0.05. All statistics were performed with Minitab (v.17).

| | Best-fit Polynomial Regression Analysis | | |
|---|---|---|---|
| | **Fit Equation** | **p-value** | **$R^2$(adj.)** |
| **5 wt%** | | | |
| Compressive Modulus ($E$) | $E_{fit} = -2.8 + 36.0\,SE - 6.3\,SE^2 + 0.3\,SE^3$ | <0.0001 | 0.768 |
| Toughness ($T$) | $\ln(T)_{fit} = 1.11 + 1.88\,SE - 0.38\,SE^2 + 0.02\,SE^3$ | 0.0092 | 0.670 |
| Volume Swelling Ratio ($Q$) | $Q_{fit} = 40.6 - 13.3\,SE + 2.5\,SE^2 - 0.1\,SE^3$ | <0.0001 | 0.811 |
| Crosslink Density ($\rho_x$) | $\rho_{xfit} = -0.000526 + 0.0101\,SE - 0.00172\,SE^2 + 0.00009\,SE^3$ | 0.0198 | 0.896 |
| Linear Deformation ($\lambda$) | $\lambda_{fit} = 1.289 - 0.015\,SE - 0.0016\,SE^2 + 0.0002\,SE^3$ | <0.0001 | 0.864 |
| Linear Deformation Ratio ($\lambda_n$) | $\lambda_{nfit} = 3.435 - 0.443\,SE - 0.082\,SE^2 + 0.005\,SE^3$ | <0.0001 | 0.790 |
| **10 wt%** | | | |
| Compressive Modulus ($E$) | $\ln(E)_{fit} = 3.00 + 1.22\,SE - 0.21\,SE^2 + 0.01\,SE^3$ | <0.0001 | 0.931 |
| Toughness ($T$) | $T_{fit} = 9.4 + 38.1\,SE - 8.0\,SE^2 + 0.5\,SE^3$ | <0.0001 | 0.759 |
| Volume Swelling Ratio ($Q$) | $Q_{fit} = 21.2 - 8.4\,SE + 1.5\,SE^2 - 0.1\,SE^3$ | 0.0006 | 0.636 |
| Crosslink Density ($\rho_x$) | $\rho_{xfit} = 0.00436 + 0.0148\,SE - 0.00208\,SE^2 + 0.00009\,SE^3$ | 0.0018 | 0.980 |
| Linear Deformation ($\lambda$) | $\lambda_{fit} = 2.868 - 0.712\,SE + 0.129\,SE^2 + 0.006\,SE^3$ | 0.042 | 0.300 |
| Linear Deformation Ratio ($\lambda_n$) | $\lambda_{nfit} = 1.351 - 0.072\,SE + 0.008\,SE^2 - 0.006\,SE^3$ | <0.0001 | 0.864 |
| **20 wt%** | | | |
| Compressive Modulus ($E$) | $E_{fit} = 107 + 152\,SE - 30\,SE^2 + 2\,SE^3$ | <0.0001 | 0.695 |
| Toughness ($T$) | $\ln(T)_{fit} = 3.41 + 0.88\,SE - 0.17\,SE^2 + 0.01\,SE^3$ | <0.0001 | 0.695 |
| Volume Swelling Ratio ($Q$) | $Q_{fit} = 10.9 - 2.79\,SE + 0.56\,SE^2 - 0.03\,SE^3$ | 0.0011 | 0.628 |
| Crosslink Density ($\rho_x$) | $\rho_{xfit} = 0.0242 + 0.0277\,SE - 0.0051\,SE^2 + 0.0003\,SE^3$ | 0.0302 | 0.862 |
| Linear Deformation ($\lambda$) | $\lambda_{fit} = 2.207 - 0.209\,SE + 0.042\,SE^2 - 0.002\,SE^3$ | 0.0018 | 0.600 |
| Linear Deformation Ratio ($\lambda_n$) | $\lambda_{nfit} = 1.408 - 0.081\,SE - 0.0134\,SE^2 - 0.0007\,SE^3$ | 0.0167 | 0.425 |

**Table 4.1** Polynomial regression analysis for all initial precursor formulations and hydrogel properties as functions of DE cycle are reported here along with their respective p and $R^2$(adjusted) values. For all models, we compared with linear and quadratic terms only models and for each response variable, a linear-quadratic-cubic model was most appropriate.

## 4.4 Results and Discussion

### *4.4.1 Preparation of PEG hydrogels*

To enable new precursor solution to react with the existing network, an off-stoichiometric ratio of thiol to 'ene' was used to ensure 'ene' groups remained unreacted after the initial network polymerization. We varied the thiol to 'ene' ratios from 0.25:1 to 1:1 at increments of 0.25 and characterized their mechanical and swelling properties and crosslink density, as shown in **Figure 4.6.** We chose the 0.5:1 ratio because it exhibited structural stability while leaving at least half of the initial 'ene' groups unreacted after the initial polymerization.

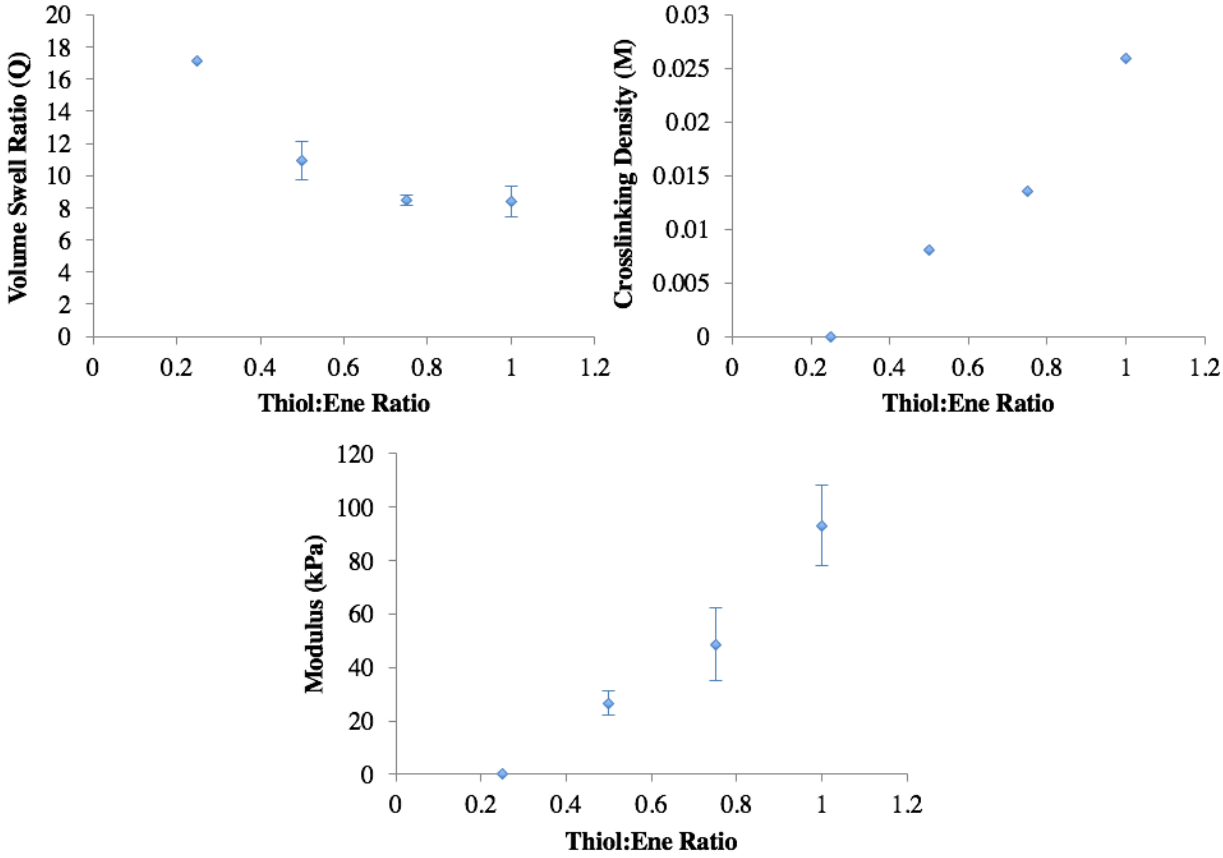


**Figure 4.6** The macroscopic properties of photo-clickable PEG hydrogels that were formed by varying the thiol:norbornene ratio from 0.25:1 to 1:1 using a precursor solution of 10 wt% macromer and 0.05 wt% LAP. The macroscopic properties are volumetric swelling ratio, *Q,* modulus, and crosslinking density, where n=3-4 and the vertical error bars (blue) indicate the standard deviation of a given sample set.

As a control experiment to verify that mechanical properties did not change in a single network gel by simply providing additional photoinitiator, a solution of 0.05 wt% LAP in PBS

was swelled into the initial single network hydrogels and exposed. As shown **Table 4.2,** no significant change in hydrogel properties was observed. This confirms that any change in mechanical properties, as a function of SE cycle, are the result of polymerization of new macromer.

To ensure that the length of time in the precursor solution bath was sufficiently long to allow each gel to approach equilibrium, gels of each formulation were placed into a bath precursor solution and incrementally removed to observe swollen mass as a function of time in the bath. Soak times of 6, 6, and 12 hours for the 5, 10, and 20 wt% gels, respectively, were determined for each SE cycle when the swollen mass had leveled off and no continued mass gain observed, which occurred after 5 hours of submersion for each formulation (**Figure 4.4a)**

To confirm experimentally that new macromers were transported into the hydrogel at each SE cycle, the dry polymer mass was obtained after each cycle, but before swelling, following lyophilization. For all formulations, the dry mass increased with SE cycle, demonstrating the in-swelling of new precursor solution into the gels (**Figure 4.4b-d**). We note that for the 5 wt% 0.5:1 hydrogels, the PBS salts were not diffused out from the hydrogel and contributed to and enhanced initial dry mass observed. To correct for this, the mass associated with the PBS salts that remain after lyophilization was determined and then subtracted from the dry mass.

The gels were designed with an off-stoichiometric ratio, leaving approximately 50% of the norbornene functional groups remaining after polymerization. However, non-idealities can leave behind unreacted thiols as well as norbornenes. To determine whether the PEG-NB macromer reacts significantly with free thiols, and thus contributes to the initial network, swelling of solely PEG-NB and photoinitiator in PBS into the single network hydrogel followed by light exposure was investigated.

| Precursor Solution Concentration | Bath with photoinitiator | Bath without photoinitiator | Compressive Modulus (kPa) | Volume Swelling Ratio (Q) |
|---|---|---|---|---|
| 5 wt% | X | | 6.92 ± 0.11 | 19.39 ± 2.02 |
| | | X | 6.65 ± 0.38 | 20.46 ± 0.99 |
| 10 wt% | X | | 18.79 ± 1.82 | 14.5 ± 3.4 |
| | | X | 18.09 ± 2.40 | 15.59 ± 1.59 |
| 20 wt% | X | | 50.63 ± 3.14 | 12.07 ± 0.40 |
| | | X | 49.76 ± 1.25 | 11.55 ± 1.24 |

**Table 4.2** Mechanical properties are not influence by the presence of photoinitiator. In a two-way ANOVA the main effect of wt% was significant ($p < 0.0001$). However, there was no significant main effect of photoinitiator status, and no significant interaction between wt% and photoinitiator status.

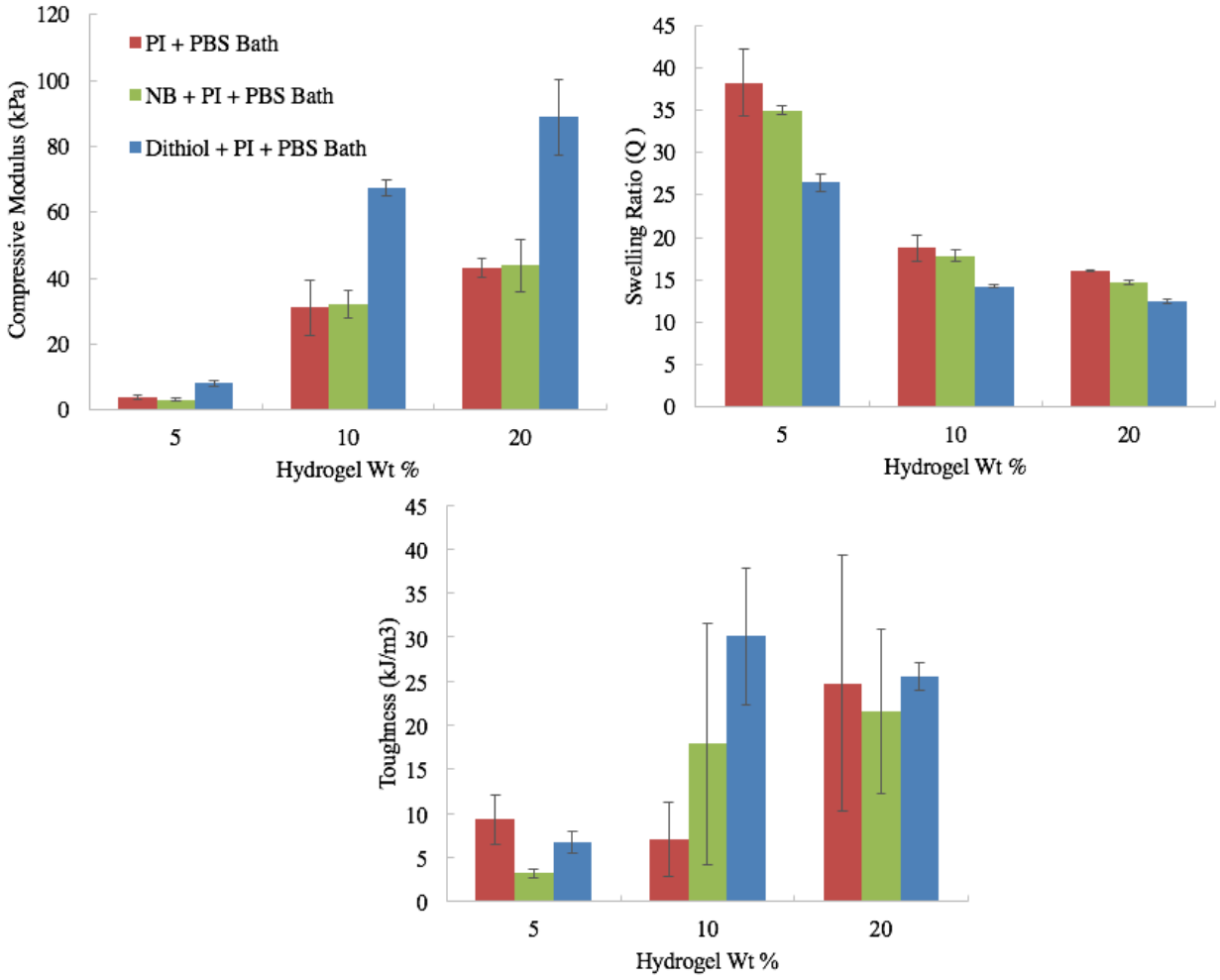

**Figure 4.7** Mechanical properties of hydrogels after a single swelling and exposure cycle using precursor solution containing solely (red) photoinitiator and PBS; (green) PEG-NB, photoinitiator, and PBS; or (blue) PEG-dithiol, photoinitiator. The compressive modulus was unaffected by the presence of solely PEG-NB in the solution, while it doubled when the PEG-dithiol solution was in-swelled and polymerized ($p<0.0001$). For both PEG-NB and PEG-dithiol solution, the swelling ratio decreased with respect to the photoinitiator solution control ($p<0.05$). Hydrogel toughness was not uniformly affected by the presence of either solely PEG-NB or PEG-dithiol across the three formulations ($p>0.05$).

No significant changes were observed in the modulus when hydrogels of 5, 10, and 20 wt% macromer with 0.5:1 thiol to ene ratios were prepared and swollen with fresh precursor solution of 0.05 wt% LAP in PBS with solely the PEG-NB macromer. This observation suggests that the concentration of free thiols in the initial network is low. However, diffusion of the PEG-NB macromer will be more limited due to its size and thus its concentration may be low.[35] Consequently, any reactions to the initial network may not, on its own, contribute significantly to the macroscopic properties. However, swelling the hydrogels with PEG-dithiol and photoinitiator in PBS led to increases in the compressive modulus by a factor of two (**Figure 4.7).** It is important to note that each gel was submerged in their respective precursor solution until equilibrium swelling was reached.

The necessity for an off-stoichiometric ratio of 'enes' to thiols was first probed by using the 5 wt% precursor solution, but with a 1:1 stoichiometric ratio between functional groups. This test was subject to 6 SE cycles as previously described.

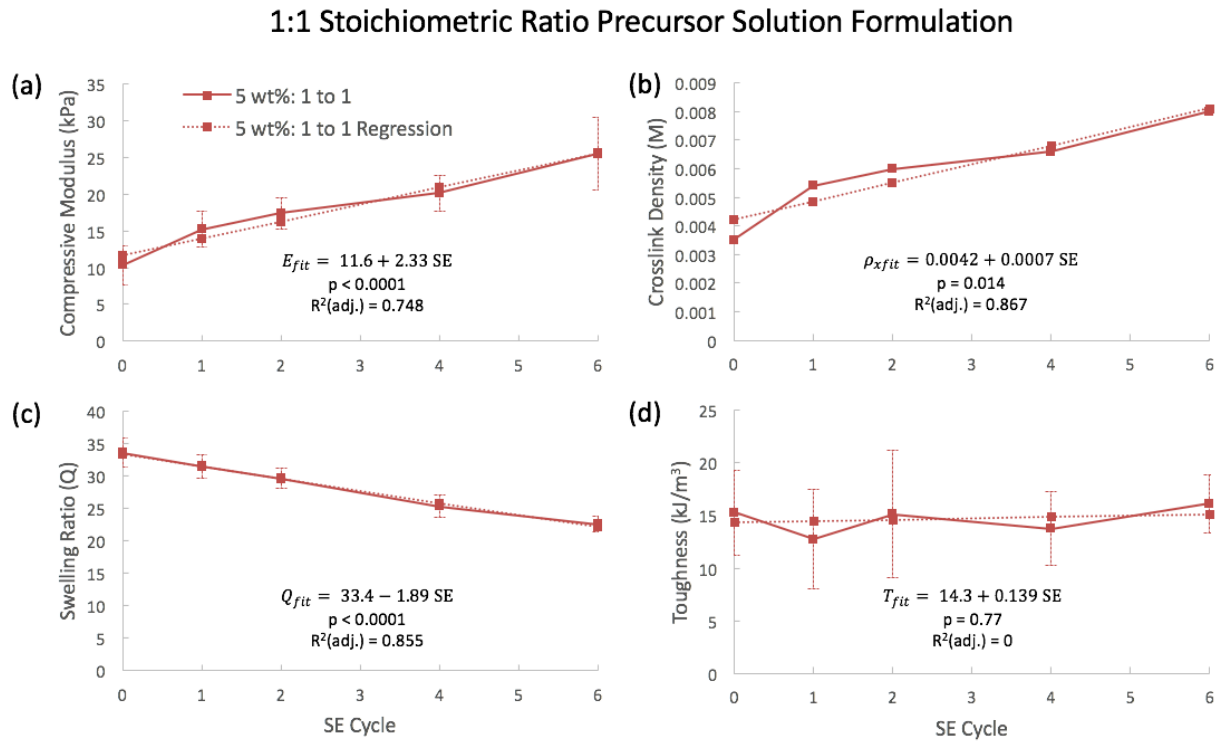


**Figure 4.8** (a) Changing thiol to 'ene' ratio from 0.5:1 to 1:1, modulus and (b) crosslink density linearly increase for all SE cycles ($p < 0.0001$ and $p = 0.014$, respectively). (c) The swelling ratio conversely decreased linearly for all SE cycles. (d) No significant relationship between toughness and SE cycle was visible after repeating 6 SE cycles ($p = 0.77$). The solid lines represent experimental data while the dotted represents the best-fit regression model.

A positive, linear relationship between modulus and SE cycle as well as crosslink density and SE cycle was found ($p<0.0001$ and $p = 0.014$, respectively), while the swelling ratio to SE cycle exhibited a negative, linear relationship ($p<0.0001$) (**Figure 4.8a-c**). The increase in modulus and decrease in swelling observed here is attributed to the presence unreacted thiol and ene functional groups that result from inefficiencies in crosslinking due to the high solvent concentration. The change in hydrogel properties was modest and even with multiple cycles, no relationship between toughness and SE cycle was found ($p=0.77$) (**Figure 4.8d**). This result corresponds with trends in elastic modulus data from the literature where the introduction of more precursor solution and subsequent polymerization to an already formed network with no accessible reactive groups, negligibly contributes to increased stiffness.[20,35] Based on these results, an off-stoichiometric ratio precursor solution was selected for subsequent experiments to investigate changes in macroscopic properties with SE cycle.

### *4.4.2 Characterization of enhanced PEG hydrogels*

This study demonstrates that repeated precursor in-swelling and exposure cycles affect both the modulus and the toughness of PEG hydrogels. We observed an order of magnitude increase in the modulus after 2-4 cycles for all precursor solution formulations (**Figure 4.9**). We hypothesize that during these cycles, the remaining 'enes' in the first network further react creating a more densely crosslinked network, evident by the increase in modulus. Because we observed greater increase in modulus after a single SE cycle than when solely swollen with a PEG-dithiol solution (**Figure 4.7**), the presence of PEG-norbornene in the in-swollen precursor solution contributes to the observed increased modulus. With each cycle, 'enes' and thiols are consumed, but new pendant free 'enes' and thiols are introduced leading to further increases in the crosslink density and subsequent modulus. However, beyond approximately 3 SE cycles, the modulus reached a plateau.

Concomitant with the increased modulus, we observed an increase in toughness of the hydrogels as they underwent up to ~2 SE cycles. The failure point was noted by a sharp decrease in the stress-strain curve corresponding to irreversible, inelastic damage with visibly fractured gels. The gel toughness increased for all formulations, for example by a factor of 4 for the 20 wt%. For the responses of modulus and toughness, models with quadratic and cubic terms of SE achieved the best fit. These models confirm the presence of a maxima (2-4 cycles), after which mechanical properties decreased with additional cycles.

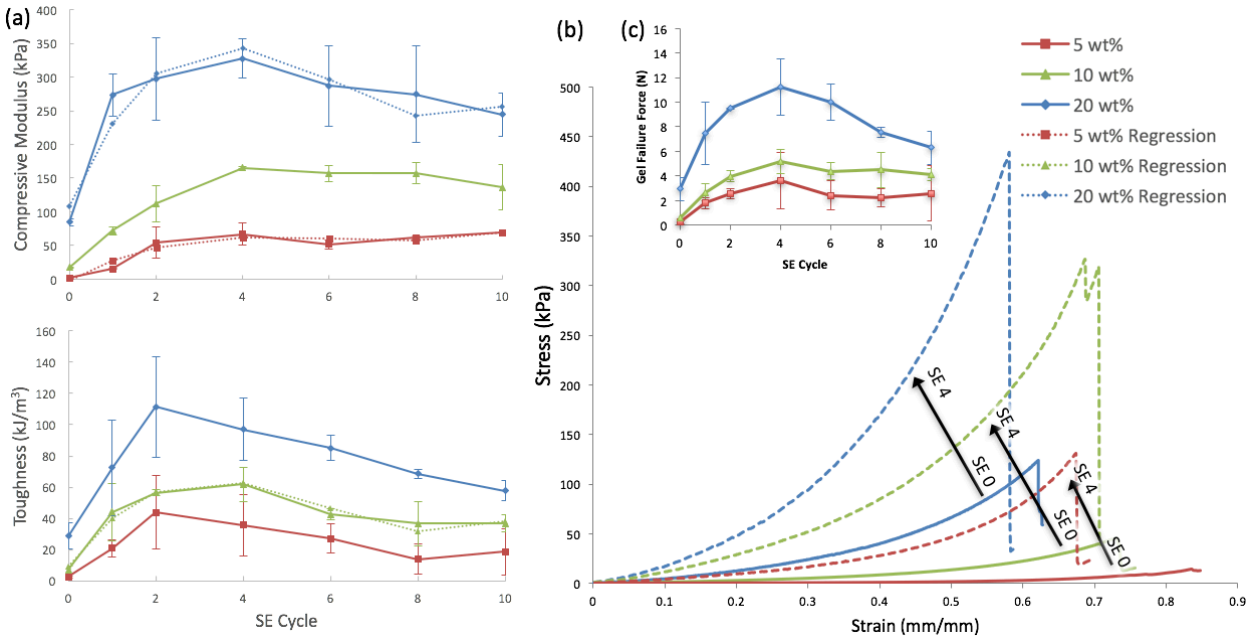


**Figure 4.9** (a) For all precursor solution formulations (5 (red), 10 (green), and 20 (blue) macromer wt%), the modulus and toughness increases until a plateau or decrease is reached at 2-4 SE cycles, Polynomial regression confirms that mechanical property data are best fit with a model including SE, $SE^2$, and $SE^3$. The shape of the most appropriate model confirms the presence of maxima in mechanical properties between 2-4 SE. For the full regression fits, p-values, and $R^2$ values see **Table 4.1**. (b) Shows the stress-strain curves until failure for each PS formulation at cycles 0 (solid line) and 4 (dashed line), where (c, inset) displays the ultimate strength as a function of SE cycle. All data are presented as mean with standard deviation as error bars for n=3-4.

For each precursor solution formulation, the equilibrium volumetric swelling ratio, $Q$, (**Figure 4.10a**) decreased as a function of SE cycle and reached a plateau after 3-4 SE cycles. As shown in **Figure 4.10b**, the crosslink density also follows this trend, which increased as a function of SE cycle until approximately 2-4 SE cycles, where the crosslink density reached a plateau (5 and 10 wt% gels) or decreased (20 wt% gels). Two hypotheses for the plateaus observed in the modulus, $Q$, and crosslink density are proposed. First, the macromers were not given adequate time to be transported into the gel once the gel had undergone multiple SE cycles. However, long times (~6-12 hours) were employed and the dry and swollen polymer masses (**Figure 4.4b**) increased with each SE cycle, suggesting that transport was not limited.

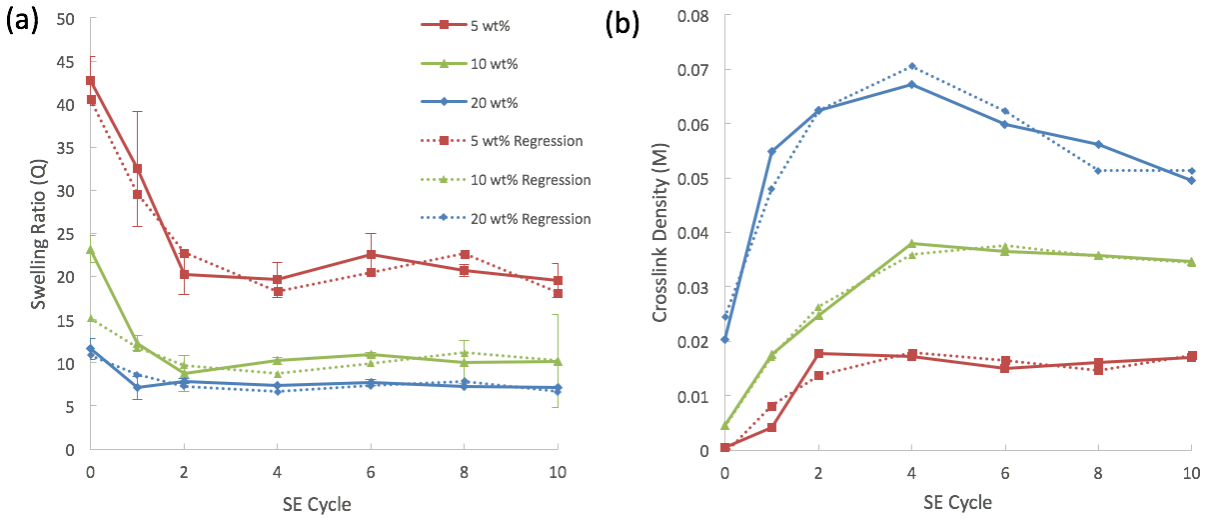


**Figure 4.10** (a) For all precursor solution formulations, a sharp decrease in the equilibrium volume swelling ratio, where Q was normalized to the dry mass of the hydrogels that underwent 0 SE cycles to account for sample variation. (b) The crosslink density experienced a similar trend to the mechanical properties, increasing until 2-4 cycles and then reaching a plateau. Polynomial regression analyses of Q versus linear and higher-order expressions of SE reveal that the best model fit is achieved with inclusion of SE, $SE^2$, and $SE^3$ terms. The best fitting model shows a maximum in Q between 2-4 SE cycles with $p < 0.05$ for all sample sets (**Table 4.1**). All data are presented as mean with standard deviation as error bars for n=3-4 except crosslink density, which was determined using all technical repeats (n=3-4) per condition in a self-learning algorithm.

Alternately, a complex, multi-network system may be forming. In support of this hypothesis, the dry polymer and swollen masses continued to increase beyond cycles 3-4 even though there were no longer any appreciable changes in mechanical or swelling properties. These data confirm that macromer is still being transported into the hydrogel and subsequently reacting and thus point to the formation of interpenetrating networks.

It is interesting, though, that the behavior the hydrogels formed herein differ substantially from typical double networks, which utilize two distinctly different materials, that exhibit an increase in toughness with the addition of the second material, while modulus remains approximately constant.[21–23,35]A linear regression analysis of toughness to modulus shows a positive correlation ($p < 0.0001$, $R^2$(adj.) = 0 .676), indicating that increase in modulus corresponds with increase in toughness in hydrogels fabricated via multiple SE cycles (**Figure 4.11**). This finding is consistent with single network hydrogels where increasing crosslinking increases both modulus and toughness. These data thus suggest that in the initial SE cycles, the

degree of crosslinking in the initial network increases leading to the combined increased in modulus and toughness. However, the plateau in properties at SE cycles of ~2-4 suggest that the bonds in this initial network dominates the mechanical properties at later SE (*i.e.*, > ~2-4) cycles.

To further understand how the network changes with increasing SE cycle, we calculated the linear deformation, $\lambda$, which is a measure of polymer chain stretching within the hydrogel relative to its dry state (**Figure 4.12a**). As expected, the polymer chains in the initial network (*i.e.*, SE=0) are more stretched in the 5 wt% (*i.e.,* low crosslinked) formulation compared to the more tightly crosslinked 10 and 20 wt% formulations.

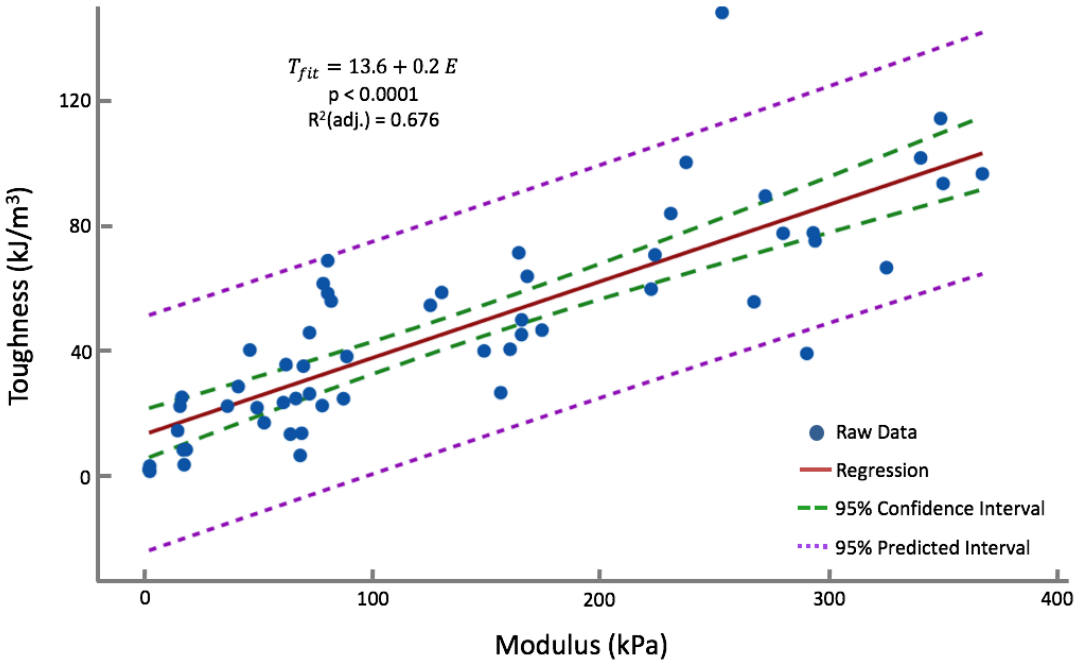


**Figure 4.11** Linear regression analysis (red solid line) confirming the positive relationship between increased modulus (E) and toughness (T) of SE cycle fabricated hydrogels with $p < 0.0001$ and $R^2$(adjusted) = 0.6759. The 95% Confidence (green dashed line) and Predicted (purple dotted line) Intervals are also plotted to highlight the model-to-data fit.

With increasing SE cycles up to ~SE 2, additional crosslinks are introduced into the initial network and overall the polymer chains do not stretch to the same extent as in the previous SE cycle. It should be noted that with each SE cycle, a distribution of polymer chains exists in different stretched states; however, $\lambda$ represents the average of all chains. At SE>~2, the linear deformation no longer changes with increasing SE cycle for each formulation.

Interestingly, however, the percent polymer mass continues to increase (*e.g.,* by 70% from SE2 to SE10 for the 5wt% formulation). Our data indicate that additional crosslinks are being introduced into the initial network (b/w SE2 and ~SE 4) as evidence by an increase in modulus and that an interpenetrating network(s) is like forming in subsequent SE cycles as indicated by the increased weight gain. Since $\lambda$ represents an average of chain stretching, it is reasonable to postulate that the chains in the initial network continue to be stretched with each SE cycle, but the new polymer chains that are introduced are less stretched. This statement is supported by data in **Figure 4.12b**, which describes the level of polymer stretching at equilibrium relative to the prepared state (*i.e.,* before swelling to equilibrium) for each SE cycle.

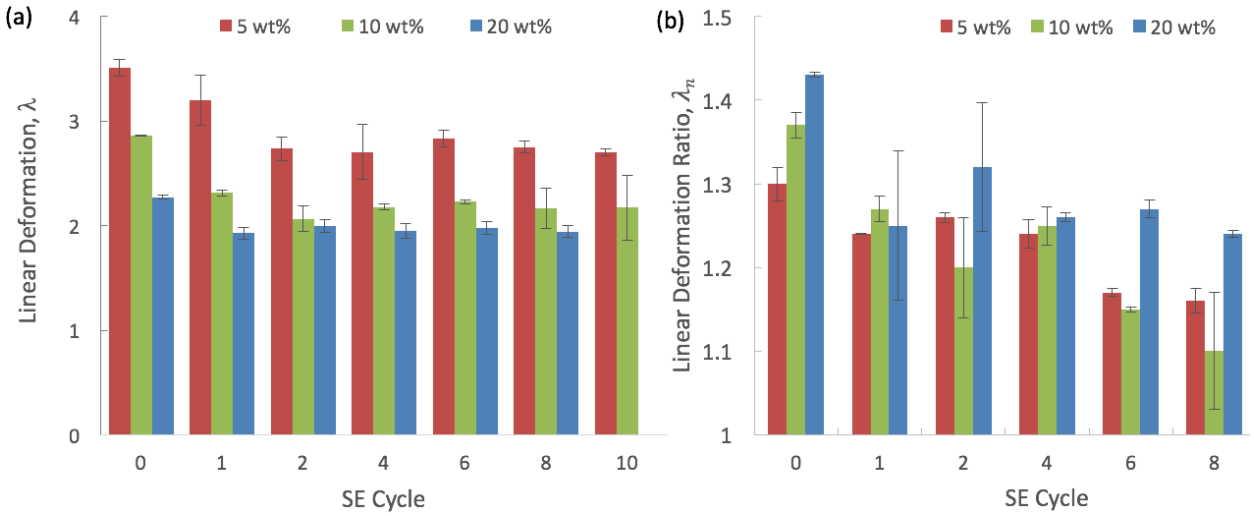


**Figure 4.12** (a) Linear deformation decreased a function of SE cycle, ($p<0.02$ for all formulations). (b) The linear deformation ratio comparing the linear deformation of the swollen network to that of the network immediately following polymerization also significantly decreases as a function of cycle ($p<0.0001$ for 5 and 20 wt% gels).

Notably for the 5 and 10 wt% formulations, this $\lambda_n$ ratio decreases with increasing SE through SE 10. This further supports that the new polymers introduced are in a much-reduced stretched state. For $\lambda$ to stay the same, the chains in the initial network, must then become increasingly stretched.

Collectively, the mechanical and swelling behaviour of PEG hydrogels formed via multiple SE cycles are largely dominated by the initial network. With the presence of free reactive groups after hydrogel formation, the initial network continues to grow with subsequent cycles. This led to a higher modulus and subsequent higher toughness due to the presence of

more crosslinks. However, as the chains in the initial network become more stretched with subsequent cycles, they require less force to break and thus dissipate lower energy during failure.[21,36] Indeed, we observed a decrease in toughness with increasing SE cycles from ~2-4 to 10. While interpenetrating networks are likely present, our data suggest that they are at a sufficiently low crosslink density and thus unable to contribute to the mechanical properties and notably toughness. Additional studies, however, are required to experimentally verify the exact nature of the networks formed using this SE approach.

### 4.5 Conclusion

Using a single precursor solution, the modulus and toughness of PEG hydrogels was shown to increase by 5-10x by in-swelling and polymerizing new macromer into an existing polymer network. Our data point to the initial network that forms during the first few SE cycles as dominating the macroscopic behavior of the hydrogel. This approach offers an elegant solution to spatially patterning mechanical properties in a biocompatible hydrogel. Because substantial material property changes can be achieved after 2-4 SE cycles, the small length scales of 3D printing (10s of μm) enable fabrication of mechanically diverse structures. Though the hydrogels tested here were not designed to bear forces sustained by native articular cartilage tissue, we offer a method to substantially increase the modulus and toughness of biocompatible hydrogels for tissue engineering applications.

### 4.6 References


1. Bryant, S. J., Anseth, K. S., Lee, D. a. & Bader, D. L. Crosslinking density influences the morphology of chondrocytes photoencapsulated in PEG hydrogels during the application of compressive strain. *J. Orthop. Res.* **22,** 1143–1149 (2004).

2. Luo, Y. & Shoichet, M. S. A photolabile hydrogel for guided three-dimensional cell growth and migration. *Nat. Mater.* **3,** 249–53 (2004).

3. Engler, A. J., Sen, S., Sweeney, H. L. & Discher, D. E. Matrix Elasticity Directs Stem Cell Lineage Specification. *Cell* **126,** 677–689 (2006).

4. Farley, R., Halacheva, S., Bramhill, J. & Saunders, B. R. Using click chemsitry to dial up the modulus of doubly crosslinked microgels through mrecise control of microgel building block functionalisation. *Polym. Chem.* (2015). doi:10.1039/C4PY01753F

5. Chen, Q., Chen, H., Zhu, L. & Zheng, J. Fundamentals of double network hydrogels. *J. Mater. Chem. B* **3,** 3654–3676 (2015).

6. Peppas, N. A. Hydrogels and drug delivery. *Curr. Opin. Colloid Interface Sci.* **2,** 531–537 (1997).

7. Limem, S. & Calvert, P. Diffusion properties of inkjet printed ionic self-assembling polyelectrolyte hydrogels. *J. Mater. Chem. B* **3,** 4569–4576 (2015).

8. Langer, R. & Vacanti, J. P. Tissue engineering. *Science* **260,** 920–6 (1993).

9. Bergmann, G. *et al.* Hip contact forces and gait patterns from routine activities. *J. Biomech.* **34,** 859–871 (2001).

10. D 'lima, D. D., Fregly, B. J., Patil, S., Steklov, N. & Colwell, C. W. Knee joint forces: prediction, measurement, and significance. *Spec. Issue Artic. Proc IMechE Part H J Eng. Med.* **226,** 95–102 (2012).

11. Amer, L. D. & Bryant, S. J. The In Vitro and In Vivo Response to MMP-Sensitive Poly(Ethylene Glycol) Hydrogels. *Ann. Biomed. Eng.* (2016). doi:10.1007/s10439-016-1608-4

12. Roberts, J. J. & Bryant, S. J. Comparison of photopolymerizable thiol-ene PEG and acrylate-based PEG hydrogels for cartilage development. *Biomaterials* **34,** 9969–9979 (2013).

13. Allan, K. S., Pilliar, R. M., Wang, J., Grynpas, M. D. & Kandel, R. A. Formation of biphasic constructs containing cartilage with a calcified zone interface. *Tissue Eng.* **13,** 167–77 (2007).

14. Melchels, F. P. W., Feijen, J. & Grijpma, D. W. A review on stereolithography and its applications in biomedical engineering. *Biomaterials* **31,** 6121–30 (2010).

15. Urness, A. C., Moore, E. D., Kamysiak, K. K., Cole, M. C. & Mcleod, R. R. Liquid deposition photolithography for submicrometer resolution three-dimensional index structuring with large throughput. *Light Sci. Appl.* **212,** (2013).

16. Chan, V., Zorlutuna, P., Jeong, J. H., Kong, H. & Bashir, R. Three-dimensional photopatterning of hydrogels using stereolithography for long-term cell encapsulation. *Lab Chip* **10,** 2062–2070 (2010).

17. Guvendiren, M., Molde, J., Soares, R. M. D. & Kohn, J. Designing Biomaterials for 3D Printing. *ACS Biomater. Sci. Eng.* **2,** 1679–1693 (2016).

18. Bryant, S. J., Nuttelman, C. R. & Anseth, K. S. The effects of crosslinking density on cartilage formation in photocrosslinkable hydrogels. *Biomed. Sci. Instrum.* **35,** 309–14 (1999).

19. DeForest, C. A., Polizzotti, B. D. & Anseth, K. S. Sequential click reactions for synthesizing and patterning three-dimensional cell microenvironments. *Nat. Mater.* **8,** 659–664 (2009).

20. Marklein, R. A. & Burdick, J. A. Spatially controlled hydrogel mechanics to modulate stem cell interactions. *Soft Matter* **6,** 136–143 (2010).

21. Ducrot, E., Chen, Y., Bulters, M., Sijbesma, R. P. & Creton, C. Toughening elastomers with sacrificial bonds and watching them break. *Science* **344,** 186–9 (2014).

22. Gong, J. P., Katsuyama, Y., Kurokawa, T. & Osada, Y. Double-Network Hydrogels with Extremely High Mechanical Strength. *Adv. Mater.* **15,** 1155–1158 (2003).

23. Gong, J. P. Why are double network hydrogels so tough? *Soft Matter* **6,** 2583 (2010).

24. Fairbanks, B. D. *et al.* A Versatile Synthetic Extracellular Matrix Mimic via Thiol-Norbornene Photopolymerization. *Adv. Mater.* **21,** 5005–10 (2009).

25. Skaalure, S. C. & Engineering, B. Tuning Hydrogel Degradation for Cartilage Tissue Engineering by. (2014).

26. Gould, S. T., Darling, N. J. & Anseth, K. S. Small peptide functionalized thiol–ene hydrogels as culture substrates for understanding valvular interstitial cell activation and de novo tissue deposition. *Acta Biomater.* **8,** 3201–3209 (2012).

27. Fung, Y. C. & Tong, P. *Classical and Computational Solid Mechanics*. **1,** (WORLD SCIENTIFIC, 2001).

28. Rubinstein, M. & Colby, R. H. *Polymer physics*. (Oxford University Press, 2003).

29. Akalp, U. *et al.* Determination of the Polymer-Solvent Interaction Parameter for PEG Hydrogels in Water: Application of a Self Learning Algorithm. *Polymer (Guildf).* **66,** 135–147 (2015).

30. Flory, P. J. *Principles of polymer chemistry.* (Cornell University Press, 1953).

31. Flory, P. J. & Erman, B. Theory of elasticity of polymer networks. 3. *Macromolecules* **15,** 800–806 (1982).

32. Holmes, M. H. & Mow, V. C. The nonlinear characteristics of soft gels and hydrated connective tissues in ultrafiltration. *J. Biomech.* **23,** 1145–1156 (1990).

33. Kwan, M. K., Lai, W. M. & Mow, V. C. A finite deformation theory for cartilage and other soft hydrated connective tissues—I. Equilibrium results. *J. Biomech.* **23,** 145–155 (1990).

34. Aziz, A. H. *et al.* Mechanical characterization of sequentially layered photo-clickable thiol-ene hydrogels. *J. Mech. Behav. Biomed. Mater.* **65,** 454–465 (2017).

35. Ahmed, S., Nakajima, T., Kurokawa, T., Anamul Haque, M. & Gong, J. P. Brittle–ductile transition of double network hydrogels: Mechanical balance of two networks as the key factor. *Polymer (Guildf).* **55,** 914–923 (2014).

36. Creton, C. *et al.* Fracture and adhesion of soft materials: a review. *Reports Prog. Phys.* **79,** 46601 (2016).

# Chapter 5- Photopatterned Variable-Modulus Hydrogel

## 5.1 Executive Summary

Employing the technique developed in Chapter 4 with the same cytocompatible photo-clickable solution, this chapter presents photopatterned hydrogels with locally enhanced mechanical properties using a single precursor solution formulation. To measure the concentration of mobile monomer attachment to the network, a quantitative confocal fluorescence microscopy technique is developed and applied to samples illuminated with variable intensity and exposure times. These data are then compared to the models presented in Chapter 3 to predict the concentration of attached species and differential swelling across the photopattern as a function of exposure time and intensity. Finally, combining the bulk properties measured in Chapter 4 with the known, printed species concentration, a model to predict the modulus across the photopattern is shown and compared to atomic force microscopy elastic modulus measurements across the photopatterned hydrogel. This comparison qualitatively validates the use of the predictive model and the single-precursor-solution technique to fabricate locally-defined, variable modulus hydrogels.

## 5.2 Introduction

As discussed in Chapter 3, spatial control of mechanical and chemical properties in regenerative constructs is required to recapitulate the extracellular environment of cells during tissue formation. Research demonstrates that stem cell development is significantly affected by their local extracellular environment.[1,2] For example, by solely changing the stiffness of the hydrogel surrounding mesenchymal stem cells (MSCs), cells exposed to an extracellular environment with a modulus of ~190 kPa preferentially differentiated into bone precursor cells while MSCs exposed to and environment of ~80kPa differentiated into cartilage precursor cells.[3] Therefore, the ability to locally define the mechanical properties that cells experience will enable spatial control of cellular differentiation and proliferation.[3–7]

Because switching printing resins is nontrivial for SLA systems and is cytotoxic, I demonstrate a technique to locally modify the mechanical properties of a cytocompatible

hydrogel using a single printing solution. A hydrogel is photopolymerized followed by in-swelling of fresh precursor solution into the existing network. This technique uses a precursor solution with functional groups at an off-stoichiometry ratio of 0.5:1. The initial hydrogel thus has unreacted groups to which fresh monomer will react when photopatterned in later cycles. Bulk hydrogels with variable mechanical properties were fabricated in Chapter 4 using this technique. Here the same technique in the SLA-AM photopatterning system is applied to produce spatially-controlled variable modulus hydrogels, measured using both confocal fluorescence microscopy and atomic force microscopy to determine the thiol concentration across the pattern and elastic modulus, respectively. In addition, the model presented in Chapter 3 predicting photopattern fidelity is then compared to the fidelity of the photopatterned hydrogels. The elastic modulus across the photopatterned hydrogels was then determined using atomic force microscopy and compared to the expected modulus, which was predicted by combining the bulk hydrogel properties in Chapter 4 with the thiol concentration across the photopatterned hydrogel.

## 5.3 Experimental Procedure

### *5.3.1 Materials*

Poly(ethylene glycol) dithiol (PEG-dithiol (Sigma Aldrich, MW 1,000 Da), poly(ethylene glycol) thiol (tripentaerythritol) (JenKem USA, 8ARM-PEG-SH, MW 10,000 Da), lithium phenyl-2,4,6-trimethylbenzoylphosphinate (LAP) (Colorado Photopolymer Solutions), and fluorescent molecule maleimide AlexaFluor-546 (Sigma Aldrich) were used as received. 5-norbornene-2-carboxylic acid (NB) (Sigma Aldrich) was conjugated to poly(ethylene glycol) amine (PEG-$NH_2$) (JenKem USA, 8arm PEG amine, HCl salt, MW 10,000 Da) at room temperature (RT) under an argon purge to produce poly(ethylene glycol) norbornene (PEG-NB).[13] This was done by dissolving PEG-$NH_2$ (10 g) in dimethylformamide (DMF) (15mL) and dichloromethane at 1:1 ratio to which the solution containing 4-molar excess NB (4.42g), 2 molar excess 2-(1H-7-Azabenzotriazol-1-yl)-1,1,3,3-tetramethyl uronium hexafluorophosphate methanaminium (HATU, AKSci) (9.12g), and 2 molar excess N,N-diisopropylethylamine (DIEA, Sigma) (6.2 g) was reacted with for 48 hours. The solution was precipitated in diethyl ether, dialyzed four times with di$H_2O$ over two days, and lyophilized. The resulting 8-arm PEG-

NB product conjugation of 99% (percentage of NB conjugated PEG arms), referred to herein as PEG-NB. The degree of norbornene conjugation was determined by $^{1}$HNMR (Bruker AV-III 400) by comparing the area under the peak for the allylic hydrogen closest to the norbornene bridged cyclic hydrocarbon group (resonance from ~3.1 to 3.2 ppm) to the area under the peak for the methyl groups in the PEG backbone (resonance from ~3.4 to 3.85 ppm), see Figure 4.2 for $^{1}$HNMR spectrum. Macromers were dissolved in phosphate-buffered saline (PBS) (OmniPur, Calbiochem).

*5.3.2 Photopatterned Sample preparation*

The bulk hydrogel precursor solution was synthesized by combining 8.55 wt% 10kDa PEG-NB by mass to phosphate buffered saline and allowed to mix overnight at 3 degrees C. Immediately prior to photopolymerization, 1.45 wt% 1kDa PEG-dithiol was added to the NB solution with 0.05 wt% LAP to produce an effective 10 wt% monomer concentration. The photopatterning precursor solution was synthesized using the same method except the thiol fluorescent tag, AlexaFluor 546, was reacted with PEG-dithiol overnight at 3 degrees C in a 1:3000 functional group ratio, which ensured the fluorescent tag did not affect the final material properties significantly.

As shown in Figure 4.1, the precursor solution was deposited between a methacrylate coated glass slide (Cell Associates) and a RainX coated coverslip with 12.5 μm shims and secured using clips. The methacrylated sample substrate was used to ensure covalent bonding to glass, while the RainX was used to reduce adhesion between the fabricated hydrogel and the coverslip. The sample was flood-polymerized for 2 minutes using a collimated mercury lamp source at 30 mW/cm$^2$ to ensure uniform, full conversion, the sample was swollen for ~1 hour with the fluorophore-labeled precursor solution applied from the edges and then immediately photopatterned at 20 mW/cm$^2$ using the stereolithography (SLA) system described in Chapter 2. Actuators position the sample to enable 24 different exposures with exposure times of 7.5-25s in 2.5s increments, 30s, and 35s. Because the most significant change in mechanical properties was achieved after a single in-swelling and exposing cycle in Chapter 4, only a single cycle was used here.

To confine photopatterning analysis to one dimension for simple comparison to the model presented in Chapter 3, the samples were exposed with a 1.03 mm by 1.99 mm rectangle

photopattern for a range of exposure times (s). Features were patterned using three exposure intensities (I= 5, 10, and 20 mW/cm$^2$) to investigate the relationship between $d_c$ and intensity. To probe if the hydrogel chemistry has reciprocity, where equivalent doses (exposure time X intensity) result in equivalent polymerization, i.e., $t_{exp}$(20 mW/cm$^2$)= 2$t_{exp}$(10 mW/cm$^2$), each intensity was probed over a range of doses (20, 50, 100, 150, 200, 250, 300, and 400 mJ/cm$^2$). Immediately following photopatterning, the samples were placed in a bath of deionized (DI) water for 24 hours to remove all unreacted monomer and finally stored in a light-proof container to prevent the fluorophore from photo-bleaching.

Photopattern fidelity was probed using the same patterning technique discussed above, changing only the photopattern, which was designed with a range of feature widths (10-210 µm) and feature separation distances (~20-100 µm). The varied widths and separation distances in the pattern explored both the critical dimension of the photopatterning system and the effect that feature proximity has on adjacent feature development. All samples were then imaged using confocal fluorescence microscopy, and samples patterned using the resolution photomask were additionally probed using atomic force microscopy.

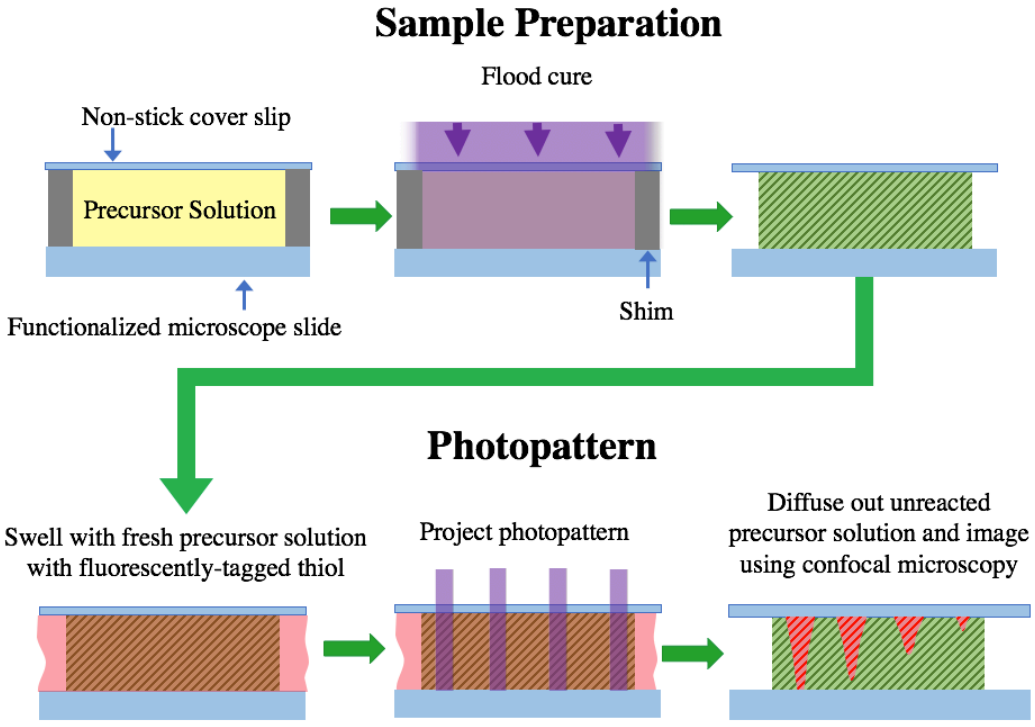

**Figure 5.1** Schematic of the sample preparation, in-swelling with the fluorescently-tagged thiol precursor solution, and then photopatterning using the SLA-AM system from Chapter 2.

*5.3.3 Confocal Fluorescence Microscopy*

The samples were imaged on a confocal microscope using a 10X water immersion objective. Various detector gains (DG) were required to match the fluorescence of the samples. Calibration curves were developed for each DG such that concentration of fluorophore and thus thiol concentration could be calculated from the confocal images.

To develop the calibration curve, five concentrations of fluorophore (0.1, 0.05, 0.01,0.001, and 0.0001 mM) were imaged by sweeping through all viable DG values, keeping all other imaging conditions constant (*e.g.*, pinhole diameter, amplifier offset, etc.). The upper and lower bounds for the DG values probed were the highest value at which the detector did not saturate and the lowest DG value with a detectable signal, respectively. The images at each DG value were processed by taking a full-field average and standard deviation of the fluorescence intensity across the image.

The average fluorescence intensity, reported as a digitized photocurrent from the detector, was then normalized by the level (256) and plotted as a function of DG for each fluorophore concentration tested, shown in **Figure 5.2**. Each curve was then fit to a power law. The resulting calibration curves and $R^2$ values of the fits are reported in **Table 5.1**. The DG values used to image the samples taken on a given day were then used to calculate the concentration of fluorophore present in order to produce the observed fluorescence intensity (**Figure 5.2**). A linear regression analysis was conducted using the plotted fluorescence intensity vs. fluorophore concentration and the representative linear equations for each DG value used in sample imaging, shown in **Table 5.2**. The linear regression fit equations were used to calibrate the concentration of fluorophore that is present in the photopattern at each given DG value. This concentration was then multiplied by the known ratio of fluorophore to thiol (3000) to calculate the concentration of photo-attached PEG-dithiol present in the imaged sample. The same thiol concentration baseline was used for each photopattern, which was determined by imaging an unexposed region of the hydrogel adjacent to the photopattern confocal fluorescence microscopy.

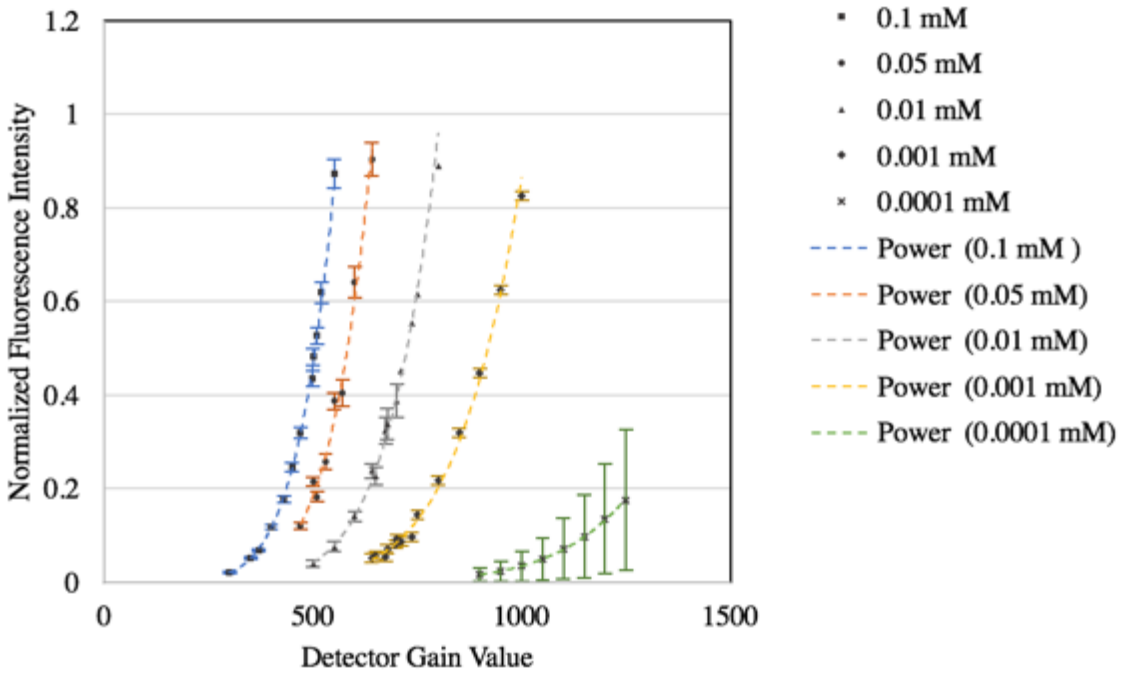


**Figure 5.2** Fluorescence intensity calibration curves with the power fit analyses plotted over the observed intensity values at each fluorophore concentration (blue=0.1 mM, orange = 0.05 mM, gray=0.01 mM, yellow=0.001 mM, and green=0.0001 mM), where the dashed line indicates the power model and the error bars indicate one standard deviation.

| Concentration (mM) | Fit Analysis | $R^2$ Value |
|---|---|---|
| 0.1 | $I_{fluor} = 9 \cdot 10^{-18} x_{DG}^{6.19}$ | 0.999 |
| 0.05 | $I_{fluor} = 5 \cdot 10^{-19} x_{DG}^{5.52}$ | 0.978 |
| 0.01 | $I_{fluor} = 5 \cdot 10^{-20} x_{DG}^{6.66}$ | 0.997 |
| 0.001 | $I_{fluor} = 2 \cdot 10^{-20} x_{DG}^{6.52}$ | 0.988 |
| 0.0001 | $I_{fluor} = 3 \cdot 10^{-24} x_{DG}^{7.36}$ | 0.999 |

**Table 5.1** Power fit analyses used to extrapolate from the observed fluorescence intensities at a given DG to include values beyond the graylevel range of the confocal photodetector with $R^2$ to represent the goodness of fit.

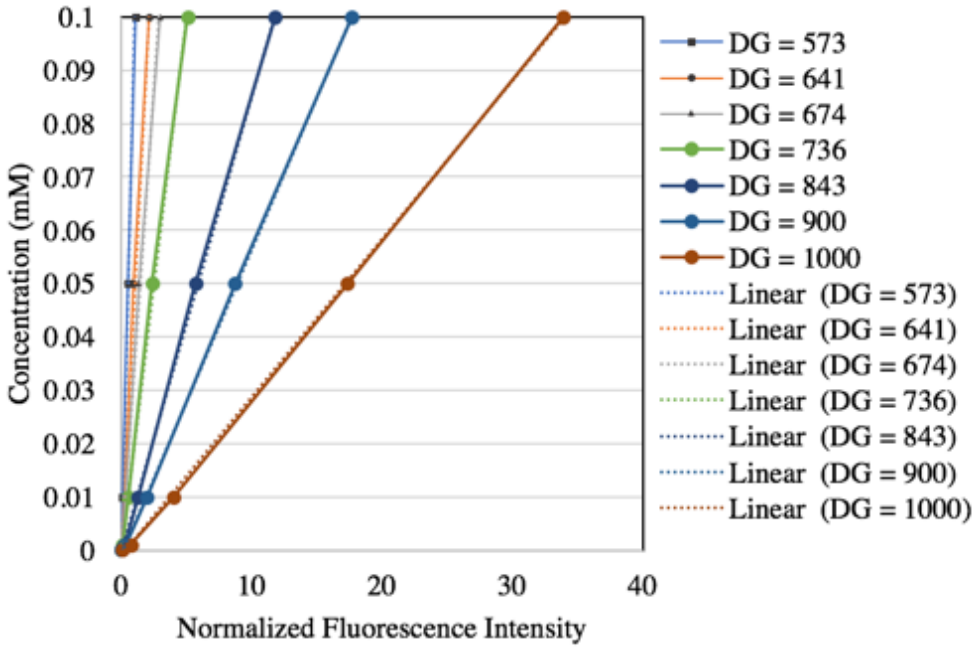


**Figure 5.3** Fluorescence intensity plotted versus known fluorophore concentration, from which a linear fit of each data set was used to determine photopatterned fluorophore/thiol concentration (dotted line).

| DG Value | Fit Analysis | $R^2$ Value |
|---|---|---|
| 573 | $C_{fluor} = 0.0952 \cdot I_{fluor}$ | 0.994 |
| 641 | $C_{fluor} = 0.0473 \cdot I_{fluor}$ | 0.996 |
| 674 | $C_{fluor} = 0.0346 \cdot I_{fluor}$ | 0.997 |
| 736 | $C_{fluor} = 0.0199 \cdot I_{fluor}$ | 0.998 |
| 843 | $C_{fluor} = 0.0085 \cdot I_{fluor}$ | 0.999 |
| 900 | $C_{fluor} = 0.0057 \cdot I_{fluor}$ | 0.999 |
| 1000 | $C_{fluor} = 0.0029 \cdot I_{fluor}$ | 0.999 |

**Table 5.2** Working curve calibration equations used to determine the fluorophore and thus thiol concentration in the photopatterned region of each sample, where $R^2$ was used to validate the model as a representative curve for the data.

The attached thiol concentration measured by the fluorescent method described above was then correlated to a measure of crosslinking density to predict an increased modulus at each location using the properties of the single SE cycle bulk gels measured in Chapter 4. The bulk hydrogels were fabricated with four different functional group ratios of thiol:norbornene (0.25:1, 0.5:1, 0.75:1, and 1:1) and their compressive moduli ($E_c$) were found to increase linearly with

increased thiol concentration [SH] ($E_c = 1.44[SH] - 42$ with $R^2 = 0.98$). Assuming only thiol species diffuse in and attach to the existing matrix, **Figure 5.4** shows the predicted modulus increase with increased thiol concentration within the hydrogel. This model combines data presented in **Figure 4.6** with the thiol concentration, [SH], obtained from confocal fluorescence images to predict the modulus increase with increased thiol concentration. Though the compressive modulus presented in Chapter 4 for the bulk materials is not precisely equivalent to elastic modulus, here they are treated as equivalent. The elastic modulus of these photopatterned hydrogels was then found using atomic force microscopy and compared to the expected moduli.

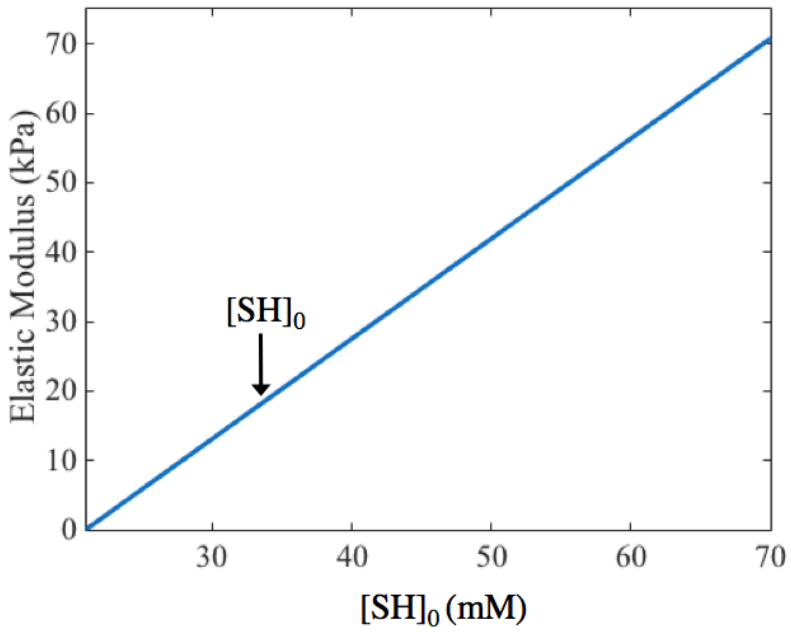


**Figure 5.4** Plot displaying the predicted relationship between increased thiol concentration in the photopattern ($[SH]_p$) and increased modulus, where the arrow indicates the elastic modulus and thiol concentration for bulk hydrogel samples fabricated using equivalent precursor solution formulation to the photopatterned samples (10wt% monomer, 0.5:1 thiol: norbornene).

*5.3.4 Atomic Force Microscopy*

Atomic force microscopy (AFM, Asylum Research MFP 3D Classic AFM) was used to determine the elastic modulus of the photopatterned hydrogels. AFM was conducted in two modes, one to image the surface topography and the other to probe the hydrogel elastic modulus. These two modes combine to produce a representative map of the hydrogel elastic modulus

across the sample and the corresponding surface topography, which captures surface contamination that can influence elastic modulus measurements.

Contact Mode AFM was used to image the photopatterned hydrogel surface topography.[8–10] In this mode, the AFM cantilever physically contacts the sample and remains in contact as it scans across the surface, maintaining a constant force. As the cantilever encounters a topographic depression, the voltage and subsequent measured force drops, which requires the cantilever to translate down to maintain constant force. Displacement of the cantilever measured by the optical feedback system produces a topographic map of the sample.

Force Volume Mapping was used to determine the elastic modulus of the photopatterned hydrogels.[11] This technique requires the cantilever to physically detect the surface and indent a user-defined distance into the sample. The cantilever detects the insertion force as a function of indentation depth using a position sensitive detector, producing a stress versus strain curve.[11] With soft (10s kPa), adhesive hydrogels it is critical to ensure the cantilever sufficiently releases from the sample surface to obtain valid force curve information. These force curves are then run through a fitting routine using the Hertz Model to extract the elastic modulus.[12] 90 X 90 μm AFM scans were digitally combined to produce a 25 μm by X measurement of the ~1300 x 1300 μm photo-pattern . The image scan-size for the topographic mapping in Contact Mode was 25 X 90μm (128 by 128 pixels or 16,384 total pixels probed). The same scan-size was used for the force map (25 X 90μm), but the pixels probed decreased to 264 (8 by 33 pixels) to decrease total probing time. All data was processed through a Savitsky-Golay digital smoothing filter that enhances the signal to noise ratio without greatly affecting the signal, which is low due to surface variability and contaminants (*e.g.*, air bubbles, delaminated hydrogel, etc.).[13]

*5.3.5 Photopattern intensity characterization*

The intensity across the photopattern region of the SLA-AM system was characterized to ensure uniform photopatterning. The average intensity variation across the photopattern was ~5% with a maximum roll-off of 15% at one photopattern corner, as shown in **Figure 5.5** at the intersection of the dashed purple and dashed orange lines that indicate where the intensity profile was taken**.** This characterization quantifies that any anomalous features in the photopatterned hydrogel were not due to non-uniform intensity.

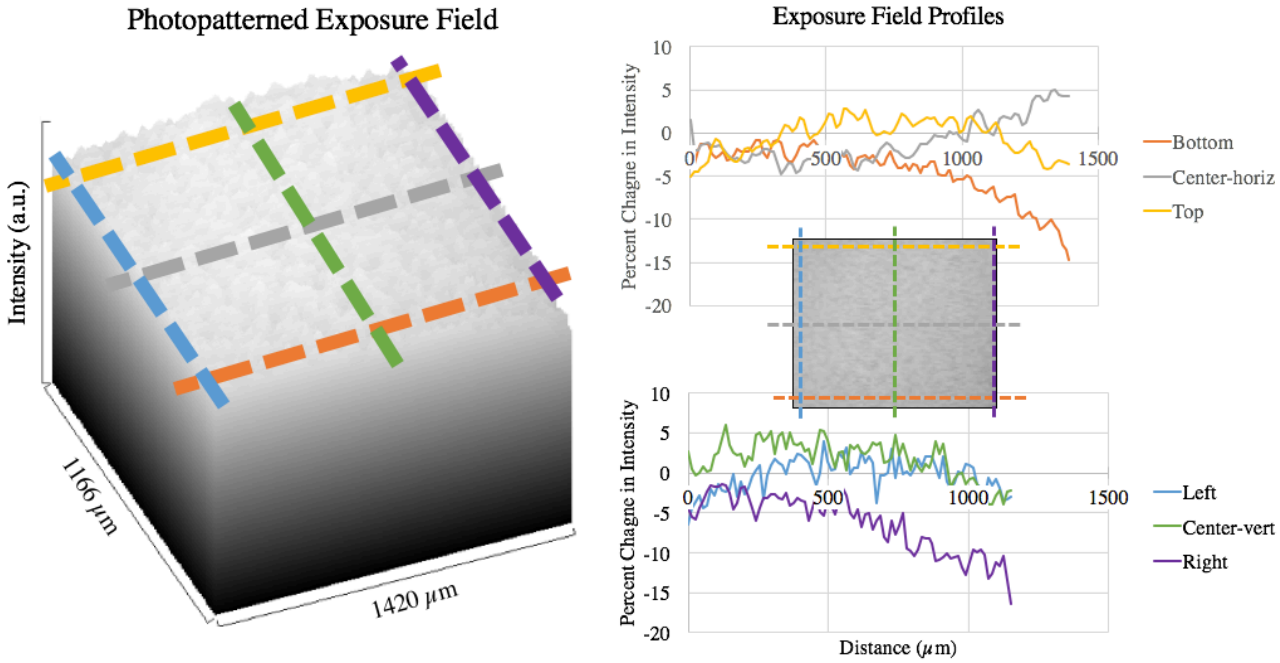


**Figure 5.5** Surface plot of the photopattern intensity variation across the exposure field with the dashed lines indicating the region at which the intensity variation was probed, where yellow = top, gray = center-horizontal, orange = bottom, blue = left, green = center-vertical, and purple = right. The plots to the right display the percent change in intensity as a function of distance across the photopattern at the probed regions described previously, with the inset image displaying the 2D intensity output on the sample plane where the dashed lines further highlight the regions probed.

## 5.4 Results and Discussion

### *5.4.1 One-dimensional photopattern characterization*

Three distinct features are observed in the photopatterned hydrogel when the thiol concentration across the photopattern edge is plotted for each exposure time and intensity, where profiles were taken through the center of the photopattern and represent the average of 100 pixels (**Figure 5.6**a). (I) The thiol concentration inside the photopattern edge ($[SH_p]$) is greater than the initial thiol concentration ($[SH_0]$) in the precursor solution. (II) The thiol concentration falls off rapidly as a function of distance from the photopattern edge. (III) The thiol concentration peak is located a distance inside the photopattern, away from the photopattern edge.

(a)

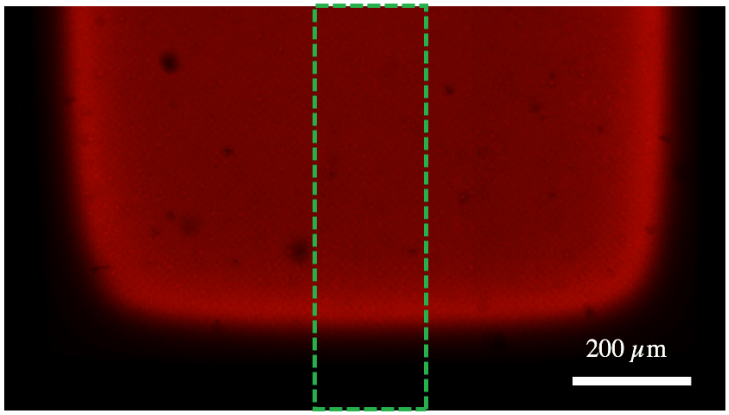
200 μm

(b)

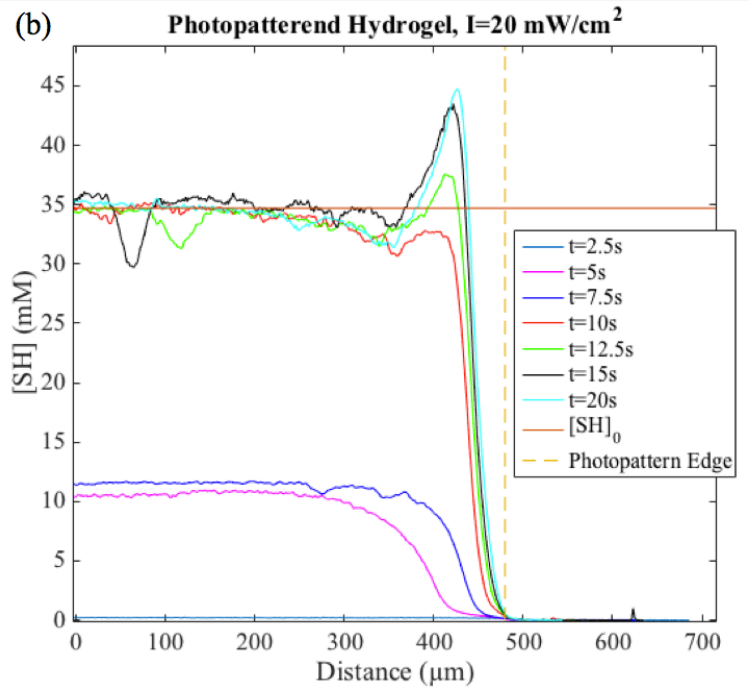
Photopatterend Hydrogel, I=20 mW/cm2
[SH] (mM)
Distance (μm)
t=2.5s
t=5s
t=7.5s
t=10s
t=12.5s
t=15s
t=20s
[SH]0
Photopattern Edge

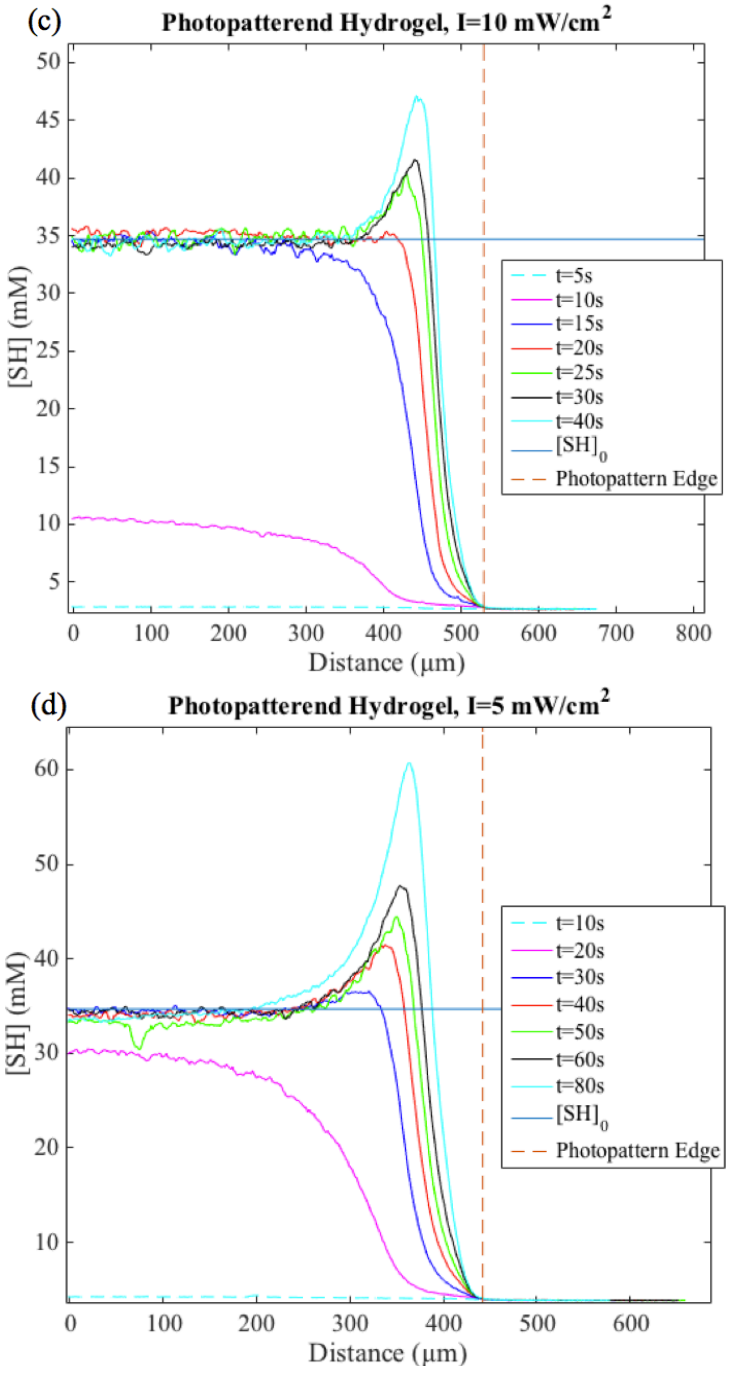


**Figure 5.6** (a) Stitched confocal fluorescence images of the photopatterned sample where the green dashed box indicates the region where the fluorescence was taken and averaged and the blue dashed box image shows the visible pixels in the sample. (b-d) Thiol concentration in the precursor solution plotted as a function of distance across the sample for varied exposure time t and for (b) I=20 mW/cm$^2$, (c) I=10 mW/cm$^2$, and (d) I=5 mW/cm$^2$. Each color represents the same amount of energy delivered to the photopattern across each sample, where dashed cyan=50 mJ/cm$^2$, magenta= 100 mJ/cm$^2$, royal blue=150 mJ/cm$^2$, red= 200 mJ/cm$^2$, green= 250 mJ/cm$^2$, black= 300, mJ/cm$^2$, and cyan= 400 mJ/cm$^2$. The orange horizontal line indicates the

concentration of thiol in the initial formulation and the dashed yellow line indicates the boundary of the photopattern, where everything left of the line was exposed to the indicated intensity 405 nm light.

The enhanced thiol concentration at the photopattern edge, Feature I, is visible for all exposure intensities (**Figure 5.6**b-c). Depletion of thiol monomer inside the photopattern generates a chemical gradient that causes thiol monomers outside of the photopattern to diffuse in during polymerization. The distance thiol monomers can diffuse into the photopattern before reacting given a set of experimental conditions is modeled in Chapter 3 as $d_{c\mathrm{SH}}$ and is represented by the distribution of thiol at the photopattern edge. The enhanced concentration of polymer at the edges of exposures is documented in the holographic photopolymers community and is referred to as Zhao-Mouroulis 'horns', which appear when diffusivity in the polymer matrix is lower than polymerization reactivity.[14] **Figure 5.7** is a plot by Zhao et al. demonstrating the formation of enhanced polymer concentration at photopattern edges, as indicated by the parameter R, which is proportional to $\mathrm{D}/k_{\mathrm{p}}$, where D is monomer diffusivity and $k_{\mathrm{p}}$ is the polymerization reaction reactivity.[14]

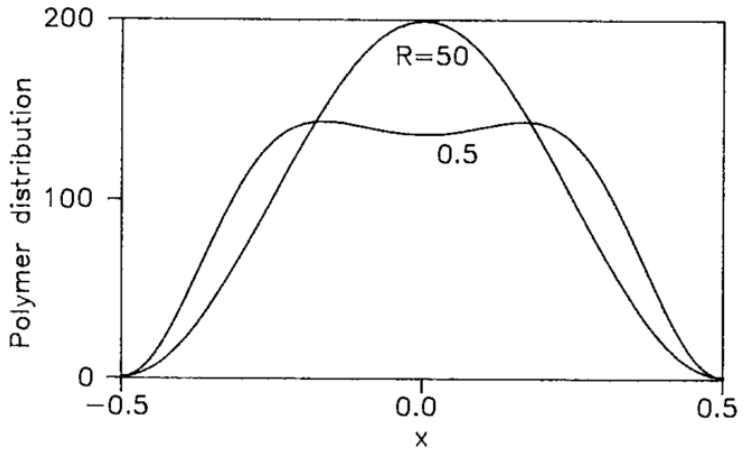


**Figure 5.7** Plot by Zhao et al. depicting the polymer distribution as a function of distance across a photopattern, where $\mathrm{R} \propto \mathrm{D}/k_{\mathrm{p}}$, indicating the formation of so-called 'horns' at the photopattern edges when diffusivity is comparable or slower than the rate of polymerization.[14]

The full-width half max (FWHM) of Feature I is directly comparable to the characteristic diffusion-reaction distance ($d_{\mathrm{cSH}}$) modeled in Chapter 3. The 'findpeaks' algorithm in MatLab was used to determine the location, full width half max (FWHM), and prominence of the peak concentration at the photopattern edge as a function of varied exposure time and intensity. For

each intensity, the FWHM of the enhanced edge varied little with respect to exposure time (10%, 3%, and 16% for I=5, 10, and 20 mW/cm$^2$, respectively), observing solely an increased peak amplitude with increased exposure time, as shown in **Figure 5.6**b-d and represented by the error bars in **Figure 5.8**.

The input parameters used to model the characteristic distance a species can diffusing before reacting were the documented values for thiol:norbornene the termination coefficient ($k_t = 3 \times 10^8$ M$^{-1}$s$^{-1}$) and the documented values for the diffusion coefficient of similarly-sized PEG molecules diffusing through a comparably crosslinked network ($D_{\mathrm{SH}} = 85\ \mu$m$^2$s$^{-1}$).[15,16]. The propagation/chain transfer coefficient is the sole parameter fit in the model at a value of $k_{\mathrm{p}} = k_{\mathrm{ct}} = 1.3 \times 10^6$ M$^{-1}$s$^{-1}$, which is well within range documented in the literature ($k_{\mathrm{p}} = k_{\mathrm{ct}}$ between $1 \times 10^5$- $3.1 \times 10^6$ M$^{-1}$s$^{-1}$).[17,18]

The standard deviation of the FWHM of the enhanced thiol concentration peak at each intensity and exposure time fell within or just outside of 90% confidence bounds of the modeled characteristic distance a thiol monomer diffuses into the photopattern before reacting (**Figure 5.8**). Slight variations of the model from experiment could be an artifact of using FWHM as a representative measure of feature width, which is not perfectly Gaussian and is asymmetric (**Figure 5.6**b-d). This model can therefore predict the width of the enhanced thiol concentration at the photopattern edges for the thiol-ene hydrogel system used, which can then be compensated for or exploited to precisely control photopatterned mechanical properties.

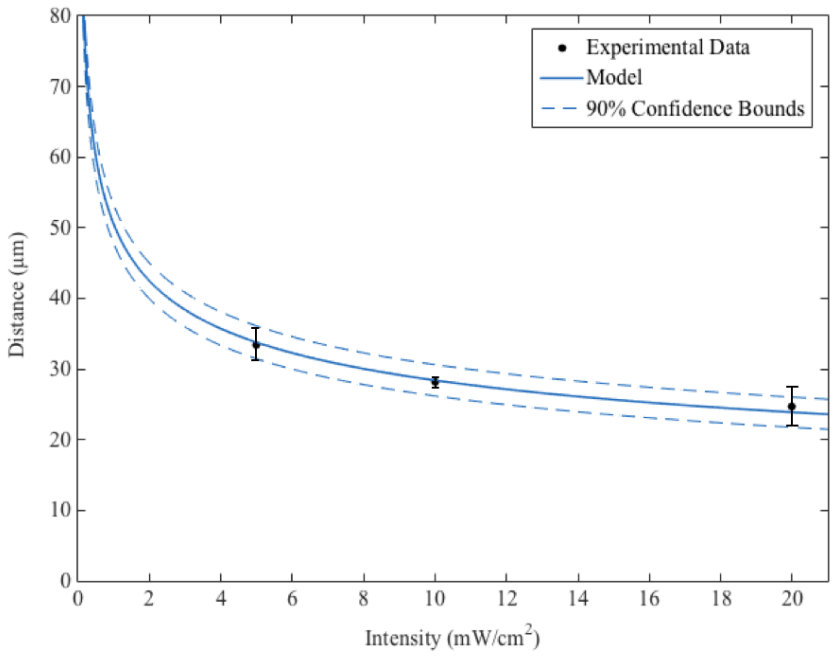


**Figure 5.8** Full-width half max (FWHM) of measured diffusion/reaction distance as a function of increased incident I= 5, 10, and 20 mW/cm$^2$ plotted with the model and its 90% confidence bounds. Error bars indicate the experiment standard deviation.

The amplitude of the diffusion-reaction peak and thus thiol concentration is also dependent on the combination of incident intensity and exposure time. Due to the slower diffusion rate of the larger PEG-NB with respect to the PEG-dithiol monomer, equivalent doses at different intensities result in different concentrations of PEG-dithiol at the photopattern edge.[15] At lower intensities, both PEG-NB and PEG-dithiol diffuse into the photopattern, providing a higher concentration of PEG-NB reactive sites to which diffusing PEG-dithiol reacts, as shown in **Figure 5.6**b-d. This effect is reflected in the thiol concentration profiles, where **Figure 5.6**b-d plotted lines of the same color indicate the same exposure dose. For equivalent doses, the thiol concentration at the photopattern edge builds up by a larger concentration for lower intensities, where $[SH]_{I=5} > [SH]_{I=10} > [SH]_{I=20}$ while the thiol concentration at the photopattern center reaches a maximum of $[SH]_0$ and remains constant (**Figure 5.9**). Though PEG-dithiol is solely modeled, these data support the hypothesis that this is not a reciprocal system with respect to exposure time and intensity.

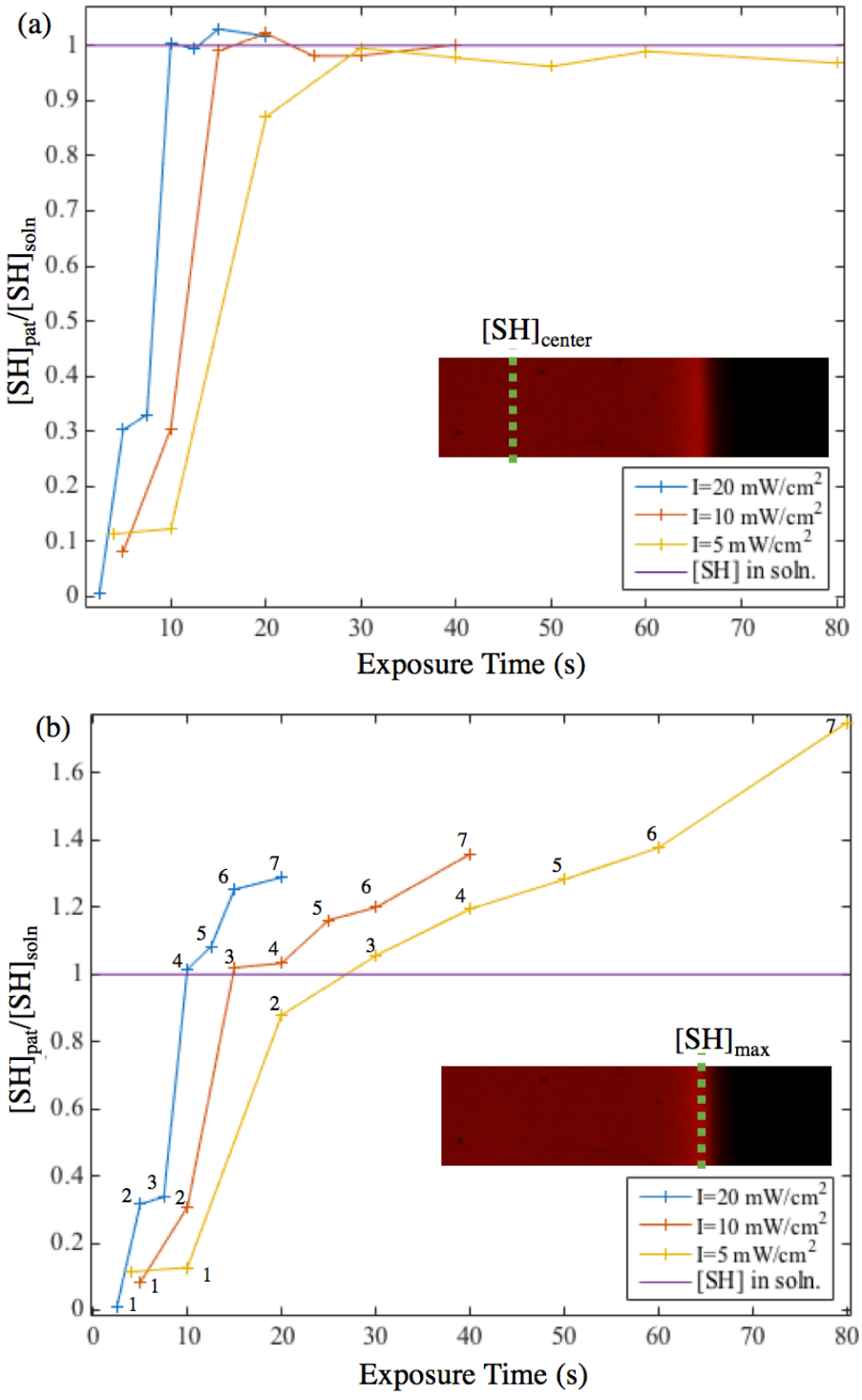


**Figure 5.9** Thiol concentration normalized to concentration of thiol in the precursor solution plotted as a function of exposure time for I= 5 (yellow), 10 (red), and 20 mW/cm$^2$(blue) measured at both (a) the center and (b) the edge of the photopattern, where equivalent energy doses are labeled with numbers 1-7 for reference. The inset fluorescent images and green dashed line indicate the location at which the data were taken for each plot.

The second feature of note, Feature II, is the low thiol concentration immediately outside of the photopatterned region. Thiyl radicals are produced within the photopattern, which produce a chemical gradient that drives the diffusion of radicals out of the pattern. The distance thiyl radicals can diffuse out of the photopattern before reacting with the surrounding matrix is the characteristic diffusion-reaction distance modeled in Chapter 3 ($d_{cs.}$). Though the reactivity and diffusivity of the thiyl radicals and thiol monomers are constant, the high concentration of norbornene groups outside the photopattern reduce the characteristic distance by $10^3$, where $d_{cs.} \approx 50$nm. This distance informs the ability to pattern high-fidelity features because it governs the distribution of polymer outside of the photopattern. High-fidelity features are achievable with the thiol:norbornene hydrogel chemistry used here given the short characteristic diffusion-reaction distance of thiyl radicals.

The third distinct feature, Feature III, is the movement of the thiol concentration peak away from photopattern edge. **Figure 5.10** displays two confocal fluorescent microscope images of the photopatterned hydrogel taken at a two detector gains, one where the detector is not saturated and one where the detector is saturated. The saturated image displays the distinct photopattern edge with the predicted rapid thiol concentration decrease and the unsaturated image displays the enhanced thiol concentration edge. When the two images are overlaid, the thiol concentration peak is distinctly shifted inside of the photopattern boundaries (**Figure 5.10**).

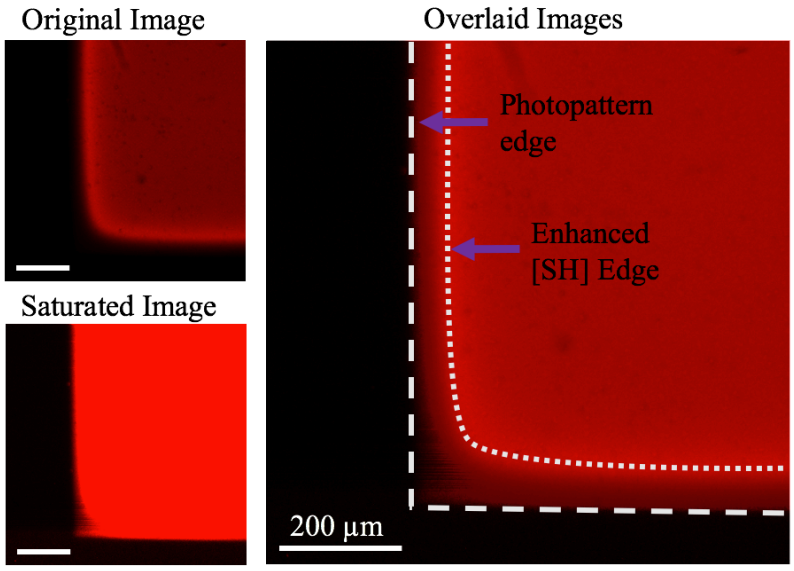


**Figure 5.10** Confocal fluorescent microscope images displaying the original, unsaturated image, the saturated image, and then an image of the original and saturated images overlaid. The

overlaid images demonstrate the movemeFigure 5.10nt of the edge of enhanced thiol concentration (dotted line) moving away from the photopattern edge (dashed line).

Chapter 3 modeled the effects of differential swelling as a result of increased crosslinking density, and Chapter 4 verified that bulk hydrogels polymerized using the same experimental conditions displayed a decrease in their equilibrium swelling ratio with increased swelling and exposing cycles. This result indicates that hydrogels fabricated using this precursor solution become less able to be swollen with increased crosslinking density. Therefore, the movement of the thiol concentration peak can be attributed to the differential swelling caused by increased crosslinking within the photopattern.

Using the linear deformation from the bulk hydrogels presented in Chapter 4 that underwent zero diffusion-exposure cycles ($\lambda_0$) and those that were swollen with fresh precursor solution and polymerized ($\lambda_P$), the expected linear deformation ratio is $\lambda_P/\lambda_0 = 0.96$. Given this ratio and a photopattern half-width of 0.99 mm, the photopatterned hydrogel is predicted to shrink inward by 39 μm. For all photopattern intensities, the FWHM of depleted thiol concentration region generated by the shifted peak was between 30-50 μm, which is in agreement with the differential swelling effect modeled in Chapter 3. This model does not account for increased crosslink density at the photopattern edges, which can cause increased differential swelling in these regions. The enhanced crosslinking density causes the feature to shrink by a larger percent than the assumption of uniform crosslinking, which is most representative at the center of the photopattern.

Features photopatterned in materials with reaction-induced differential swelling require exposure times shorter than the propagation time or the swelling will deform the matrix during photopolymerization and significantly blur the features. This deformation affect is demonstrated by the enhanced thiol concentration at the photopattern edge getting pulled away from the true photopattern edges. If this criterion is met, the photopatterned hydrogel will still be distorted by differential swelling. There are two mechanisms to avoid the build-up of species at the photopattern edges, representing an increased crosslinking density, (1) the total species conversion must be reduced or (2) diffusion rate and polymerization time must be significantly different. Though thiol and norbornene are highly reactive, the low concentration of total species increases the polymerization time, which allows diffusion to occur during polymerization. If all

criteria are met, hydrogel structures can be photopatterned with resolution and fidelity limited by the diffusion reaction transport distance, which is ~100s nm.

These three features have distinctly different scales, shapes and temporal dynamics. Feature III develops when the equilibrium water concentration is disrupted, which occurs immediately once the swollen hydrogel is illuminated. Feature I occurs only after significant monomer is consumed to produce a chemical gradient driving monomer diffusion into the photopattern. Feature II also develops once a significant concentration or radicals are generated, but is negligible due to the short characteristic diffusion-reaction distance. Because Feature III reduces [SH] at the pattern edge, while Feature I increases the edge concentration, balancing these two effects at intermediate times will allow them to roughly compensate for one another, although with a shift due to continued shrinkage.

*5.4.2 Photopatterned hydrogel*

Hydrogels were exposed to the two patterns shown in **Figure 5.11** using an illumination intensity of 20 mW/cm$^2$. The resolution pattern shown on the top left probes both the minimum feature size and the resolution of the hydrogel patterning system, while the grid pattern probes the interaction between closely patterned, repeating features (**Figure 5.11**). Line widths in the left pattern were 210, 105, 52, 26, 13, and 10 μm labeled 1-6, respectively, at two spacing distances of 78 μm (left) and 39 μm (right). The grid pattern was ~50 X 50 μm squares separated by ~50 μm. Due to the rotated orientation of the DMD pixels and the algorithm that translates the bitmap into DMD pixels, half of the squares are larger by a pixel width, as shown in **Figure 5.11**.

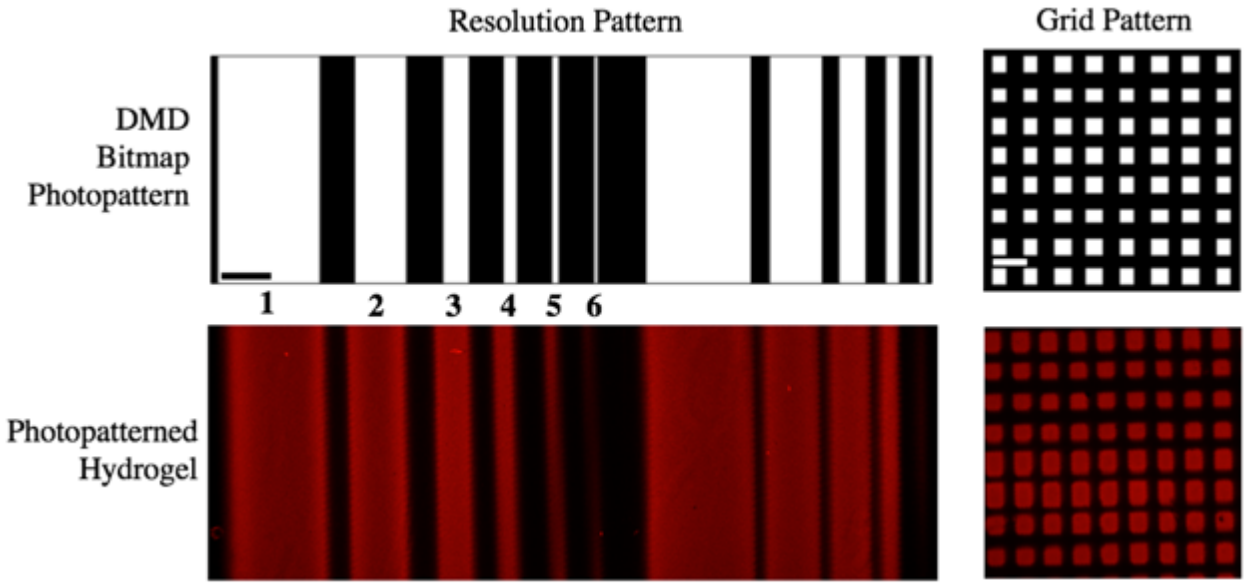


**Figure 5.11** Photopattern of both the resolution pattern and the grid photopattern with the subsequent confocal fluorescent microscope images of the photopatterned hydrogel, demonstrating both the high-fidelity features. Resolution pattern lines 1-6 are 210, 105, 52, 26, 13, and 10 μm, respectively, on the sample plane. The scale bar designates 100 μm.

Pixel-limited resolution (~10 μm) features were fabricated using the SLA-AM system with an exposure time of 25s at I=20 mW/cm$^2$, as demonstrated by the saw-tooth pattern along the photopattern edge representing the diagonal, rotated DMD pixels (**Figure 5.12**). As predicted by the one-dimensional photopatterning analysis, high-fidelity photopatterning is achievable using this SLA system due to the short diffusion-reaction distance (~50 nm) of the thiyl radicals, which preserve the photopattern edge. Also visible in **Figure 5.12** is the enhanced thiol concentration at the photopattern edge due to the ~30 μm diffusion reaction distance of thiol monomer. This is the first demonstration of pattering low solids content hydrogels (10 wt%) at the 10 μm length-scale without the addition of viscosifiers or cytotoxic concentrations of photoinitiator.

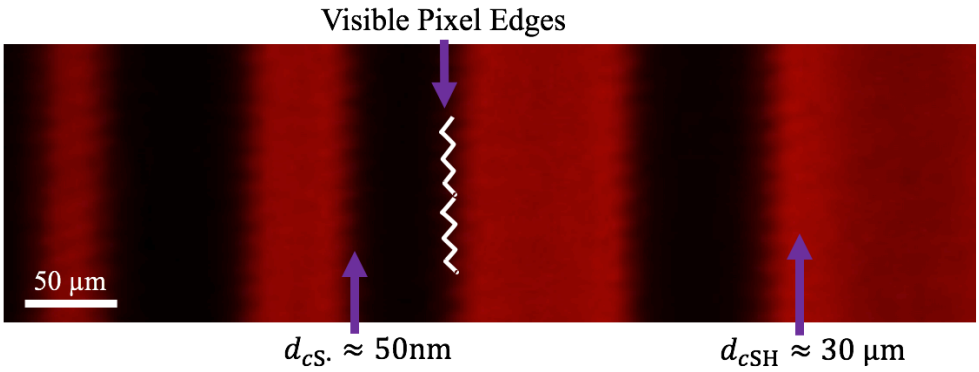


**Figure 5.12** Confocal fluorescent microscope image of hydrogel photopatterned for 25s at I=20 mW/cm$^2$ demonstrating high-fidelity photopatterning capability with pixel-limited resolution. The short characteristic distance for thiyl radicals diffusing out of the photopattern ($d_{cS\cdot}$) enables high fidelity patterning while enhanced thiol concentration at the photopattern edges is enabled by a longer characteristic reaction-diffusion distance of thiol species diffusing into the photopattern ($d_{cSH}$).

**Figure 5.13**a further demonstrates the ability to photopattern repeatable, high-fidelity structures within a single photopattern as a function of exposure time due to the nanometer-scale diffusion-reaction distance of thiyl radicals. As hypothesized, thiol concentration increases with increased exposure time, demonstrated by the increasing fluorescence images indicated by the varied detector gain values required to obtain an unsaturated confocal microscopy image in **Figure 5.13**b. As the photopattern develops with exposure time, the high-fidelity photopatterns exposed for $t_{exp} > 17.5$s show signs of the pixels at the photopattern edges (**Figure 5.13**b).

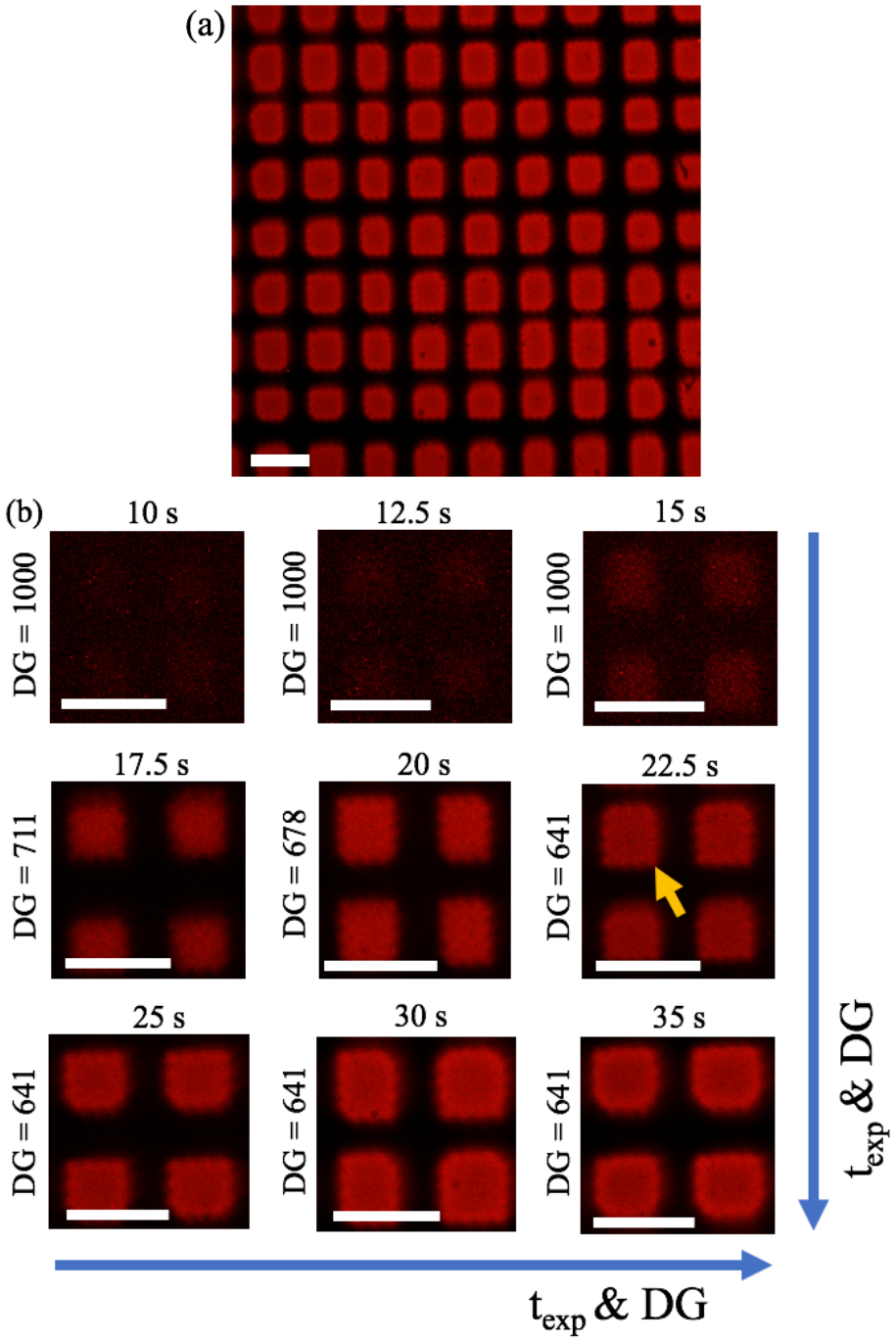


**Figure 5.13** (a) Confocal fluorescent image of photopatterned ~50 µm by ~50 µm grid exposed 30 s, displaying uniform photopatterning. Grid irregularity is an artifact of the software conversion of the bitmap photopattern to the programmable photomask. (b) Array of zoomed-in images of the grid photopattern exposed for nine different exposure times, noted above each image with the detector gain use to capture each image located to the left. The scale bar for all images indicates 100 µm.

The average thiol concentration at the center of the squares in the grid photopattern were taken for each exposure time and plotted as a function of exposure time to determine the relationship between the two for small patterns (~50 μm) (**Figure 5.14**). For the first five exposure times the increased thiol concentration follows an approximately exponential trend after which the concentration increase slows an equilibrates after $t_{exp} \approx$ 25 s (**Figure 5.14**). Because the average was taken at the center of the photopattern, this equilibration is likely due to the depletion of monomer in the unexposed regions between the grid of squares. This result highlights the importance of feature placement within the desired photopattern because features at the edges have an influx of newly diffused monomer while features at the center do not. The combination of the SLA-AM instrument and fluorescent testing enables control and measurement of thiol attachment throughout the photopattern to within ±1.5 mM.

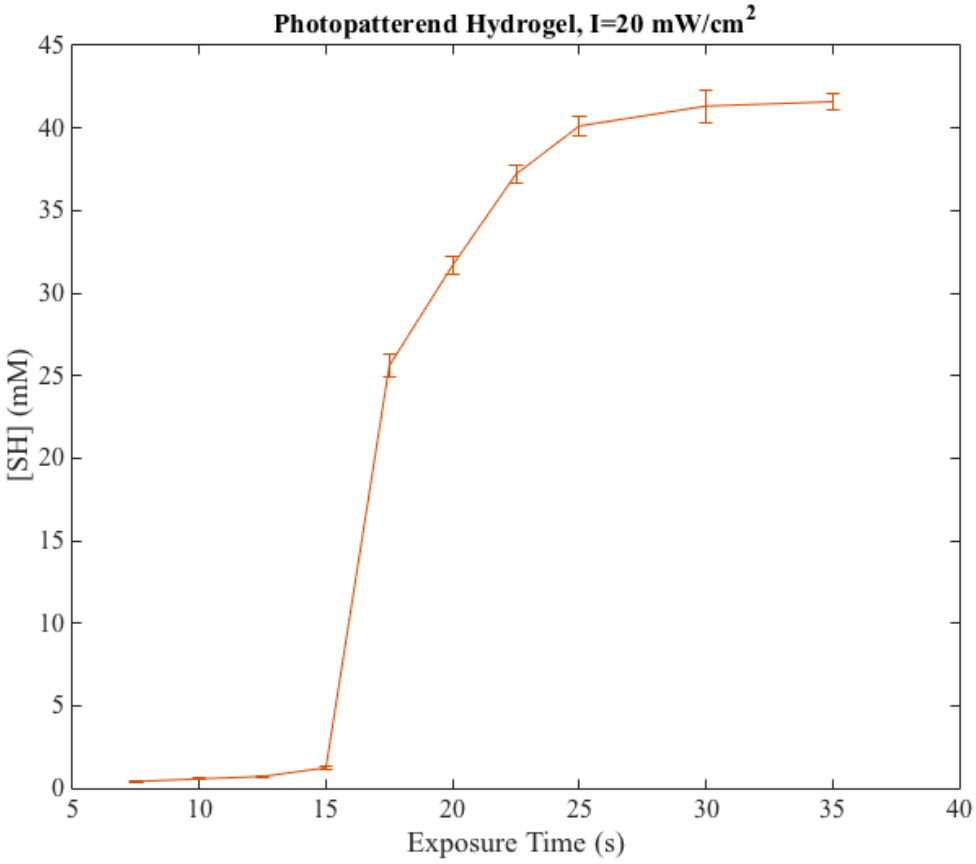


**Figure 5.14** Plot depicting the average thiol concentration (mM) at the center of a series of squares in the grid photopattern versus exposure time (s) with the one standard deviation plotted (n=20).

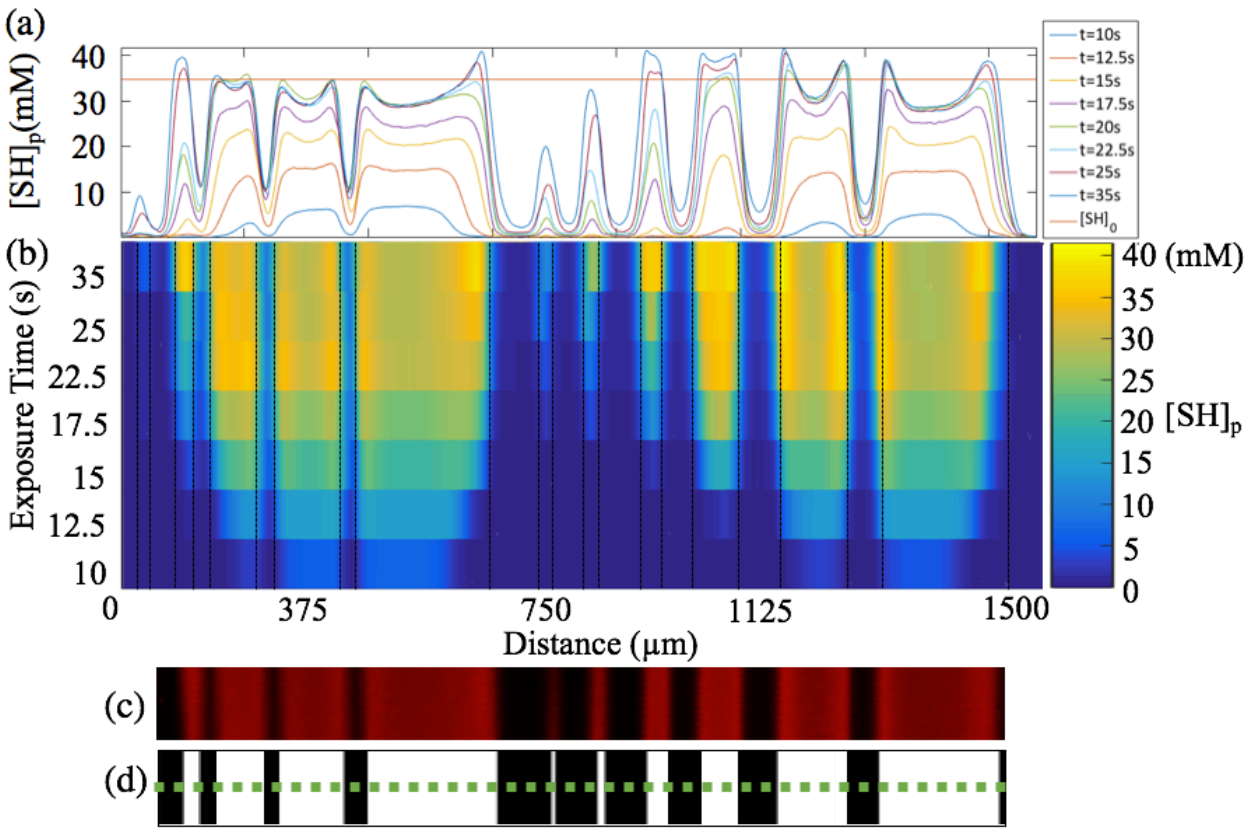


**Figure 5.15** (a) Attached thiol concentration as a function of exposure time. The orange line represents the initial concentration of thiol in the precursor solution. (b) Heat-map displaying increasing thiol concentration (yellow= high, blue=low) as a function of exposure time and distance across the photopattern. (c) Florescence image of hydrogel after a 22.5 s exposure to the (d) bitmap photopattern with the green dashed line indicating the where the fluorescence profile was taken for (a) and (b).

Hydrogels photopatterned with the resolution bitmap exhibit the three features modeled and observed in the one-dimensional characterization in the previous section (**Figure 5.15)**. Feature I, $[SH]_p > [SH]_0$ develops after $t_{exp}$ = 12.5s, indicating the time at which significant depletion of thiol monomer occurred within the photopattern to drive diffusion of fresh monomer into the illuminated region (**Figure 5.15**a-b). Feature II, rapid decrease in thiol concentration beyond the illuminated photopattern edge, becomes apparent after $t_{exp}$ = 17.5s where the pixels begin to be visible at the center of the photopattern, indicated by the smallest pattern, width 6 (**Figure 5.15**b).

Feature III, the movement of the enhanced thiol concentration edge, occurs almost immediately where at $t_{exp}$ = 10s the thiol attaches considerably inside of the intensity width (>30 μm at outermost photopattern edge), but thiol attachment at the outermost pattern edge is

negligible beyond ~50 nm (**Figure 5.15**a-b). If this feature development was due to thiyl radical diffusion out of this micron-scale region, an equal concentration of attached thiol would be visible at a similar length scale, which is not observed and is predicted from Feature II. Therefore, this edge movement is caused by differential swelling due to the equilibrium swelling ratio changing as a function of increase thiol concentration, as observed in the one-dimensional studies. The largest line-widths (1 and 2) are less able to be swollen due to the higher thiol concentration and thus crosslinking density and thus contract, effectively causing nearby features to appear to move closer to them (**Figure 5.15**b, $t_{exp}$ = 10, 12.5, 15, and 17.5 s). Because the thiol concentration profile was taken through the center of the photopattern, enhanced concentration at the pattern edges is due to unexposed monomer between the widths diffusing into the pattern. Thus, the features appear to contract towards the photopattern center occurs only until the unexposed monomer in between the widths is depleted, as evident after 20s between the largest widths and at 35s for the smaller widths (**Figure 5.15**b). The relationship between maximum thiol concentration, photopattern differential swelling, and the size and proximity of photopattern can be exploited to fully control the spatial distribution of thiol concentration and thus mechanical properties, though more experiments are required to adequately do so.

### *5.4.3 Atomic Force Microscopy*

Atomic force microscopy was then used to determine the elastic modulus across the hydrogels photopatterned with the resolution bitmap to understand at what exposure time and to what magnitude does the modulus increase develop, which was then compared to the predicted modulus using the model presented in Section 5.3.5. Increased thiol concentration is hypothesized to lead to increased elastic modulus. To test this hypothesis, photopatterns exposed for 15, 20, 25, and 35 seconds were probed using AFM to map the material response to varied exposure times. The expected modulus was calculated from the confocal fluorescence data (**Figure 5.15**) and the bulk studies (**Figure 4.6**) and was then plotted against the experimentally determined modulus of each sample.

The photopatterned modulus increase for a 15s exposure was significant for the largest photopattern widths (100-150% increase), though the smallest features do not show significant increases, as anticipated by the minimal thiol concentration present in these regions (**Figure**

**5.16**). The theoretical, expected modulus increase given the concentration of thiols present in the hydrogel was ~2X greater than the modulus measured (**Figure 5.16**). However, the model operates under the assumption that all species are in macromer, un-polymerized form, thus allowing for uniform conversion all species as demonstrated by previous studies using thiol:norbornene reactions.[17] Because the hydrogel is initially a crosslinked network with an ~50% excess norbornene concentration with additional crosslinks formed only after the network is swollen with new species and polymerized, is realistic for the modulus to be lower than the model. The model does not predict for sterically hindered species that become immobilized in the photopatterning process, which can lead to an artificially high modulus increase. The model does qualitatively predict the shape and approximate magnitude of the photopatterned features.

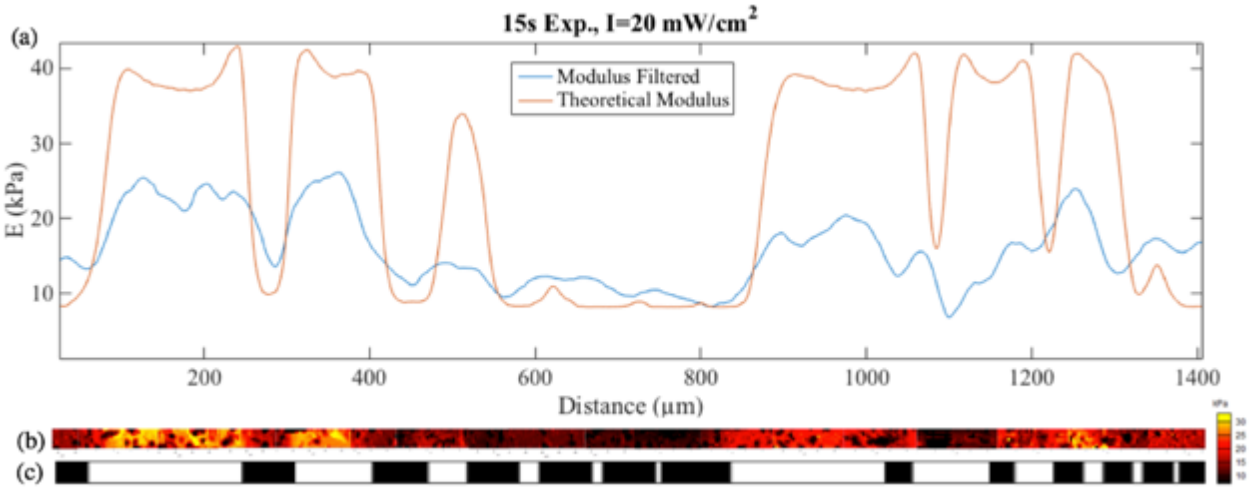


**Figure 5.16** (a) Graph depicting the (left) elastic modulus (kPa) of the photopatterned hydrogel ($t_{exp}$ =15 seconds, I=20 mW/cm$^2$) filtered data (Savitsky-Golay), with (right) the thiol concentration profile overlaid to highlight the enhanced modulus locations. (b) Image of the stitched AFM elastic modulus data, where yellow indicates enhanced modulus and black lower modulus, and (c) is a section of the projected photopattern bitmap to further emphasize enhanced modulus location.

Similarly, hydrogels photopatterned for 20s exhibited an increased modulus that matches the exposure pattern with all patterned regions translating into an increased modulus (**Figure 5.17**). While the modulus, again, falls below that of the model, the initial condition assumptions bias the model to over predict the modulus because the attached fluorophore does not function as a crosslinking agent and solely binds to a single site. However, the fluorescence concentration with respect to total thiol functional groups was kept sufficiently low to not influence

crosslinking. The presence of increased modulus at the edges of Feature 1-1 are the first appearance of the diffusion/reaction or Zhao-Mouroulis 'horns' translating directing into increased elastic modulus. The model qualitatively predicts the increased modulus with increased thiol concentration, capturing both the modulus of each photopatterned region and the enhanced modulus at the pattern edges (**Figure 5.17**).

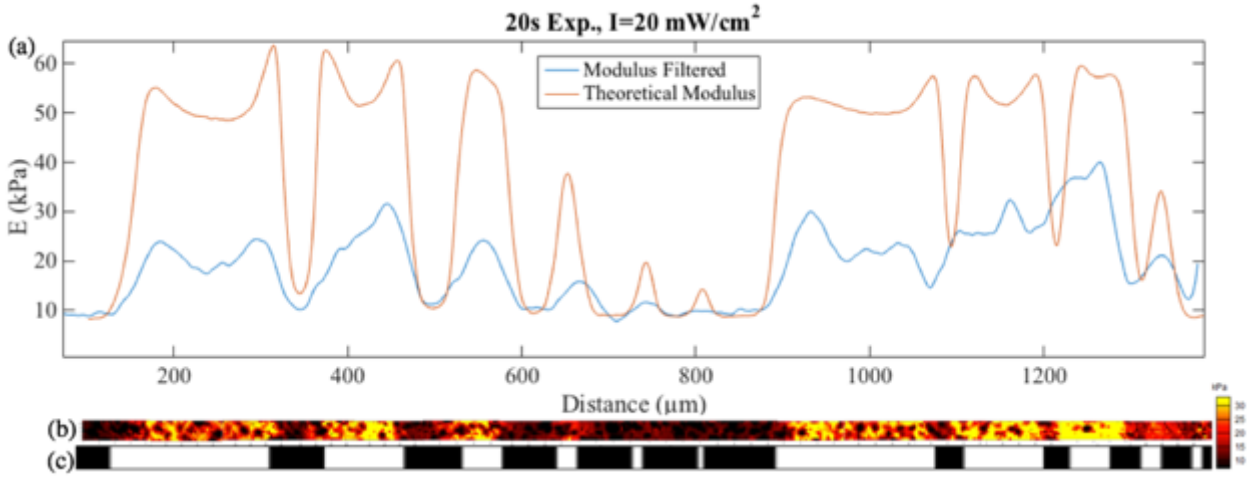


**Figure 5.17** (a) Graph depicting the (left) elastic modulus (kPa) of the photopatterned hydrogel ($t_{exp}$ =20 seconds, I=20 mW/cm$^2$) filtered data (Savitsky-Golay), with (right) the thiol concentration profile overlaid to highlight the enhanced modulus locations. (b) Image of the stitched AFM elastic modulus data, where yellow indicates enhanced modulus and black lower modulus, and (c) is a section of the projected photopattern bitmap to further emphasize enhanced modulus location.

Hydrogels photopatterned for 25s have an elastic modulus that maps directly to the exposed photopattern and matches the theoretical modulus both in shape and in magnitude for 9 of the 11 patterns (**Figure 5.18**). Longer exposure times allow sufficient time for not only the thiol component to diffuse into the photopattern region, but also the norbornene monomer because the larger, norbornene monomers diffuse at a slower rate than the thiol monomers. This generates an increased concentration of binding sites to which sterically hindered thiol react and, thus, form a higher modulus network than samples exposed for shorter times with low concentrations of diffused norbornene monomer. This result demonstrates the ability to locally increase the elastic modulus of low-solids-content hydrogels by five times using a single swelling and photopatterning cycle.

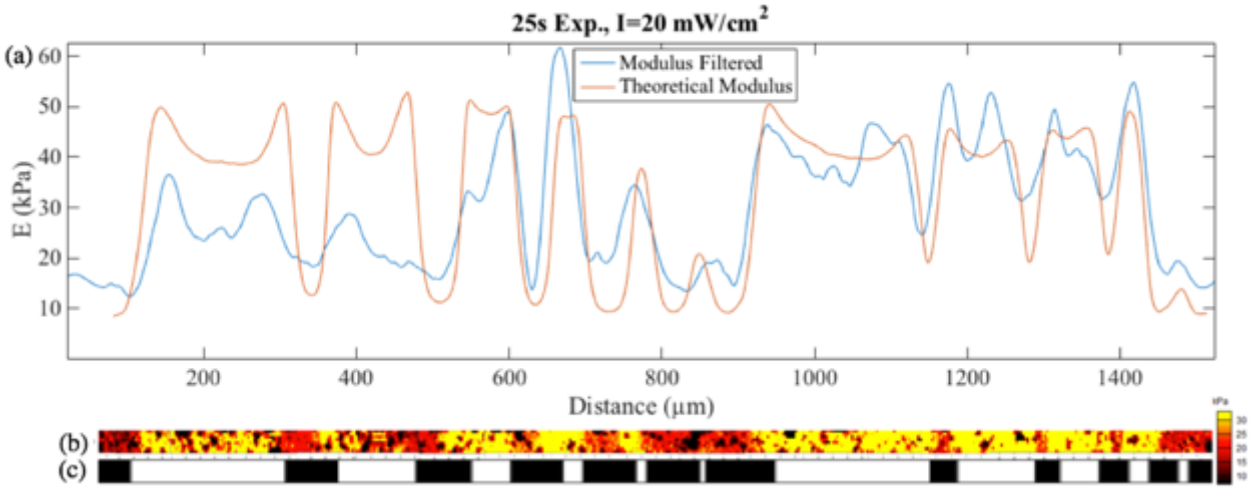


**Figure 5.18** (a) Graph depicting the (left) elastic modulus (kPa) of the photopatterned hydrogel ($t_{exp}$ =25 seconds, I=20 mW/cm$^2$) filtered data (Savitsky-Golay), with (right) the thiol concentration profile overlaid to highlight the enhanced modulus locations. (b) Image of the stitched AFM elastic modulus data, where yellow indicates enhanced modulus and black lower modulus, and (c) is a section of the projected photopattern bitmap to further emphasize enhanced modulus location.

Hydrogels patterned for 35s and tested using AFM had elastic modulus that followed the photopatterned exposure, but in this case, because the sample was exposed for a long duration, species had sufficient time to diffuse into the depleted regions between the features. It is hypothesized that these species then react with radicals that diffused outside of the photopattern due to diminished binding sites, effectively raising the baseline modulus for the sample, reducing the contrast between the exposed and unexposed photopattern regions (**Figure 5.19**). The model was not designed to accommodate for this unique situation and therefore does not predict the decreased contrast between photopatterned features that was measured. The reaction-diffusion features remain and contribute into increased elastic modulus at the edges of the larger photopatterns (**Figure 5.19**).

This is the first demonstration of locally enhanced elastic modulus in hydrogels using a single photopatterned precursor solution. Increased modulus is also detected down to the minimum photopattern feature width of ~10 μm. The optimal feature separation and width to photopattern features with the highest contrast in modulus at both feature edges is 26 μm feature size separated by 78 μm and exposed for 25s, which exhibited a 500% elastic modulus increase.

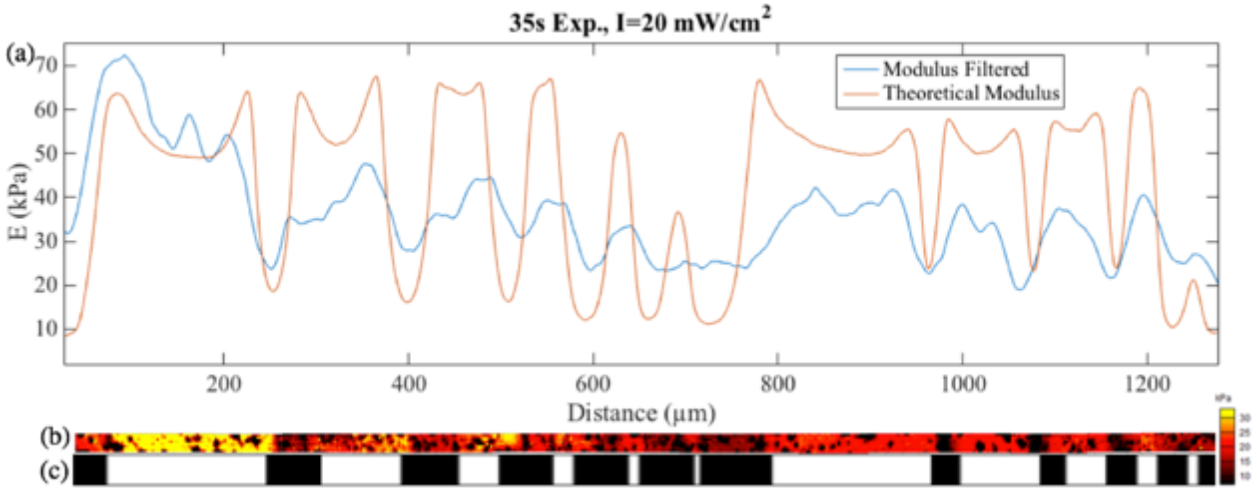


**Figure 5.19** (a) Graph depicting the (left) elastic modulus (kPa) of the photopatterned hydrogel ($t_{exp}$ =35 seconds, I=20 mW/cm$^2$) filtered data (Savitsky-Golay), with (right) the thiol concentration profile overlaid to highlight the enhanced modulus locations. (b) Image of the stitched AFM elastic modulus data, where yellow indicates enhanced modulus and black lower modulus, and (c) is a section of the projected photopattern bitmap to further emphasize enhanced modulus location.

The surface variability for each sample is depicted in the force-curve maps shown in **Figure 5.16**b-**Figure 5.19**b, where the dark, randomly arranged spots correspond to small surface contaminants on the photopattern surface that do not represent the true patterned modulus. Minimizing these contaminants by washing the sample prior to testing using purified de-ionized water is the subject of future work.

The topographic features of the sample were also probed using Contact Mode AFM. **Figure 5.20** displays the feature topography in reference to the photopattern and fluorescent image of the sample. The topographic image indicates a correlation between feature separation and photopattern swelling, which translates into feature height. Due to the translation of the bitmap pixels to the DMD, the spacing between features 1:2 and 3:4 in the left pattern set and features 4:5 on the right pattern set have roughly equivalent spacing (~60 μm). Between these patterns, a buckling effect was observed, which is represented by a 20% depression at the photopattern edges (with respect to the patterned region height) followed by a large bulge (~25 μm) centered between the patterns. For the photopatterns with the largest spacing (78μm), no increased height was observed between the patterned regions, whereas the 39μm spaced features (1:2 (left set), and 2:3 and 3:4 (right set)) resulted in a 20% height increase (**Figure 5.20**). It is

hypothesized that the differential swelling that occurs in these low solids content hydrogels causes the varied topography measured and is the subject of future work.

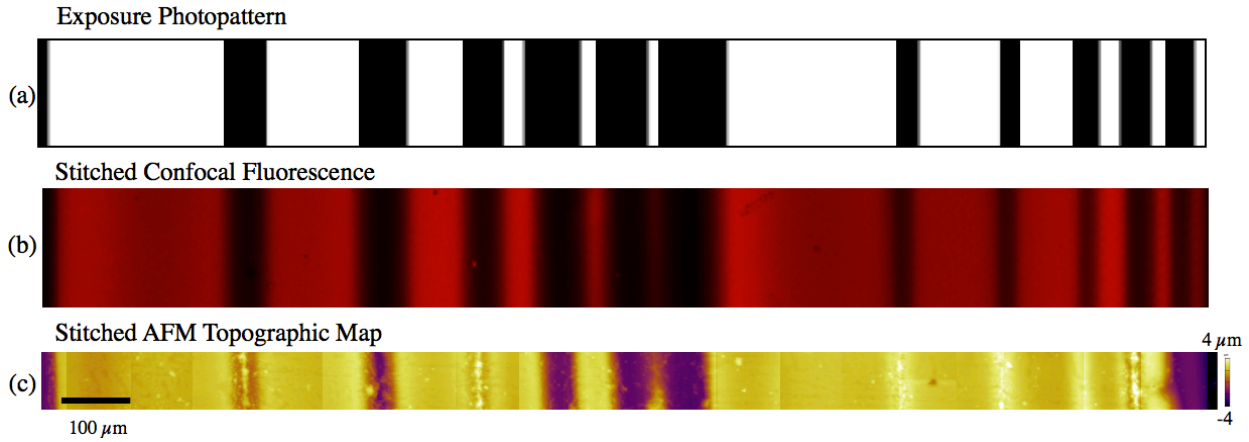


**Figure 5.20** (a) Segment of the bitmap photopattern that was used to photopattern the (b) hydrogel imaged using confocal fluorescent microscopy. Where (c) displays a stitched, topography image of the shown photopatterned hydrogel, where white indicates the highest regions and dark the lowest, resulting in a total height variation of 12 μm.

## 5.5 Conclusion

This chapter presented photopatterned hydrogels with locally enhanced mechanical properties using a single precursor solution formulation. A quantitative confocal fluorescence microscopy technique was developed to determine local measurement of attached thiol concentration across a photopattern and was applied to samples illuminated with variable intensity and exposure times. Photopatterning dynamics were first characterized in one dimension by exposing the swollen hydrogel to a single, rectangular photopattern.

Three distinct features were observed in the thiol concentration distribution: (I) $[SH]_p > [SH]_0$, (II) negligible [SH] ~50 nm beyond the photopattern edge, and (III) the enhanced [SH] at the photopattern edge is shifted inside of the photopattern edge. Feature I was hypothesized to be caused by diffusion of thiol monomer into the photopattern during polymerization. Feature II was hypothesized to be caused by the short distance thiyl radicals can diffuse before terminating on the $10^3$ times greater concentration of unreacted monomer outside of the photopattern. Feature III was hypothesized to be caused by reaction-induced differential swelling that occurs when the hydrogel becomes more crosslinked causing the equilibrium swelling ratio to change. These data

were then compared to the models presented in Chapter 3 to predict the concentration of attached species and differential swelling across the photopattern as a function of exposure time and intensity. This comparison agreed with all three hypotheses regarding the physical cause of each Feature, which informs future work fabricating fully-defined photopatterned hydrogels structures.

Hydrogel photopatterning was then probed in two dimensions using a resolution pattern to probe both the critical dimension and the resolution of the hydrogel patterning system and a grid pattern probed the interaction between closely patterned, repeating features. The three Features observed in the one-dimensional analysis were observed in these two-dimensional patterns. The short thiyl diffusion-reaction distance attributed to Feature II yielded high-fidelity photopatterns and provided the first demonstration of ~10 μm resolution photopatterning using an SLA system with low solids content solution (10 wt%) without the use of viscosifier or cytotoxic levels of photoinitiator.

Finally, combining the bulk properties measured in Chapter 4 with the known, printed species concentration, a model to predict the modulus across the photopattern was shown and compared to atomic force microscopy elastic modulus measurements across the photopatterned hydrogel. This comparison qualitatively validated the use of the predictive model and the single-precursor-solution technique to fabricate locally-defined, variable modulus hydrogels. This work demonstrates photopatterned hydrogels with 5X elastic modulus for ~30μm features, and presents this technique as a tool to characterize any photopatternable hydrogel material. SLA is a promising technique to fabricate variable modulus materials, and further research that probes a range of patternable biomaterials is the focus of future work.

## 5.6 References


1. Su, T. *et al.* Strong Bioinspired Polymer Hydrogel with Tunable Stiffness and Toughness for Mimicking the Extracellular Matrix. *ACS Macro Lett.* 1217–1221 (2016). doi:10.1021/acsmacrolett.6b00702

2. Engler, A. J., Sen, S., Sweeney, H. L. & Discher, D. E. Matrix elasticity directs stem cell lineage specification. *Cell* **126,** 677–89 (2006).

3. Oh, S. H., An, D. B., Kim, T. H. & Lee, J. H. Wide-range stiffness gradient PVA/HA hydrogel to investigate stem cell differentiation behavior. *Acta Biomater.* (2016). doi:10.1016/j.actbio.2016.02.016

4. Fairbanks, B. D. *et al.* A Versatile Synthetic Extracellular Matrix Mimic via Thiol-Norbornene Photopolymerization. *Adv. Mater.* **21,** 5005–10 (2009).

5. Ulrich, T. a., De Juan Pardo, E. M. & Kumar, S. The mechanical rigidity of the extracellular matrix regulates the structure, motility, and proliferation of glioma cells. *Cancer Res.* **69,** 4167–4174 (2009).

6. Extracellular matrix scaffolds for cartilage and bone regeneration. *Trends in Biotechnology* (2013). at <http://dx.doi.org/10.1016/j.tibtech.2012.12.004>

7. Wei L., H. *et al.* Biomaterial stiffness determines stem cell fate. *Life Sci.* (2017). doi:10.1016/j.lfs.2017.04.014

8. Binning, G., Rohrer, H., Gerber, C. & Weibel, E. Surface Studies by Scanning Tunneling Microscopy. *Treatises Mater. Sci. Technol. A. V. Granato* **49,** 505–33 (1958).

9. Binning, G., Gerber, C., Stoll, E., Atomic Resolution with Atomic Force Microscope. *Eur. Lett.* **12,** 1281–1286 (1987).

10. Le Grimellec, C. *et al.* Imaging of the Surface of Living Cells by Low-Force Contact-Mode Atomic Force Microscopy. *Biophys. J.* **75,** 695–703 (1998).

11. Butt, H.-J., Cappella, B. & Kappl, M. Force measurements with the atomic force microscope: Technique, interpretation and applications. *Surf. Sci. Rep.* **59,** 1–152 (2005).

12. Obataya, I., Nakamura, C., Han, S., Nakamura, N. & Miyake, J. Nanoscale Operation of a Living Cell Using an Atomic Force Microscope with a Nanoneedle. doi:10.1021/nl0485399

13. Savitzky, A. & Golay, M. J. E. Smoothing and Differentiation of Data by Simplified Least Squares Procedures. *Anal. Chem.* **36,** 1627–1639 (1964).

14. Zhao, G. & Mouroulis, P. Diffusion Model of Hologram Formation in Dry Photopolymer Materials. *J. Mod. Opt.* **41,** 1929–1939 (1994).

15. Aziz, A. H. *et al.* Mechanical characterization of sequentially layered photo-clickable thiol-ene hydrogels. *J. Mech. Behav. Biomed. Mater.* **65,** 454–465 (2017).

16. Skaalure, S. C. & Engineering, B. Tuning Hydrogel Degradation for Cartilage Tissue Engineering by. (2014).

17. Reddy, S. K., Cramer, N. B. & Bowman, C. N. Thiol−Vinyl Mechanisms. 1. Termination and Propagation Kinetics in Thiol−Ene Photopolymerizations. *Macromolecules* **39,** 3673–3680 (2006).

18. Cramer, N. B., Reddy, S. K., O'Brien, A. K. & Bowman, C. N. Thiol - Ene Photopolymerization Mechanism and Rate Limiting Step Changes for Various Vinyl Functional Group Chemistries. *Macromolecules* **36,** 7964–7969 (2003).

# Chapter 6 -Projection Stereolithography 3D Printed Hydrogels

## 6.1 Executive Summary

The models of Chapter 2 indicate that out-diffusion of thiyl or carbon-centered radicals into the surrounding monomer solution in the dark should have a transport distance well below a micron due to the high rate constant of the thiol-norbornene reaction. This suggests that it should be possible to 3D print high contrast thiol-norbornene hydrogel structures that would be impossible with acrylate or methacrylate monomers. This chapter presents the use of the thiol-norbornene hydrogel precursor material to form high-resolution (~10 μm) hydrogels with 250 μm, enclosed channels using the custom SLA projection printer presented in Chapter 2. This is the first demonstration of high-fidelity 3D printed hydrogels using high-water content (90%) precursor solution without the use of viscosifiers to decrease solute diffusivity. The 3D printed hydrogel channels were then perfused with dye to demonstrate their utility as a fully cytocompatible microfluidic device.

## 6.2 Introduction

Three-dimensional (3D) printing is a promising technology to recapitulate different biological tissues.[1,2] A common printing technique in regenerative medicine utilizes a nozzle-based deposition system where a 3D structure is built by depositing a steady flow of material onto the substrate, building up 2D cross sections of the desired structure. This allows multiple materials to be printed within a single structure, but because the material must be deposited through a nozzle, it places significant constraints on the types of materials that are printable. There are specifically three restrictive constraints that render it difficult to print a range of biologically relevant materials (*e.g.*, elastic moduli between 10 kPa and 10 MPa). The first constraint is the limited resolution caused by the minimum diameter of the deposition nozzle, where feature sizes below 10s μm are not printable.[3] The second constraint is that the material must be thixotropic, behaving as a fluid when a force is applied and then behaving as a solid once the force is removed, which considerably limits the types of materials printed.[4] The third constraint is that

the printing speed is, itself, defined by the printing material because cells will die if the applied force is too high (cell-line dependent), where cell-laden material cannot be deposited rapidly.[5]

Stereolithography (SLA) does not have the same limitations as nozzle-based systems. SLA offers the flexibility to fabricate variable modulus, cytocompatible structures using a single material through simple manipulation of the pattering process, which was demonstrated in previous chapters. SLA is currently utilized to fabricate a variety of tissue constructs ranging from bone-tissue regenerative medicine to fundamental research probing the development of individual muscle fibers.[6,7] Though the utility of the technique is demonstrated for a variety of regenerative medicine applications, it has yet to be widely adopted by the research community, primarily because of the difficulties involved with printing cytocompatible, hydrogel materials.

SLA 3D printing hydrogels is difficult due their high-diffusion (~10s-100 $\mu m^2/s$) and high water content (50-95%) that allow movement of species outside of and into the desired regions during the printing process[8–11]. Current research in 3D printed hydrogels using SLA demonstrates the ability to print a wide variety of cytocompatible materials, highlighting the utility of this technique.[1,12] Unfortunately, the structures presented are low resolution (100s μm) and do not provide evidence of overhanging features with resolution below 500 μm.[14–16,13,17,18] Current research only demonstrates the use of low solids content 10 wt% hydrogels with the use of a viscosifier, which can affect cellular development and viability by modifying the extracellular environement.[19–21]

As discussed in Chapter 2, another defining feature of 3D printing is fabricating overhanging structures. This is achieved in an SLA system by utilizing the absorptive properties of the printing material to prevent polymerization below the layer thickness.[22] However, because hydrogels allow material to readily diffuse, radical species (primary, monomers, oligomers, etc.) diffuse out of and into the exposure region during polymerization not only transversely, but also axially, into the previously fabricated layer. To print hydrogel overhanging structures with resolution greater than current research, both diffusion and absorption must be understood and subsequently applied.

Due to the high reactivity of thiol:norbornene reactions discussed and demonstrated in Chapters 5, high-fidelity, high-resolution (~10 μm) hydrogels were 3D printed using the SLA-AM system described in Chapter 2. In a first-of-kind demonstration, enclosed, perfusable channels were fabricated using low solids-content (10 wt%) hydrogel precursor solution without

the use of viscosifier. In addition to printing 3D low-solids-content hydrogel structures, 3D printed stiff hydrogel (~10 MPa) pillar structures are demonstrated with ~10μm resolution into which soft (10s kPa) hydrogel precursor solution was back-filled and polymerized. Printing both stiff hydrogel pillars to be back-filled and high-resolution, 10 wt% solids content hydrogels demonstrates the utility of SLA printing for a wide variety of future regenerative medicine applications.

## 6.3 Experimental Procedure

### *6.3.1 Materials*

Poly(ethylene glycol) dithiol (PEG-dithiol (Sigma Aldrich, MW 1,000 Da), poly(ethylene glycol) diacrylate (Sigma Aldrich, MW 700 Da), pentaerythritol tetrakis(3-mercaptopropionate) (PETMP, Sigma Aldrich), lithium phenyl-2,4,6-trimethylbenzoylphosphinate (LAP) (Colorado Photopolymer Solutions), fluorescent molecules AlexaFluor 546 and AlexaFluor 488 (Sigma Aldrich), Tinuvin CarboProtect (BASF), diphenyl(2,4,6-trimethylbenzoyl)phosphine oxide (TPO, Sigma Aldrich), and Trypan Blue (Sigma Aldrich) were used as received. 5-norbornene-2-carboxylic acid (NB) (Sigma Aldrich) was conjugated to poly(ethylene glycol) amine (PEG-$NH_2$) (JenKem USA, 8arm PEG amine, HCl salt, MW 10,000 Da) at room temperature (RT) under an argon purge to produce poly(ethylene glycol) norbornene (PEG-NB). [23] This was done by dissolving PEG-$NH_2$ (10 g) in dimethylformamide (DMF) (15mL) and dichloromethane at 1:1 ratio to which the solution containing 4-molar excess NB (4.42g), 2 molar excess 2-(1H-7-Azabenzotriazol-1-yl)-1,1,3,3-tetramethyl uronium hexafluorophosphate methanaminium (HATU, AKSci) (9.12g), and 2 molar excess N,N-diisopropylethylamine (DIEA, Sigma) (6.2 g) was reacted with for 48 hours. The solution was precipitated in diethyl ether, dialyzed four times with di$H_2O$ over two days, and lyophilized. The resulting 8-arm PEG-NB product conjugation of 99% (percentage of NB conjugated PEG arms), referred to herein as PEG-NB. The degree of norbornene conjugation was determined by $^1$HNMR (Bruker AV-III 400) by comparing the area under the peak for the allylic hydrogen closest to the norbornene bridged cyclic hydrocarbon group (resonance from ~3.1 to 3.2 ppm) to the area under the peak for the methyl groups in the PEG backbone (resonance from ~3.4 to 3.85 ppm), see Figure 4.6 for $^1$HNMR spectrum. Macromers were dissolved in phosphate-buffered saline (PBS) (OmniPur, Calbiochem).

### *6.3.2 Sample Preparation*

The 3D printing precursor solution was synthesized by combining 8.55 wt% 10kDa PEG-NB by mass to phosphate buffered saline and allowed to mix overnight at 3 degrees C. The thiol fluorescent tag, AlexaFluor 546, was reacted with PEG-dithiol overnight at 3 degrees C in a 1:3000 functional group ratio, which ensured the fluorescent tag did not affect the final material properties significantly. Immediately prior to photopolymerization, 1.45 wt% 1kDa PEG-dithiol was added to the NB solution with 0.05 wt% LAP and 2 wt% Tinuvin CarboProtect (CP) to produce an effective 10 wt% macromer concentration. The photoabsorber, Tinuvin CP, was added in 2 wt% to ensure polymerization beyond the 20μm layer thickness was negligible and thus allowed overhanging structures to be fabricated (**Figure 6.1**).

The stiff hydrogel precursor solution consisted of 99.95 wt% PEGDA, 1 wt% PETMP, and 0.05 wt% TPO photoinitiator, an equivalent initiator to LAP miscible in PEGDA, to which 0.1 mM AlexaFluor 546 was added that readily conjugates to PETMP under ambient conditions at room temperature. The hydrogel for back-filling the stiff structures was the same formulation as the 3D printed 10wt% PEG-thiol-ene hydrogel, except the fluorescent tag AF 488 was used in place of AF 546 to provide distinct contrast from the stiff structure AF 546 fluorescence. The stiff hydrogel precursor solution consisted of 99.95 wt% PEGDA, 1 wt% PETMP, and 0.05 wt% TPO photoinitiator, an equivalent initiator to LAP miscible in PEGDA, to which 0.1 mM AlexaFluor 546 was added that readily conjugates to PETMP under ambient conditions at room temperature. The hydrogel for back-filling the stiff structures was the same formulation as the 3D printed 10wt% PEG-thiol-ene hydrogel, except the fluorescent tag AF 488 was used in place of AF 546 to provide distinct contrast from the stiff structure AF 546 fluorescence.

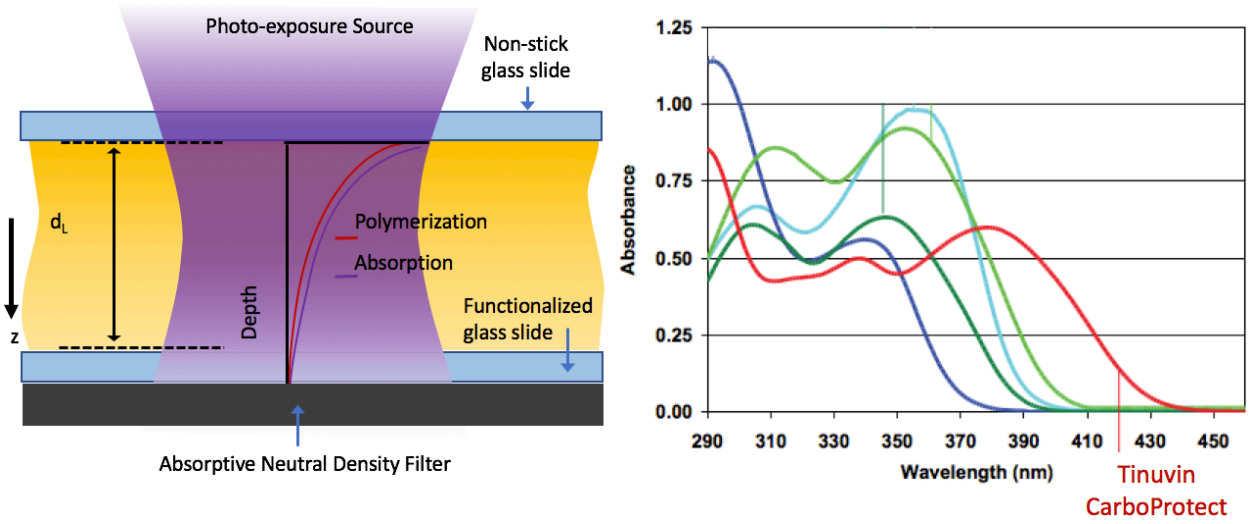


**Figure 6.1** (Left) Depiction of the photoexposure process demonstrating the decrease in polymerization as a function of depth due to absorption change in depth. (Right) Photoabsorber Tinuvin CarboProtect absorption spectrum, indicating it is relevant for SLA printing at 400 nm.[24]

Because both the photoinitiator and the fluorescent tag are sensitive to ambient, white light, all solution preparation, printing, post-processing, and sample storage was done under >500 nm wavelength lighting. All 3D structures were fabricated using the SLA system described in 0 2 with a methacrylate-functionalized glass microscope slide substrate (Cell) to ensure the structure polymerized to the substrate. RainX was applied to the photopatterning window to prevent sample/window adhesion. Once both substrate and window were in place, a small volume (20-30 µL) of precursor solution (for either the stiff or soft hydrogels) was deposited onto the sample substrate. The sample was translated vertically until it was ~50-100 µm from the window surface (**Figure 6.2**). This distance served as a baseline from which the structures, with user-defined layer thicknesses, were built. As mentioned, the 3D printed soft, thiol-ene hydrogel structures were printed using a 20 µm layer thickness, to produce a total structure height of 1.5 mm tall (75 layers). The stiff PEGDA hydrogel structures were printed using a 50 µm layer thickness, with a total height of 300 µm (6 layers). Because the stiff hydrogel structures did not require overhanging features, no photo-absorber was used in the precursor formulation.

The soft 3D printed hydrogels were placed into a bath of DI water for 24 hrs to allow all unreacted macromer to diffuse out of the structure. The stiff hydrogels were also placed into a bath to remove unreacted material, but because PEGDA 700 is immiscible in water, it was placed into a bath of pure ethanol for 24 hrs. Each structure was then removed from the bath

containing unreacted material, placed into a fresh bath of DI water, and allowed to swell to equilibrium for 24 hr prior to further processing and/or structure characterization. To probe the ability to back-fill stiff hydrogel structures, the equilibrium swollen PEGDA structures were back-filled with the soft, 10 wt% thiol:norbornene hydrogel precursor solution and then polymerized (**Figure 6.2**).

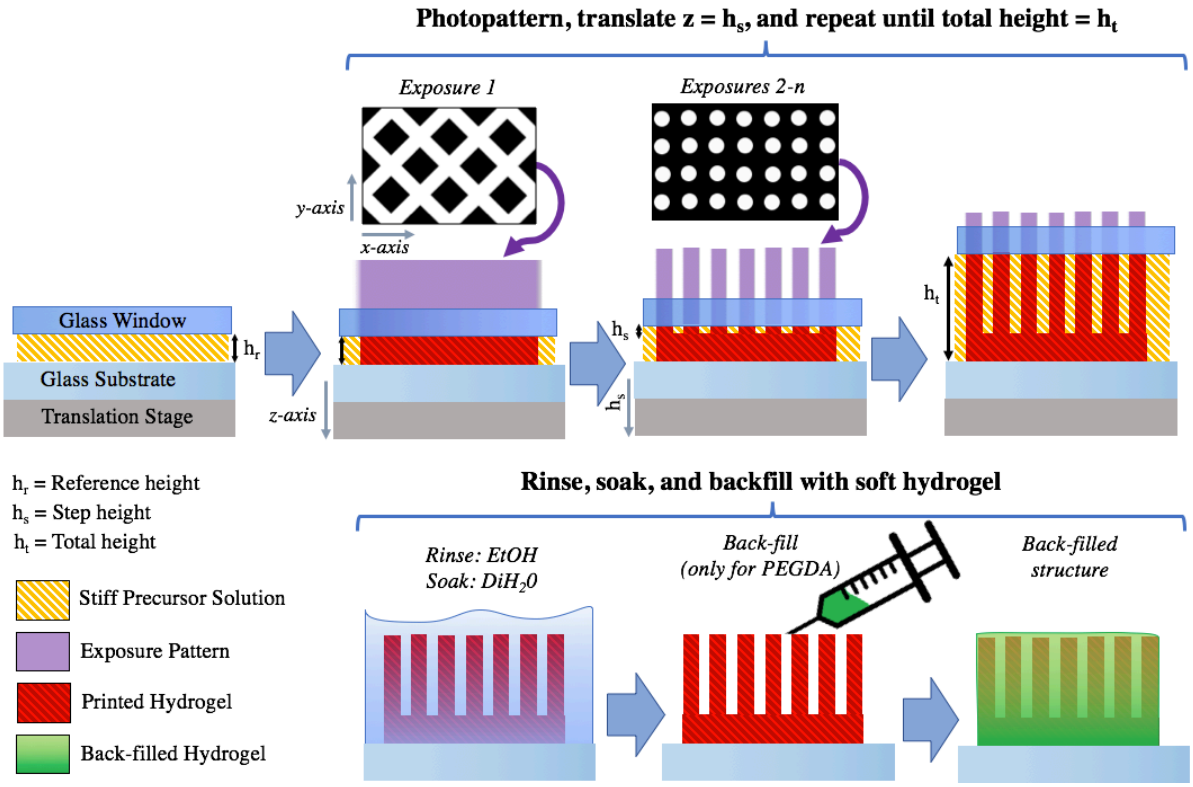


**Figure 6.2** Sample preparation process for photopatterned hydrogel (pillar photo-exposure patterns shown). Soft 3D printed hydrogels follow the same procedure as stiff, excluding the additional back-filling procedure.

### *6.3.3 Confocal fluorescence microscopy*

As discussed in Chapter 5, the samples were imaged using fluorescence confocal microscopy with a 10X water immersion objective. Because the microscope image size at 10X was much smaller than the total structure size, 30 images were taken and then stitched together to produce a complete, 2D cross-section image of the printed hydrogel structures. The structure was also imaged in depth by taking a series of images at 10 µm increments to generate a 3D fluorescent image of the printed structure because confocal microscopy allows only light collected at the focal place to reach the photo-detector.

*6.3.4 Channel Perfusion*

To demonstrate the ability to fabricate soft hydrogel structures with overhanging features, Trypan Blue dye was pipetted into the 3D photopatterned hydrogel structure. To optically monitor the perfusion of dye through the printed hydrogel channels, both a Dino-Lite Digital Microscope (Dino-Lite) and an 8-megapixel iSight camera (Macintosh) were used. Both features with and without overhangs were captured to demonstrate the comparative differences between the two structures.

## 6.4 Results and Discussion

*6.4.1 3D printed soft, 10 wt% PEG hydrogels*

High-fidelity 3D printed soft (~10 kPa), 10wt% PEG hydrogels with 250 μm enclosed channels were printed using the SLA-AM system with ~10 μm resolution (**Figure 6.3**). The fluorescent region indicates photopatterned hydrogel and the enclosed channels are the connected letters CU, where slight fluorescence is visible between the channels due to fluorescence from the 100 μm hydrogel ceiling encasing the channels. As discussed in Chapter 5, the enhanced fluorescence at photopattern edges indicates diffusion occurring during polymerization. This effect is present in the confocal fluorescence images taken of the University of Colorado (CU) Buffalo. Due to the fast reaction rate of thiol:norbornene hydrogels, species diffusing into the photopattern react within the photopatterned region before they can diffuse out. This allows 10 wt% precursor solution to be SLA 3D printed with pixel-limited resolution, which is observed **Figure 6.3** inset image, where characteristic diamond DMD pixel edges are visible. This result highlights the importance of precursor solution choice because the rate of polymerization greatly affects the final structure resolution (*i.e.,* fast thiol:norbornene reaction chemistry enables finely resolved features).

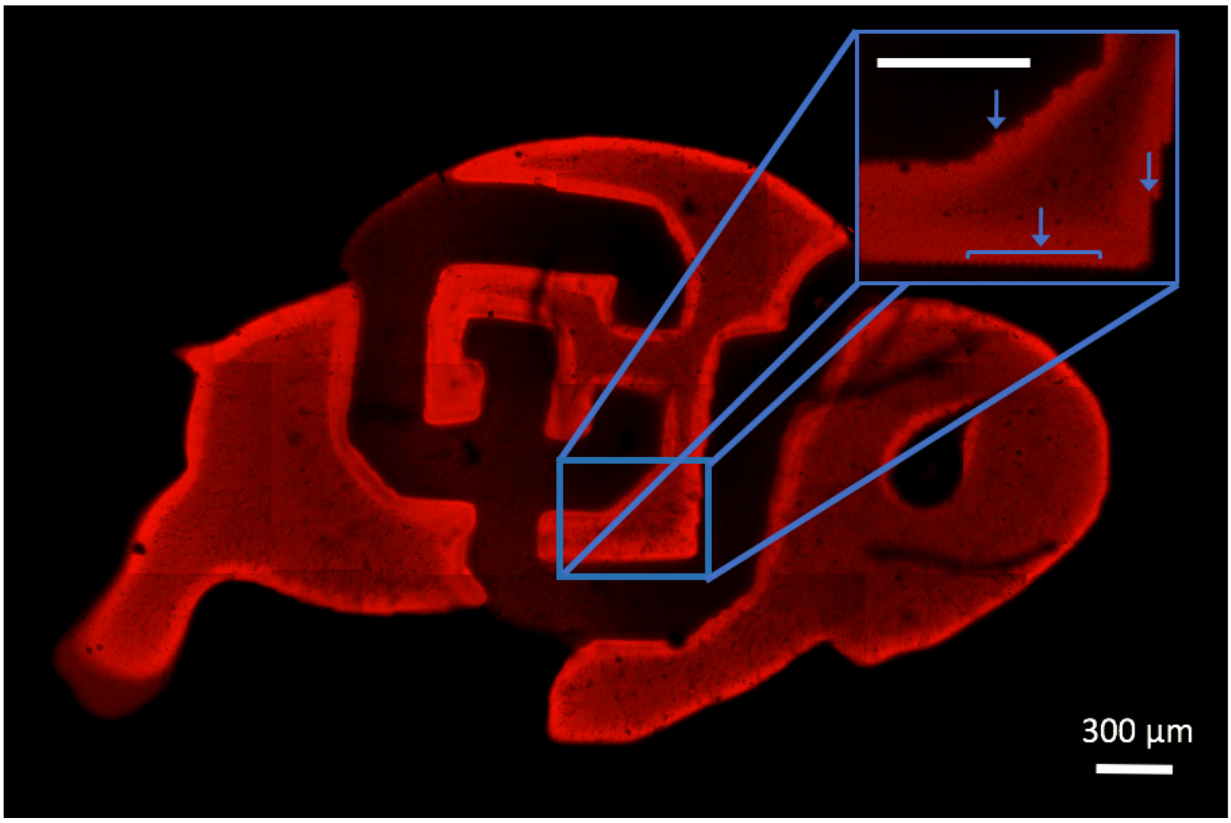


**Figure 6.3** 3D printed PEG hydrogel with visible, encased channels indicated slight fluorescent shading over the CU and (inset) visible DMD pixels photopatterned into the 3D structure, with arrows highlighting the distinguishable pixels.

To further verify the presence of encased channels beyond the confocal fluorescence images, Trypan Blue was perfused through the CU Buffalo channels. Taken as a time-lapse image series, the dye is injected at a rate of ~5 µL/s beneath the buffalo at t=0s after which it takes 2.05s for the dye to perfuse the length of all channel. The dye rapidly (~0.3s) traverses through the path of least resistance, through the edge of the C-U channel, and then slowly diffuses into the remainder of the C-U channels, which required an additional 1.75 seconds to completely perfuse (**Figure 6.4**). The rate of perfusion variation is because perfusion of liquid through an enclosed, no-outlet channel (*e.g.,* the ends of the 'C') is less energetically favorable than perfusion through channels with an outlet (*e.g.,* the bottom edge of the 'U').[25]

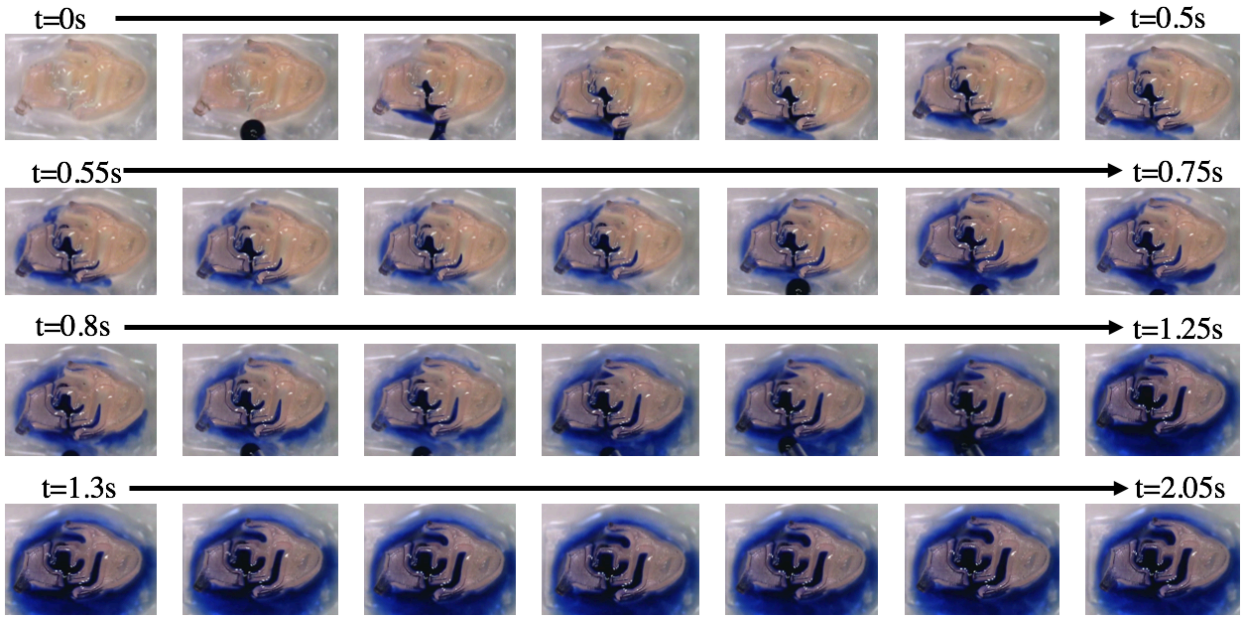


Figure 6.4 Perfusion of Trypan Blue dye through a 3D printed PEG hydrogel CU Buffalo with channels, snapshots taken from Dino-Lite video footage. Full perfusion of Trypan Blue dye requires 2.05s to travel through the 250μm width channels.

Comparing the un-perfused hydrogel channels to the final, perfused channels further verifies of the presence of a thin, hydrogel layer encasing the C-U channel. At t=0, the channels have a concave surface curvature, as indicated by the surface reflections showing an offset between the channel edges and the channel center that is representative of a depressed feature (**Figure 6.5**).[26,27] Conversely, at t=2.05s, the channels are fully perfused and swollen, effectively causing the top surface of the hydrogel to bow outward or convexly, as indicated, again, by the surface reflections that are representative of a raised, convex feature (**Figure 6.5**).[26,27] Because the photopatterned C-U channel ceiling is ~100 μm thick and is fabricated using 10 wt% solids content hydrogel, it swells and shrinks rapidly (~2s), while thick (~500 μm) and/or higher crosslinking density channel ceilings do not experience the same deflection.[15] Additionally, the dye used does diffuse into the PEG-NB-thiol hydrogel, as shown in the buffalo rear, left 'foot', but because it occurs at a slower rate than the time required to observe full perfusion, it is negligible (**Figure 6.4**).

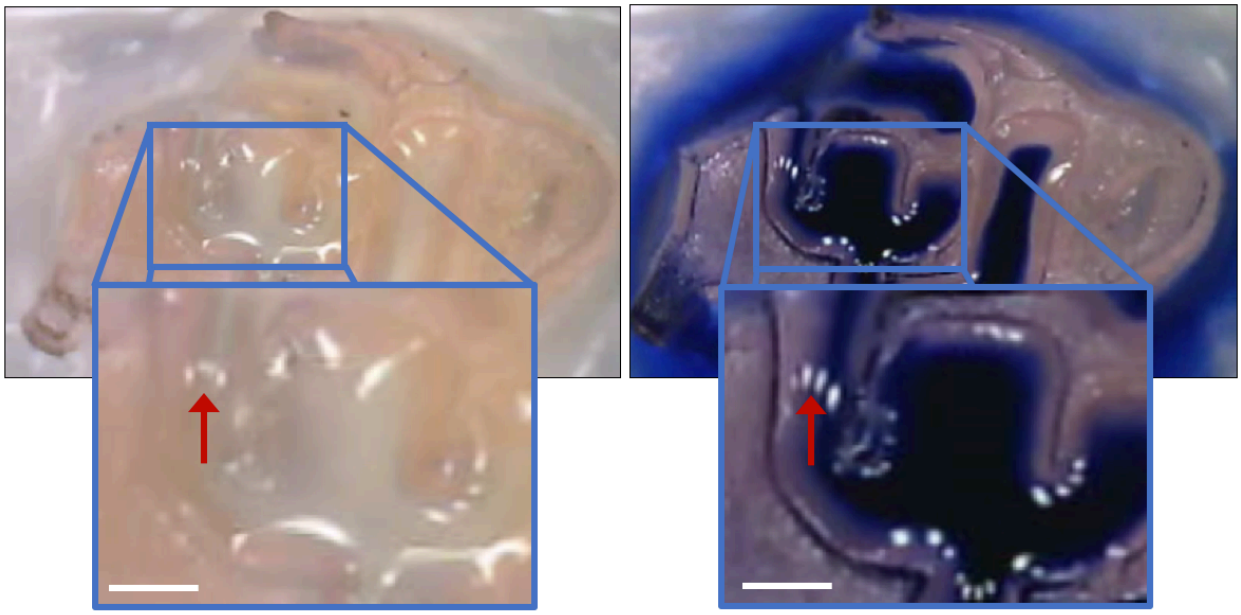

**Figure 6.5** Image demonstrating the deflection of the enclosed channel, where the left image, taken at t=0s, shows the channel ceiling in a concave conformation indicated by the concave surface reflections (red arrow). The right image is taken at t=2.05s where the ceiling is convex, as indicated by the convex surface reflections (red arrow). The scale bar indicates 250 µm.

To probe how channel perfusion is affected by the presence of a channel ceiling, the same CU Buffalo channels were printed (20µm layers, 1.5 mm tall) without an encasing ceiling. Keeping all perfusion conditions constant (*i.e.*, solution=Trypan Blue, velocity = ~5µL/s) channels printed without a ceiling perfused four times faster than those with encased channels (**Figure 6.6**). A possible explanation for this significant difference is that open channels can replace any remaining DI water within the channels more rapidly than the enclosed channels because they do not have a barrier applying opposing pressure to the diffusing/perfusing solution (*i.e.*, ceiling concavity with perfusion). Patterning regions of enclosed channels versus open channels will enable precise control of perfusion velocity and is the subject of future work.

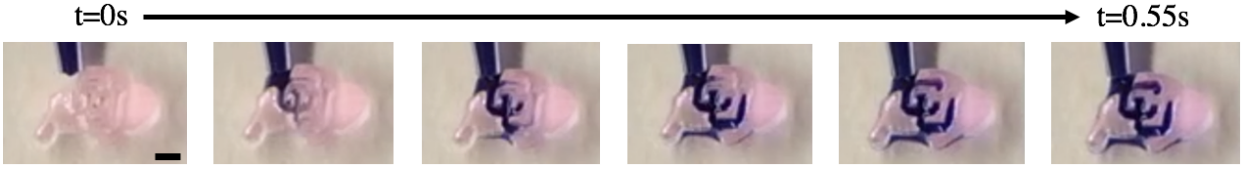


**Figure 6.6** Perfusion of Trypan Blue through 3D printed PEG hydrogel CU Buffalo without channel ceilings, snapshots taken from using iSight camera. Full perfusion through channels

required only 0.55s, a duration 4X shorter than that of enclosed channels. Scale bar equivalent to 500 μm.

SLA 3D printed 1.5mm tall 10 wt% hydrogel structures with pixel-limited resolution were made possible due to a non-stick, RainX window. No adhesion to the RainX window was observed for the soft, thiol-ene hydrogels. This is attributed to the high water, low solids content of the printing precursor solution that effectively reduces the surface area to fraction of the total print area (~10%), reducing adhesion between the patterned hydrogel and the window. Though the structures presented here required 75 layers, similar structures were printed with > 300 layers with no window failure observed.

*6.4.2 3D printed stiff PEGDA hydrogels*

3D printed stiff, PEGDA hydrogel pillars (diameter=100μm) were fabricated and then back-filled with soft, 10 wt% hydrogel, demonstrating the versatility of the SLA-AM patterning system (**Figure 6.7**). The final structure was ~400 μm tall with 6, 50 μm layers and an ~100 μm reference layer (lattice pattern shown in **Figure 6.2**) from which the pillars were built. Confocal images were taken before and after back-filling, where the non-backfilled structures are shown in red, and the soft, hydrogel structure is shown in green (**Figure 6.7**). The tilted view of the back-filled pillars is a view from the bottom/side of the structure, which demonstrates the ability to homogenously back-fill the printed hydrogel structures. The tilted view of the pillars without back-fill depict a view from the top/side of the structure, demonstrating pillar symmetry.

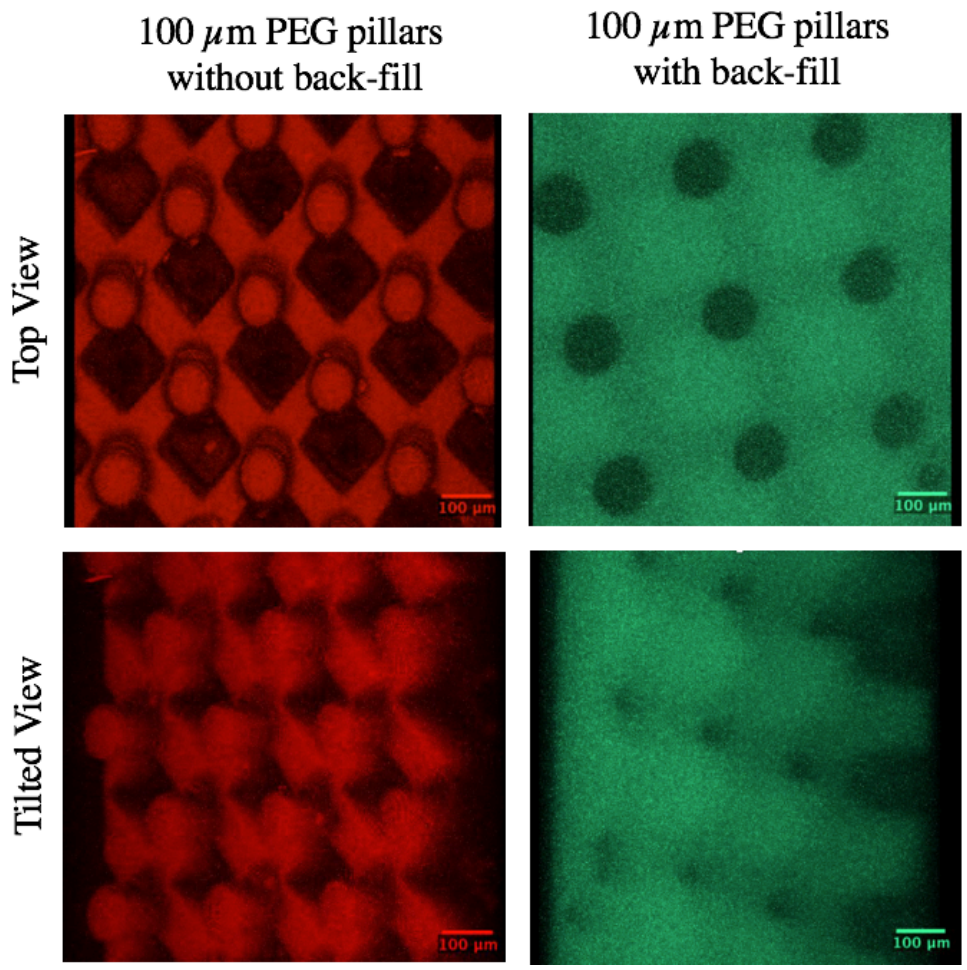


**Figure 6.7** (Left) Stiff 100 μm diameter PEGDA pillars with AF546-tagged thiol (top view and tilted view) and (right) the same pillars back-filled with 10 wt% PEG-NB-dithiol hydrogel with AF488 tagged thiol to demonstrate hydrogel back-filling capabilities.

Unlike the 10 wt% hydrogels, the stiff PEGDA structures did adhere to the nonstick RainX window after 7+ layers. This is attributed to the high solids content precursor solution, which allowed 100% of the print area to adhere to the window surface. With each patterned layer, the adhesive force between the structure and the window removed portions of the silane coating until, after 7 layers, the sample adhered to the surface due to low nonstick silane concentration. To overcome this issue, the subject of future work is a poly dimethyl siloxane (PDMS) window through which oxygen can diffuse into the precursor solution, inhibiting the polymerization reaction, which is demonstrated for similar applications.[28–30]

## 6.5 Conclusion

3D SLA printed structures were demonstrated with pixel-limited resolution (~10 μm) and overhanging features using a range of precursor solutions to produce elastic moduli hydrogels ranging from 10s kPa to 10s MPa. The encased 3D printed channels demonstrate the utility of this technique for regenerative medicine because it enables precise control of hydrogel physical and chemical properties, while maintaining a viable cellular environment. Because the hydrogels printed here are affected by local water concentration, perfused channel ceilings became bowed when they were fully perfused. This effect can be harnessed as a switching mechanism in 3D to control nutrients or drug delivery using a passive perfusion system to open and/or close the delivery channel. Conversely, this effect can be removed using precursor solution that produces a higher crosslinking density hydrogel, decreasing the swelling ratio, or by tuning the matrix chemistry to produce a network that is unaffected by local water concentration variations.

In addition, controlling the location of outlet ports and 'dead-ends' within the encased hydrogel network also provide a mechanism to control nutrients and/or drugs delivery at a pre-determined rate. By understanding the perfusion rate and diffusion rate of a given solution through the 3D printed hydrogel network, a channel-system can be designed to deliver solutions to a predefined site within the perfusion network at a predefined time. For these reasons, this is a powerful fabrication technique for regenerative medicine studies that require a pre-determined rate and precise location of drug and/or pathogen delivery, which is suggested future work.

## 6.6 References


1. Elomaa, L. *et al.* Three-dimensional fabrication of cell-laden biodegradable poly(ethylene glycol-co-depsipeptide) hydrogels by visible light stereolithography. *J. Mater. Chem. B* **3,** 8348–8358 (2015).

2. Bajaj, P., Schweller, R. M., Khademhosseini, A., West, J. L. & Bashir, R. 3D Biofabrication Strategies for Tissue Engineering and Regenerative Medicine. *Annu. Rev. Biomed. Eng.* **16,** 247–76 (2014).

3. Li, X., Lian, Q., Li, D., Xin, H. & Jia, S. Development of a Robotic Arm Based Hydrogel Additive Manufacturing System for In-Situ Printing. *Appl. Sci.* **7,** 73 (2017).

4. Hospodiuk, M., Dey, M., Sosnoski, D. & Ozbolat, I. T. The bioink: A comprehensive review on bioprintable materials. *Biotechnol. Adv.* (2017). doi:10.1016/j.biotechadv.2016.12.006

5. Murphy, S. V & Atala, A. 3D bioprinting of tissues and organs. *Nat. Biotechnol.* **32,** 773–785 (2014).

6. Cooke, M. N., Fisher, J. P., Dean, D., Rimnac, C. & Mikos, A. G. Use of stereolithography to manufacture critical-sized 3D biodegradable scaffolds for bone ingrowth. *J. Biomed. Mater. Res. B. Appl. Biomater.* **64,** 65–69 (2003).

7. Linnenberger, A. *et al.* Three dimensional live cell lithography. *Optics express* **21,** 10269–77 (2013).

8. Hadjiev, N. A. & Amsden, B. G. An assessment of the ability of the obstruction-scaling model to estimate solute diffusion coefficients in hydrogels. *J. Control. Release* **199,** 10–16 (2015).

9. Watkins, A. W. & Anseth, K. S. Investigation of molecular transport and distributions in poly(ethylene glycol) hydrogels with confocal laser scanning microscopy. *Macromolecules* **38,** 1326–1334 (2005).

10. Akalp, U. *et al.* Determination of the Polymer-Solvent Interaction Parameter for PEG Hydrogels in Water: Application of a Self Learning Algorithm. *Polymer (Guildf).* **66,** 135–147 (2015).

11. Skaalure, S. C. & Engineering, B. Tuning Hydrogel Degradation for Cartilage Tissue Engineering by. (2014).

12. Lambert, P. *et al.* Mask projection microsterolithography of novel biocompatible polymers. 2284 (2014).

13. Chan, V., Zorlutuna, P., Jeong, J. H., Kong, H. & Bashir, R. Three-dimensional photopatterning of hydrogels using stereolithography for long-term cell encapsulation. *Lab Chip* **10,** 2062–2070 (2010).

14. Sirrine, J. M. *et al.* 3D-Printable Biodegradable Polyester Tissue Scaffolds for Cell Adhesion. *Aust. J. Chem.* **68,** 1409 (2015).

15. Elomaa, L. *et al.* Three-dimensional fabrication of cell-laden biodegradable poly(ethylene glycol-co-depsipeptide) hydrogels by visible light stereolithography. *J. Mater. Chem. B* **3,** 8348–8358 (2015).

16. Arcaute, K., Mann, B. & Wicker, R. Stereolithography of spatially controlled multi-material bioactive poly(ethylene glycol) scaffolds. *Acta Biomater.* **6,** 1047–1054 (2010).

17. Zhou, X. *et al.* 3D bioprinted graphene oxide-incorporated matrix for promoting chondrogenic differentiation of human bone marrow mesenchymal stem cells. *Carbon N. Y.* (2017). doi:10.1016/j.carbon.2017.02.049

18. Lin, H. *et al.* Application of visible light-based projection stereolithography for live cell-scaffold fabrication with designed architecture. *Biomaterials* **34,** 331–339 (2013).

19. Cha, C. *et al.* Structural Reinforcement of Cell-Laden Hydrogels with Microfabricated Three Dimensional Scaffolds. *Biomater. Sci.* **2,** 703–709 (2014).

20. Bryant, S. J., Nuttelman, C. R. & Anseth, K. S. The effects of crosslinking density on cartilage formation in photocrosslinkable hydrogels. *Biomed. Sci. Instrum.* **35,** 309–14 (1999).

21. Weber, L. M., Lopez, C. G. & Anseth, K. S. Effects of PEG hydrogel crosslinking density on protein diffusion and encapsulated islet survival and function. *J. Biomed. Mater. Res. Part A* **90A,** 720–729 (2009).

22. Wang, Z. *et al.* A simple and high-resolution stereolithography-based 3D bioprinting system using visible light crosslinkable bioinks. *Biofabrication* **7,** (2015).

23. Roberts, J. J. & Bryant, S. J. Comparison of photopolymerizable thiol-ene PEG and acrylate-based PEG hydrogels for cartilage development. *Biomaterials* **34,** 9969–9979 (2013).

24. Tinuvin ® CarboProtect ®. at <http://aerospace.basf.com/common/pdfs/BASF_Tinuvin_CarboProtect_DS_USL_sfs.pdf>

25. Nguyen, N.-T. & Wereley, S. T. *Fundamentals and Applications of Microfluidics Second Edition*. (Artech House, 2006).

26. Kreimer, G. & Melkonian, M. Reflection confocal laser scanning microscopy of eyespots in flagellated green algae. *Eur. J. Cell Biol.* **53,** 101–11 (1990).

27. Kerrigan, I. S. *et al.* Highlights, disparity, and perceived gloss with convex and concave surfaces. *J. Vis.* **13,** 9–9 (2013).

28. Urness, A. C., Moore, E. D., Kamysiak, K. K., Cole, M. C. & Mcleod, R. R. Liquid deposition photolithography for submicrometer resolution three-dimensional index structuring with large throughput. *Light Sci. Appl.* **212,** (2013).

29. Janusziewicz, R., Tumbleston, J. R., Quintanilla, A. L., Mecham, S. J. & DeSimone, J. M. Layerless fabrication with continuous liquid interface production. *Proc. Natl. Acad. Sci. U. S. A.* 201605271 (2016). doi:10.1073/pnas.1605271113

30. Tumbleston, J. R. *et al.* Continuous liquid interface production of 3D objects. *Science (80-. ).* **347,** (2015).

# Chapter 7 - Conclusions and Recommendations

## 7.1 Conclusions

This thesis advances tissue engineering technologies by developing and characterizing a technique to fabricate cytocompatible hydrogel structures with locally defined mechanical and chemical properties. The current state of the art to fabricate tissue engineering constructs with spatially defined mechanical properties uses nozzle-based three-dimensional (3D) printing due to its ability to print with multiple materials.[1–3] However, the constraints on ink-jet 3D printing limit its use to include printing solely shear-thinning materials that are dispensed through a nozzle, which limits fabrication resolution to >10s μm. The printing throughput is also constrained because cell-laden precursor materials cannot be extruded at forces greater than the cells can sustain, which limits the speed of printing.[1] Stereolithography (SLA) does not have these restrictions and can exploit the diffusivity of low solids content cytocompatible hydrogels and photopolymerization to produce locally defined mechanical and chemical properties, which is demonstrated in Chapters 3-4.

Chapter 2 presents the fundamentals of SLA 3D printing, which demonstrates the complexity of photopatterning low solids content systems because diffusion can occur during photopolymerization. This diffusion and subsequent reaction can reduce photopattern fidelity if the chosen printing resin does not compensate for this effect. A custom SLA 3D printer was designed and built to enable cytocompatible materials to be photopatterned, which enabled all photopatterning work presented in this thesis.

Chapter 3 demonstrates the ability to fabricate hydrogels with variable mechanical properties using a single precursor solution, where over an order of magnitude increases in compressive modulus and toughness were achieved. This technique isolated diffusion/swelling transport kinetics from the photopolymerization kinetics by determining the hydrogel mechanical properties in bulk versus in the photopatterning environment. Although this method is demonstrated for a single photochemistry and macromer solution, it is readily applied to any precursor solution that is polymerizeable and can be diffused or swollen with new materials, which expands the utility of cytocompatible materials used in regenerative medicine.

The technique developed in Chapter 3 was applied to the custom SLA photopatterning system (Chapter 2), to photopattern hydrogels with locally enhanced elastic moduli in Chapter 4. A 500% increase in elastic modulus was demonstrated for ~26μm features using, again, a single precursor solution. The ability to pattern the local concentration of different chemical species (*i.e.*, thiol macromer), not only enabled photopatternable mechanical properties, but can extend to include photopatterning a range of chemical cues to probe cellular development.[4]

The photopatterning model presented in Chapter 5 advances the field of 3D printing cytocompatible materials by predicting the relationship between the complex photopatterning environment of low solids content, hydrogel materials and the final photopatterned structure fidelity. This work demonstrates the ability to predict, with 90% confidence, the width of diffusion-reaction features that enhance both mechanical properties and chemical concentrations at the edges of photopatterns. This model provides the framework to either exploit or remove these features when photopatterning low solids content hydrogels.

This work further advances the field of 3D printing by demonstrating, for the first time, SLA 3D printing of 10 wt% solids content hydrogel scaffolds with pixel-limited resolution (~10s μm) using a custom-built SLA printer (SLA-AM). The state of the art in printing hydrogels using SLA utilizes precursor solutions with >15wt% solids content with a maximum reported transverse resolution of ~100 μm with a minimum overhanging feature size of ~ 500 mm.[5–8] The ability to photopattern perfusable 10 wt% hydrogel networks with 250μm channel widths and ~10 μm resolution using a custom SLA system therefore extends considerably beyond the current state of the art.

### 7.2 Recommendations

The findings in this thesis demonstrate the importance of understanding the complex 3D photopatterning environment in hydrogel systems to fabrication fidelity and mechanical property control. This thesis provides the foundation for future SLA 3D printing of cytocompatible hydrogels by addressing the most significant factors when photopatterning low solids content hydrogels and using them to model the ability to print high fidelity hydrogel constructs with photopatterned mechanical properties. To build from this research the following studies are recommended.

### *7.2.1 Photopatterned hydrogel without differential swelling*

Chapter 5 demonstrated the presence of reaction-induced differential swelling. It also presented a series of criteria that, if met, will yield high-fidelity structures without the enhanced crosslinking at the photopattern edge, induced by diffusion-limited reaction. The three identified criteria were as follows: (1) exposure times must be shorter than the propagation time to ensure features do not swell during photopatterning; and to eliminate the build-up of species at the photopattern edges (2) the total species conversion must be reduced or (3) diffusion rate and polymerization time must be significantly different. Developing a quantitative relationship between these criteria using a series of different photopatternable materials (*e.g.*, varied wt% hydrogels, varied molecular weight macromers, etc.) using SLA, is recommended. With a robust understanding of how reaction-induced differential swelling affects photopatterned hydrogels, a structure with fully defined mechanical and chemical properties can be fabricated.

### *7.2.2 3D hydrogel microfluidics*

As demonstrated in Chapter 6, encased 3D hydrogel channels are sensitive to the channel orientation, where channels with no outlet experience slower perfusion rates than those with outlets, and fluid flow, where the ceiling of encased channels is sensitive to perfusion. These properties can be harnessed to develop 3D microfluidic devices that are fabricated with 100% cytocompatible material. Devices with this control will enable body-on-a-chip applications where a drug and/or pathogen is perfused through the 3D cell-laden microfluidic device with precise control of the rate at which each cell type encounters the solution in question.[9]

### *7.2.3 Variable modulus 3D hydrogel*

Applying the techniques presented in Chapter 4 and 6 to fabricate a variable modulus 3D printed hydrogel is highly recommended due to the potential impact on the regenerative medicine community. Extending beyond the two-dimension photopatterns demonstrated in Chapter 4 to 3D will allow for user-defined mechanical properties within a cytocompatible structure. This capability is a gateway to fabricate diverse constructs for tissue engineering. With the incorporation of a biodegradable component into the printing precursor solution, constructs with defined 3D mechanical properties will enable studies in cellular response to 3D engineered extracellular matrices.

## 7.3 References


1. Park, J. H., Jang, J., Lee, J. S. & Cho, D. W. Three-Dimensional Printing of Tissue/Organ Analogues Containing Living Cells. *Ann. Biomed. Eng.* 1–15 (2016). doi:10.1007/s10439-016-1611-9
2. Jakab, K. *et al.* Tissue engineering by self-assembly and bio-printing of living cells. *Biofabrication* **2,** 22001 (2010).
3. Bajaj, P., Schweller, R. M., Khademhosseini, A., West, J. L. & Bashir, R. 3D Biofabrication Strategies for Tissue Engineering and Regenerative Medicine. *Annu. Rev. Biomed. Eng.* **16,** 247–76 (2014).
4. Fairbanks, B. D. *et al.* A versatile synthetic extracellular matrix mimic via thiol-norbornene photopolymerization. *Adv. Mater.* **21,** 5005–5010 (2009).
5. Chan, V., Zorlutuna, P., Jeong, J. H., Kong, H. & Bashir, R. Three-dimensional photopatterning of hydrogels using stereolithography for long-term cell encapsulation. *Lab Chip* **10,** 2062–2070 (2010).
6. Arcaute, K., Mann, B. & Wicker, R. Stereolithography of spatially controlled multi-material bioactive poly(ethylene glycol) scaffolds. *Acta Biomater.* **6,** 1047–1054 (2010).
7. Lin, H. *et al.* Application of visible light-based projection stereolithography for live cell-scaffold fabrication with designed architecture. *Biomaterials* **34,** 331–339 (2013).
8. Elomaa, L. *et al.* Three-dimensional fabrication of cell-laden biodegradable poly(ethylene glycol-co-depsipeptide) hydrogels by visible light stereolithography. *J. Mater. Chem. B* **3,** 8348–8358 (2015).
9. Jang, J., Yi, H.-G., Cho ACS Biomater Sci Eng, D.-W. & Cho, D.-W. 3D Printed Tissue Models: Present and Future. (2016). doi:10.1021/acsbiomaterials.6b00129

# Bibliography


1. Ahmed, S., Nakajima, T., Kurokawa, T., Anamul Haque, M. & Gong, J. P. Brittle–ductile transition of double network hydrogels: Mechanical balance of two networks as the key factor. *Polymer (Guildf).* **55,** 914–923 (2014).

2. Aisenbrey, E. A. & Bryant, S. J. Mechanical loading inhibits hypertrophy in chondrogenically differentiating hMSCs within a biomimetic hydrogel. *J. Mater. Chem. B* **4,** 3562–3574 (2016).

3. Akalp, U. *et al.* Determination of the Polymer-Solvent Interaction Parameter for PEG Hydrogels in Water: Application of a Self Learning Algorithm. *Polymer (Guildf).* **66,** 135–147 (2015).

4. Allan, K. S., Pilliar, R. M., Wang, J., Grynpas, M. D. & Kandel, R. A. Formation of biphasic constructs containing cartilage with a calcified zone interface. *Tissue Eng.* **13,** 167–77 (2007).

5. Amer, L. D. & Bryant, S. J. The In Vitro and In Vivo Response to MMP-Sensitive Poly(Ethylene Glycol) Hydrogels. *Ann. Biomed. Eng.* (2016). doi:10.1007/s10439-016-1608-4

6. Anseth, K. S. *et al.* Kinetic evidence of reaction diffusion during the polymerization of multi(meth)acrylate monomers. *Macromolecules* **27,** 650–655 (1994).

7. Arcaute, K., Mann, B. & Wicker, R. Stereolithography of spatially controlled multi-material bioactive poly(ethylene glycol) scaffolds. *Acta Biomater.* **6,** 1047–1054 (2010).

8. Ashley, J. F., Cramer, N. B., Davis, R. H. & Bowman, C. N. Soft-lithography fabrication of microfluidic features using thiol-ene formulations. *Lab Chip* **11,** 2772–2778 (2011).

9. Aziz, A. H. *et al.* Mechanical characterization of sequentially layered photo-clickable thiol-ene hydrogels. *J. Mech. Behav. Biomed. Mater.* **65,** 454–465 (2017).

10. Bajaj, P., Schweller, R. M., Khademhosseini, A., West, J. L. & Bashir, R. 3D Biofabrication Strategies for Tissue Engineering and Regenerative Medicine. *Annu. Rev. Biomed. Eng.* **16,** 247–76 (2014).

11. Balluffi, Robert, W., Samuel, M., Allen & Craig Carter, W. Solutions to the Diffusion Equation - Solutions to Fick ' s Laws. *Kinet. Mater.* 1–18 (2006).

12. Begley, M. R., Creton, C. & McMeeking, R. M. The elastostatic plane strain mode I crack tip stress and displacement fields in a generalized linear neo-Hookean elastomer. *J. Mech. Phys. Solids* **84,** 21–38 (2015).

13. Bergmann, G. *et al.* Hip contact forces and gait patterns from routine activities. *J. Biomech.* **34,** 859–871 (2001).

14. Bhatia, S., Chen, C., Liu, V. A. & Bhatia, S. N. Hybrid Bio/Arti®cial Microdevices: Three-Dimensional Photopatterning of Hydrogels Containing Living Cells. *Biomed. Microdevices* **4,** 257–266 (2002).

15. Billiet, T., Vandenhaute, M., Schelfhout, J., Van Vlierberghe, S. & Dubruel, P. A review of trends and limitations in hydrogel-rapid prototyping for tissue engineering. *Biomaterials* **33,** 6020–6041 (2012).

16. Binning, G., Gerber, CH., Stoll, E., T. R. A. C. F. Q. Atomic Resolution with Atomic Force Microscope. *Eur. Lett.* **12,** 1281–1286 (1987).

17. Binning, G., Rohrer, H., Gerber, C. & Weibel, E. Surface Studies by Scanning Tunneling Microscopy. *Treatises Mater. Sci. Technol. A. V. Granato* **49,** 505–33 (1958).

18. Bryant, S. J., Anseth, K. S., Lee, D. a. & Bader, D. L. Crosslinking density influences the morphology of chondrocytes photoencapsulated in PEG hydrogels during the application of compressive strain. *J. Orthop. Res.* **22,** 1143–1149 (2004).

19. Bryant, S. J., Nuttelman, C. R. & Anseth, K. S. Cytocompatibility of UV and visible light photoinitiating systems on cultured NIH/3T3 fibroblasts in vitro. *J. Biomater. Sci. Polym. Ed.* **11,** 439–457 (2000).

20. Bryant, S. J., Nuttelman, C. R. & Anseth, K. S. The effects of crosslinking density on cartilage formation in photocrosslinkable hydrogels. *Biomed. Sci. Instrum.* **35,** 309–14 (1999).

21. Burdick, J. A. & Anseth, K. S. Photoencapsulation of osteoblasts in injectable RGD-modified PEG hydrogels for bone tissue engineering. *Biomaterials* **23,** 4315–4323 (2002).

22. Butt, H.-J., Cappella, B. & Kappl, M. Force measurements with the atomic force microscope: Technique, interpretation and applications. *Surf. Sci. Rep.* **59,** 1–152 (2005).

23. Cha, C. *et al.* Structural Reinforcement of Cell-Laden Hydrogels with Microfabricated Three Dimensional Scaffolds. *Biomater. Sci.* **2,** 703–709 (2014).

24. Chan, V., Zorlutuna, P., Jeong, J. H., Kong, H. & Bashir, R. Three-dimensional photopatterning of hydrogels using stereolithography for long-term cell encapsulation. *Lab Chip* **10,** 2062–2070 (2010).

25. Chen, C. S., Mrksich, M., Huang, S., Whitesides, G. M. & Ingber, D. E. Geometric control of cell life and death. *Science* **276,** 1425–1428 (1997).

26. Chen, Q., Chen, H., Zhu, L. & Zheng, J. Fundamentals of double network hydrogels. *J. Mater. Chem. B* **3,** 3654–3676 (2015).

27. Chim, H. *et al.* A comparative analysis of scaffold material modifications for load-bearing applications in bone tissue engineering. *Int. J. Oral Maxillofac. Surg.* **35,** 928–934 (2006).

28. Cooke, M. N., Fisher, J. P., Dean, D., Rimnac, C. & Mikos, A. G. Use of stereolithography to manufacture critical-sized 3D biodegradable scaffolds for bone ingrowth. *J. Biomed. Mater. Res. B. Appl. Biomater.* **64,** 65–69 (2003).

29. Corbel, S., Dufaud, O. & Roques-Carmes, T. *Materials for stereolithography*. *Stereolithography* (2011).

30. Cramer, N. B., Davies, T., O'Brien, A. K. & Bowman, C. N. Mechanism and modeling of a thiol-ene photopolymerization. *Macromolecules* **36,** 4631–4636 (2003).

31. Cramer, N. B., Reddy, S. K., O'Brien, A. K. & Bowman, C. N. Thiol−Ene Photopolymerization Mechanism and Rate Limiting Step Changes for Various Vinyl Functional Group Chemistries. *Macromolecules* **36,** 7964–7969 (2003).

32. Creton, C. *et al.* Fracture and adhesion of soft materials: a review. *Reports Prog. Phys.* **79,** 46601 (2016).

33. Cui, H., Nowicki, M., Fisher, J. P. & Zhang, L. G. 3D Bioprinting for Organ Regeneration. *Adv. Healthc. Mater.* 1601118 (2016). doi:10.1002/adhm.201601118

34. D 'lima, D. D., Fregly, B. J., Patil, S., Steklov, N. & Colwell, C. W. Knee joint forces: prediction, measurement, and significance. *Spec. Issue Artic. Proc IMechE Part H J Eng. Med.* **226,** 95–102 (2012).

35. Decker, C. Kinetic Study and New Applications of UV Radiation Curing. *Macromol. Rapid Commun.* **23,** 1067–1093 (2002).

36. DeForest, C. A., Polizzotti, B. D. & Anseth, K. S. Sequential click reactions for synthesizing and patterning three-dimensional cell microenvironments. *Nat. Mater.* **8,** 659–664 (2009).

37. Dorvee, J. R., Boskey, A. L. & Estroff, L. A. Rediscovering Hydrogel-Based Double-Diffusion Systems for Studying Biomineralization. *CrystEngComm* **14,** 5681–5700 (2012).

38. Ducrot, E., Chen, Y., Bulters, M., Sijbesma, R. P. & Creton, C. Toughening elastomers with sacrificial bonds and watching them break. *Science* **344,** 186–9 (2014).

39. Elomaa, L. *et al.* Three-dimensional fabrication of cell-laden biodegradable poly(ethylene glycol-co-depsipeptide) hydrogels by visible light stereolithography. *J. Mater. Chem. B* **3,** 8348–8358 (2015).

40. Engler, A. J., Sen, S., Sweeney, H. L. & Discher, D. E. Matrix elasticity directs stem cell lineage specification. *Cell* **126,** 677–89 (2006).

41. Extracellular matrix scaffolds for cartilage and bone regeneration. *Trends in Biotechnology* (2013).

42. Fairbanks, B. D. *et al.* A versatile synthetic extracellular matrix mimic via thiol-norbornene photopolymerization. *Adv. Mater.* **21,** 5005–5010 (2009).

43. Farley, R., Halacheva, S., Bramhill, J. & Saunders, B. R. Using click chemsitry to dial up the modulus of doubly crosslinked microgels through mrecise control of microgel building block functionalisation. *Polym. Chem.* (2015). doi:10.1039/C4PY01753F

44. Fiedler, C. I. *et al.* Enhanced mechanical properties of photo-clickable thiol-ene PEG hydrogels through repeated photopolymerization of in-swollen macromer. *Soft Matter* **12,** (2016).

45. Flory, P. J. & Erman, B. Theory of elasticity of polymer networks. 3. *Macromolecules* **15,** 800–806 (1982).

46. Flory, P. J. *Principles of polymer chemistry.* (Cornell University Press, 1953).

47. Fung, Y. C. & Tong, P. *Classical and Computational Solid Mechanics*. **1,** (WORLD SCIENTIFIC, 2001).

48. Gandavarapu, N. R., Alge, D. L. & Anseth, K. S. Osteogenic differentiation of human mesenchymal stem cells on α5 integrin binding peptide hydrogels is dependent on substrate elasticity. *Biomater. Sci.* **2,** 352–361 (2014).

49. Gong, J. P. Why are double network hydrogels so tough? *Soft Matter* **6,** 2583 (2010).

50. Gong, J. P., Katsuyama, Y., Kurokawa, T. & Osada, Y. Double-Network Hydrogels with Extremely High Mechanical Strength. *Adv. Mater.* **15,** 1155–1158 (2003).

51. Gould, S. T., Darling, N. J. & Anseth, K. S. Small peptide functionalized thiol–ene hydrogels as culture substrates for understanding valvular interstitial cell activation and de novo tissue deposition. *Acta Biomater.* **8,** 3201–3209 (2012).

52. Guo, N. & Leu, M. C. Additive manufacturing: Technology, applications and research needs. *Front. Mech. Eng.* **8,** 215–243 (2013).

53. Guvendiren, M., Molde, J., Soares, R. M. D. & Kohn, J. Designing Biomaterials for 3D Printing. *ACS Biomater. Sci. Eng.* **2,** 1679–1693 (2016).

54. Hadjiev, N. A. & Amsden, B. G. An assessment of the ability of the obstruction-scaling model to estimate solute diffusion coefficients in hydrogels. *J. Control. Release* **199,** 10–16 (2015).

55. Holmes, M. H. & Mow, V. C. The nonlinear characteristics of soft gels and hydrated connective tissues in ultrafiltration. *J. Biomech.* **23,** 1145–1156 (1990).

56. Hospodiuk, M., Dey, M., Sosnoski, D. & Ozbolat, I. T. The bioink: A comprehensive review on bioprintable materials. *Biotechnol. Adv.* (2017).

57. Huh, D., Hamilton, G. a. & Ingber, D. E. From 3D cell culture to organs-on-chips. *Trends Cell Biol.* **21,** 745–754 (2011).

58. Jacobs, P. Stereolithography 1993 : Epoxy Resins , Improved Accuracy & Investment Casting. (1993).

59. Jakab, K. *et al.* Tissue engineering by self-assembly and bio-printing of living cells. *Biofabrication* **2,** 22001 (2010).

60. Jang, J., Yi, H.-G., Cho ACS Biomater Sci Eng, D.-W. & Cho, D.-W. 3D Printed Tissue Models: Present and Future. (2016). doi:10.1021/acsbiomaterials.6b00129

61. Jang, J., Yi, H.-G., Cho ACS Biomater Sci Eng, D.-W. & Cho, D.-W. 3D Printed Tissue Models: Present and Future. (2016). doi:10.1021/acsbiomaterials.6b00129

62. Janusziewicz, R., Tumbleston, J. R., Quintanilla, A. L., Mecham, S. J. & DeSimone, J. M. Layerless fabrication with continuous liquid interface production. *Proc. Natl. Acad. Sci. U. S. A.* 201605271 (2016).

63. Kang, W., Bi, B., Zhuo, R. & Jiang, X. Photocrosslinked methacrylated carboxymethyl chitin hydrogels with tunable degradation and mechanical behavior. *Carbohydr. Polym.* **160,** 18–25 (2017).

64. Kenning, N. S., Ficek, B. A., Hoppe, C. C. & Scranton, A. B. Spatial and temporal evolution of the photoinitiation rate for thick polymer systems illuminated by polychromatic light: selection of efficient photoinitiators for LED or mercury lamps. *Polym. Int.* **57,** 1134–1140 (2008).

65. Kerrigan, I. S. *et al.* Highlights, disparity, and perceived gloss with convex and concave surfaces. *J. Vis.* **13,** 9–9 (2013).

66. Kloxin, A. M., Kasko, A. M., Salinas, C. N. & Anseth, K. S. Photodegradable hydrogels for dynamic tuning of physical and chemical properties. *Science* **324,** 59–63 (2009).

67. Kolesky, D. B. *et al.* 3D Bioprinting of Vascularized, Heterogeneous Cell-Laden Tissue Constructs. *Adv. Mater.* **26,** 3124–3130 (2014).

68. Kreimer, G. & Melkonian, M. Reflection confocal laser scanning microscopy of eyespots in flagellated green algae. *Eur. J. Cell Biol.* **53,** 101–11 (1990).

69. Kwan, M. K., Lai, W. M. & Mow, V. C. A finite deformation theory for cartilage and other soft hydrated connective tissues—I. Equilibrium results. *J. Biomech.* **23,** 145–155 (1990).

70. Lambert, P. *et al.* Mask projection microsterolithography of novel biocompatible polymers. 2284 (2014).

71. Langer, R. & Vacanti, J. P. Tissue engineering. *Science* **260,** 920–6 (1993).

72. Le Grimellec, C. *et al.* Imaging of the Surface of Living Cells by Low-Force Contact-Mode Atomic Force Microscopy. *Biophys. J.* **75,** 695–703 (1998).

73. Li, X., Lian, Q., Li, D., Xin, H. & Jia, S. Development of a Robotic Arm Based Hydrogel Additive Manufacturing System for In-Situ Printing. *Appl. Sci.* **7,** 73 (2017).

74. Limem, S. & Calvert, P. Diffusion properties of inkjet printed ionic self-assembling polyelectrolyte hydrogels. *J. Mater. Chem. B* **3,** 4569–4576 (2015).

75. Lin, B. J. Where Is The Lost Resolution? in *SPIE 0633, Optical Microlithography V* (ed. Stover, H. L.) 44–50 (International Society for Optics and Photonics, 1986).

76. Lin, H. *et al.* Application of visible light-based projection stereolithography for live cell-scaffold fabrication with designed architecture. *Biomaterials* **34,** 331–339 (2013).

77. Linnenberger, A. *et al.* Three dimensional live cell lithography. *Optics express* **21,** 10269–77 (2013).

78. Linnenberger, A. Live cell lithography and non-invasive mapping of neural networks. (University of Colorado Boulder, 2014).

79. Liska, R. *et al.* Photopolymers for rapid prototyping. *J. Coatings Technol. Res.* **4,** 505–510 (2007).

80. Lowe, A. B. Thiol-ene 'click' reactions and recent applications in polymer and materials synthesis. *Polym. Chem.* **1,** 17–36 (2010).

81. Luo, Y. & Shoichet, M. S. A photolabile hydrogel for guided three-dimensional cell growth and migration. *Nat. Mater.* **3,** 249–53 (2004).

82. Malda, J. *et al.* 25th Anniversary Article: Engineering Hydrogels for Biofabrication. *Adv. Mater.* **25,** 5011–5028 (2013).

83. Mansour, J. M. *Biomechanics of Cartilage in: Kinesiol. Mech. pathomechanics Hum. Mov.* (Lippincott Williams & Wilkins, 2003).

84. Marklein, R. A. & Burdick, J. A. Spatially controlled hydrogel mechanics to modulate stem cell interactions. *Soft Matter* **6,** 136–143 (2010).

85. Max Born & Emil Wolf. *Principles of Optics*. (Cambridge University Press, 1999).

86. Melchels, F. P. W., Feijen, J. & Grijpma, D. W. A review on stereolithography and its applications in biomedical engineering. *Biomaterials* **31,** 6121–30 (2010).

87. Mezger, T. G. The rheology handbook : for users of rotational and oscillatory rheometers. (2006).

88. Mikos, A. G. *et al.* Engineering complex tissues. *Tissue Eng.* **12,** 3307–3339 (2006).

89. Murphy, S. V & Atala, A. 3D bioprinting of tissues and organs. *Nat. Biotechnol.* **32,** 773–785 (2014).

90. Nguyen, N.-T. & Wereley, S. T. *Fundamentals and Applications of Microfluidics Second Edition*. (Artech House, 2006).

91. Nikolenko, V., Peterka, D. S. & Yuste, R. A portable laser photostimulation and imaging microscope. *J. Neural Eng.* **7,** 45001 (2010).

92. Norotte, C., Marga, F. S., Niklason, L. E. & Forgacs, G. Scaffold-free vascular tissue engineering using bioprinting. *Biomaterials* **30,** 5910–5917 (2009).

93. Obataya, I., Nakamura, C., Han, S., Nakamura, N. & Miyake, J. Nanoscale Operation of a Living Cell Using an Atomic Force Microscope with a Nanoneedle.

94. Odian, G. *Principles of Polymerization*. ( John Wiley & Sons, Inc., 2004).

95. Oh, S. H., An, D. B., Kim, T. H. & Lee, J. H. Wide-range stiffness gradient PVA/HA hydrogel to investigate stem cell differentiation behavior. *Acta Biomater.* (2016).

96. Park, J. H., Jang, J., Lee, J. S. & Cho, D. W. Three-Dimensional Printing of Tissue/Organ Analogues Containing Living Cells. *Ann. Biomed. Eng.* 1–15 (2016). =

97. Park, J. Y., Gao, G., Jang, J. & Cho, D.-W. 3D Printed Structures for Delivery of Biomolecules and Cells: Tissue Repair and Regeneration. *J. Mater. Chem. B* (2016). doi:10.1039/C6TB01662F

98. Park, S.-H., Yang, D.-Y. & Lee, K.-S. Two-photon stereolithography for realizing ultraprecise three-dimensional nano/microdevices. *Laser Photonics Rev.* **3,** 1–11 (2009).

99. Pellegrino, J., Makila, T., Mcqueen, S. & Taylor, E. Measurement Science Roadmap for Polymer-Based Additive Manufacturing Measurement Science Roadmap for Polymer-Based Additive Manufacturing Measurement Science Roadmap for Polymer-Based Additive Manufacturing i. *NIST Adv. Manuf. Ser.* **100,** (2016).

100. Peppas, N. A. & Reinhart, C. T. Solute diffusion in swollen membranes. Part I. A new theory. *J. Memb. Sci.* **15,** 275–287 (1983).

101. Peppas, N. A. Hydrogels and drug delivery. *Curr. Opin. Colloid Interface Sci.* **2,** 531–537 (1997).

102. Polizzotti, B. D., Fairbanks, B. D. & Anseth, K. S. Three-Dimensional Biochemical Patterning of Click-Based Composite Hydrogels via Thiolene Photopolymerization. *Biomacromolecules* **9,** 1084–1087 (2008).

103. Reddy, S. K., Cramer, N. B. & Bowman, C. N. Thiol−Vinyl Mechanisms. 1. Termination and Propagation Kinetics in Thiol−Ene Photopolymerizations. *Macromolecules* **39,** 3673–3680 (2006).

104. Reinhart, C. T. & Peppas, N. A. Solute diffusion in swollen membranes. Part II. Influence of crosslinking on diffusive properties. *J. Memb. Sci.* **18,** 227–239 (1984).

105. Roberts, J. J. & Bryant, S. J. Comparison of photopolymerizable thiol-ene PEG and acrylate-based PEG hydrogels for cartilage development. *Biomaterials* **34,** 9969–9979 (2013).

106. Rubinstein, M. & Colby, R. H. *Polymer physics*. (Oxford University Press, 2003).

107. Savitzky, A. & Golay, M. J. E. Smoothing and Differentiation of Data by Simplified Least Squares Procedures. *Anal. Chem.* **36,** 1627–1639 (1964).

108. Serbin, J. *et al.* Femtosecond laser-induced two-photon polymerization of inorganic-organic hybrid materials for applications in photonics. *Opt. Lett.* **28,** 301–303 (2003).

109. Sirrine, J. M. *et al.* 3D-Printable Biodegradable Polyester Tissue Scaffolds for Cell Adhesion. *Aust. J. Chem.* **68,** 1409 (2015).

110. Skaalure, S. C. & Engineering, B. Tuning Hydrogel Degradation for Cartilage Tissue Engineering by. (2014).

111. Stampfl, J. *et al.* Photopolymers with tunable mechanical properties processed by laser-based high-resolution stereolithography. *J. Micromechanics Microengineering* **18,** 125014 (2008).

112. Steinmetz, N. J., Aisenbrey, E. A., Westbrook, K. K., Qi, H. J. & Bryant, S. J. Mechanical loading regulates human MSC differentiation in a multi-layer hydrogel for osteochondral tissue engineering. *Acta Biomater.* **21,** 142–153 (2015).

113. Su, T. *et al.* Strong Bioinspired Polymer Hydrogel with Tunable Stiffness and Toughness for Mimicking the Extracellular Matrix. *ACS Macro Lett.* 1217–1221 (2016).

114. Sun, A. X., Lin, H., Beck, A. M., Kilroy, E. J. & Tuan, R. S. Projection Stereolithographic Fabrication of Human Adipose Stem Cell-Incorporated Biodegradable Scaffolds for Cartilage Tissue Engineering. *Front. Bioeng. Biotechnol.* **3,** 115 (2015).

115. Suntornnond, R., An, J. & Chua, C. K. Roles of support materials in 3D bioprinting. *Int. J. Bioprinting* **3,** (2017).

116. Talib, M. Fabrication and characterisation of 3 dimensional scaffold for tissue engineering application via microstereolithography technique. (2012).

117. Tang, Y. Stereolithography cure process modeling. (2005).

118. Tang, Y. Stereolithography cure process modeling. (2005). at <http://smartech.gatech.edu/handle/1853/7235>

119. Taylor, P., Vernerey, F. J., Greenwald, E. C. & Bryant, S. J. Computer Methods in Biomechanics and Biomedical Engineering Triphasic mixture model of cell-mediated enzymatic degradation of hydrogels. 37–41

120. Tele Nko, C. & Seepersad, C. C. A Comparative Evaluation of Energy Consumption of Selective Laser Sintering and Injection Molding of Nylon Parts. at <https://sffsymposium.engr.utexas.edu/Manuscripts/2011/2011-04-Telenko.pdf>

121. Tinuvin ® CarboProtect ®. at <http://aerospace.basf.com/common/pdfs/BASF_Tinuvin_CarboProtect_DS_USL_sfs.pdf>

122. Tormen, M. *et al.* 3D patterning by means of nanoimprinting, X-ray and two-photon lithography. *Microelectron. Eng.* **73–74,** 535–541 (2004).

123. Tumbleston, J. R. *et al.* Continuous liquid interface production of 3D objects. *Science (80-. ).* **347,** (2015).

124. Tumbleston, J. R. *et al.* Continuous liquid interface production of 3D objects. *Science (80-. ).* **347,** (2015).

125. Ulrich, T. a., De Juan Pardo, E. M. & Kumar, S. The mechanical rigidity of the extracellular matrix regulates the structure, motility, and proliferation of glioma cells. *Cancer Res.* **69,** 4167–4174 (2009).

126. Urness, A. C., Moore, E. D., Kamysiak, K. K., Cole, M. C. & Mcleod, R. R. Liquid deposition photolithography for submicrometer resolution three-dimensional index structuring with large throughput. *Light Sci. Appl.* **212,** (2013).

127. Verma, A. & Rai, R. Energy Efficient Modeling and Optimization of Additive Manufacturing Processes. at <https://www.researchgate.net/profile/Anoop_Verma5/publication/251231305_Energ

y_Efficient_Modeling_and_Optimization_of_Additive_Manufacturing_Processes/links/02e7e51eeec020ef49000000.pdf>

128. Vernerey, F. J., Greenwald, E. C. & Bryant, S. J. Triphasic mixture model of cell-mediated enzymatic degradation of hydrogels. *Comput. Methods Biomech. Biomed. Engin.* **15,** 1197–1210 (2012).

129. Wade, R. J., Bassin, E. J., Gramlich, W. M. & Burdick, J. A. Nanofibrous Hydrogels with Spatially Patterned Biochemical Signals to Control Cell Behavior. *Adv. Mater.* **27,** 1356–1362 (2015).

130. Walters, B. D. & Stegemann, J. P. Strategies for directing the structure and function of three-dimensional collagen biomaterials across length scales. *Acta Biomater.* **10,** 1488–1501 (2014).

131. Wang, X., Jiang, M., Zhou, Z., Gou, J. & Hui, D. 3D printing of polymer matrix composites: A review and prospective. *Compos. Part B Eng.* (2016).

132. Wang, Z. *et al.* A simple and high-resolution stereolithography-based 3D bioprinting system using visible light crosslinkable bioinks. *Biofabrication* **7,** (2015).

133. Watkins, A. W. & Anseth, K. S. Investigation of molecular transport and distributions in poly(ethylene glycol) hydrogels with confocal laser scanning microscopy. *Macromolecules* **38,** 1326–1334 (2005).

134. Weber, L. M., Lopez, C. G. & Anseth, K. S. Effects of PEG hydrogel crosslinking density on protein diffusion and encapsulated islet survival and function. *J. Biomed. Mater. Res. Part A* **90A,** 720–729 (2009).

135. Wei Lv, H. *et al.* Biomaterial stiffness determines stem cell fate. *Life Sci.* (2017).

136. Weng, Z., Zhou, Y., Lin, W., Senthil, T. & Wu, L. Structure-Property Relationship of Nano Enhanced Stereolithography Resin for Desktop SLA 3D Printer. *Compos. Part A Appl. Sci. Manuf.* (2016). doi:10.1016/j.compositesa.2016.05.035

137. Wilemski, G. On the derivation of Smoluchowski equations with corrections in the classical theory of Brownian motion. *J. Stat. Phys.* **14,** 153–169 (1976).

138. Yu, C. *et al.* Oxygen reduction reaction induced pH-responsive chemo-mechanical hydrogel actuators. *Soft Matter* **11,** 7953–7959 (2015).

139. Zabti, M. M. Effects of Light Absorber on Micro Stereolithography Parts A Thesis Submitted to The University of Birmingham for the Degree of Doctor of Philosophy By Mohamed Mohamed Zabti. (2012).

140. Zhao, G. & Mouroulis, P. Diffusion Model of Hologram Formation in Dry Photopolymer Materials. *J. Mod. Opt.* **41,** 1929–1939 (1994).

141. Zhou, G. *et al.* Digital light procession three-dimensional printing acrylate/collagen composite airway stent for tracheomalacia. *J. Bioact. Compat. Polym.* 88391151668609 (2017). doi:10.1177/0883911516686090

142. Zhou, X. *et al.* 3D bioprinted graphene oxide-incorporated matrix for promoting chondrogenic differentiation of human bone marrow mesenchymal stem cells. *Carbon N. Y.* (2017). doi:10.1016/j.carbon.2017.02.049

143. Zhou, Y. *et al.* Establishment of a Physical Model for Solute Diffusion in Hydrogel: Understanding the Diffusion of Proteins in Poly (Sulfobetaine Methacrylate) Hydrogel. *J. Phys. Chem. B* acs.jpcb.6b10355 (2017). doi:10.1021/acs.jpcb.6b10355